nature electronics

Article

https://doi.org/10.1038/s41928-024-01271-4

A wearable echomyography system based on a single transducer

Received: 16 May 2023

Accepted: 27 September 2024

Published online: 31 October 2024

Check for updates

Xiaoxiang Gao[1,8], Xiangjun Chen[2,8], Muyang Lin[1,8], Wentong Yue[1,8], Hongjie Hu[1], Siyu Qin[3], Fangao Zhang[2], Zhiyuan Lou[1], Lu Yin[1], Hao Huang[1], Sai Zhou[2], Yizhou Bian[1], Xinyi Yang[2], Yangzhi Zhu[4], Jing Mu[2], Xinyu Wang[1], Geonho Park[1], Chengchangfeng Lu[3], Ruotao Wang[1], Ray S. Wu[1], Joseph Wang[1], Jinghong Li[5] & Sheng Xu[1,2,3,6,7] ✉

Wearable electromyography devices can detect muscular activity for health monitoring and body motion tracking, but this approach is limited by weak and stochastic signals with a low spatial resolution. Alternatively, echomyography can detect muscle movement using ultrasound waves, but typically relies on complex transducer arrays, which are bulky, have high power consumption and can limit user mobility. Here we report a fully integrated wearable echomyography system that consists of a customized single transducer, a wireless circuit for data processing and an on-board battery for power. The system can be attached to the skin and provides accurate long-term wireless monitoring of muscles. To illustrate its capabilities, we use this system to detect the activity of the diaphragm, which allows the recognition of different breathing modes. We also develop a deep learning algorithm to correlate the single-transducer radio-frequency data from forearm muscles with hand gestures to accurately and continuously track 13 hand joints with a mean error of only 7.9°.

Wearable electronics can capture different types of signals on the skin surface for health monitoring and human–machine interactions[1–6] (Supplementary Note 1). For example, electromyography (EMG) can measure local field potentials generated by motor units during muscle activity[5,7] (Supplementary Fig. 1). However, EMG signals have low stability[8,9], spatial resolution[10,11] and signal-to-noise ratio[12,13] (Supplementary Notes 2 and 3). The irregular magnitude and frequency of motor unit firing, stochastic number of fired motor units and low level of synchronization between different motor units can lead to inconsistent results between measurements. The reception of EMG signals from specific muscle fibres occurs randomly, making it impossible to infer the signal source based on the time of arrival. Additionally, EMG signals from multiple muscle fibres are mixed; therefore, it is difficult to isolate the contributions of a specific muscle fibre. Furthermore, EMG signals are intrinsically weak during normal muscle activity[13], which reduces the signal-to-noise ratio[14] and detection accuracy[12,13], requiring large electrodes to compensate[15]. However, large electrodes average the local field potential under their area, reducing the spatial resolution.

Echomyography (EcMG) uses ultrasound to sense the activity of musculoskeletal systems and is accessible, safe and versatile[16,17]. Conventional EcMG uses a rigid array of transducer elements for spatial beamforming to achieve B-mode imaging, but this requires complex wiring, bulky control systems and a large amount of power[18,19]. Subsequently, soft ultrasound patches with arrays of transducer elements for spatial beamforming have been developed for B-mode imaging[19] and elastography[20] for monitoring muscle activities. However, when

[1]Aiiso Yufeng Li Family Department of Chemical and Nano Engineering, University of California San Diego, La Jolla, CA, USA. [2]Materials Science and Engineering Program, University of California San Diego, La Jolla, CA, USA. [3]Department of Electrical and Computer Engineering, University of California San Diego, La Jolla, CA, USA. [4]Terasaki Institute for Biomedical Innovation, Los Angeles, CA, USA. [5]Department of Medicine, University of California San Diego, La Jolla, CA, USA. [6]Shu Chien-Gene Lay Department of Bioengineering, University of California San Diego, La Jolla, CA, USA. [7]Department of Radiology, School of Medicine, University of California San Diego, La Jolla, CA, USA. [8]These authors contributed equally: Xiaoxiang Gao, Xiangjun Chen, Muyang Lin, Wentong Yue. ✉e-mail: shengxu@ucsd.edu

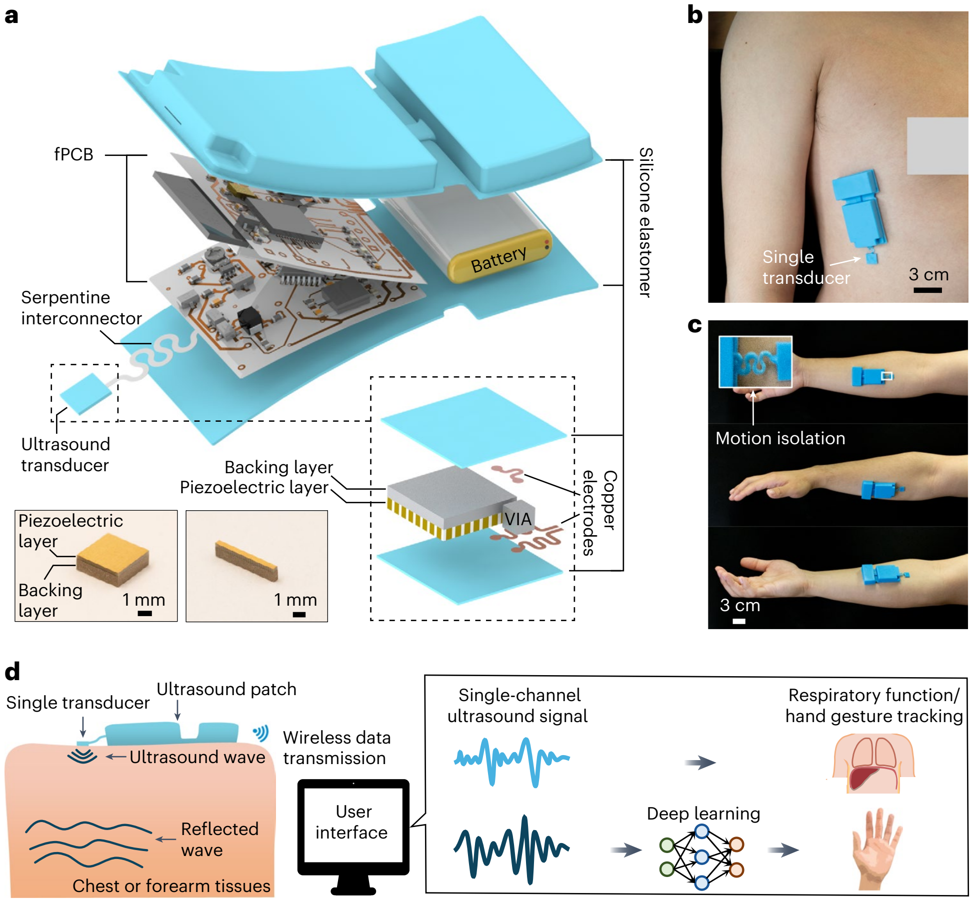

Fig. 1 | Overview of the fully integrated wearable single-transducer EcMG system. a, Schematic of the exploded view of the system. The top panel shows the whole device structure, including a compact single transducer, fPCB and battery, all encapsulated in a silicone elastomer. The bottom-left insets show the single transducers designed for different applications. The bottom-right inset shows the exploded view of the single transducer. **b**, Image of the system attached to the chest for diaphragm monitoring. **c**, Images of the system attached to the forearm for hand gesture tracking. The serpentine connector can isolate the motion between the single transducer and fPCB. **d**, Working principle of the system. The system has a soft interface with the skin. It can capture and precondition ultrasound waves reflected by deep muscles and wirelessly transmit the data to an external station for post-processing. The single-transducer RF signal is analysed to extract the respiration status directly or dynamic hand gesture through deep learning. VIA, vertical interconnect access.

integrated on a curved dynamic skin surface, a soft transducer array has uncertain morphologies and unknown locations and orientations of the transducer elements. This can cause inaccurate beamforming. In addition, the arrays still need tethering wires to the backend system for power and data transmission[18,19,21–23] (Supplementary Note 4), which can limit the participant's mobility.

EcMG can work with a single transducer. Single-transducer radio-frequency (RF) signals (that is, the waves reflected at tissue interfaces) cannot support spatial beamforming, but can reveal tissue thickness and activity[24]. Compared with EMG (where the electrodes passively collect signals), single-transducer EcMG actively transmits intensity-controlled ultrasound waves and collects RF signals that carry information from deep tissues, making them more stable[25]. Furthermore, the arrival time of RF signals is determined by the distance between the transducer and tissue interface. Therefore, RF signals are deterministic, based on the spatial distribution of tissues within the sonographic window[26], and can capture any change to that distribution. The actively transmitted intense ultrasound waves also have a high signal-to-noise ratio[27]. However, such devices are too large to be worn for continuous, long-term monitoring[28,29].

In this Article, we report a fully integrated wearable single-transducer EcMG system, consisting of a small single transducer, a wireless circuit and an on-board battery (Fig. 1a). The system can wirelessly and continuously monitor deep tissue activities with sub-millimetre spatial resolution and minimal constraints on the human body. We customize a wireless circuit on a flexible printed circuit board (fPCB) with low system complexity and power consumption to control the single transducer. We use the single-transducer EcMG system to monitor the diaphragm and recognize different breathing patterns. We also design a deep learning model to correlate the RF signals with specific forearm muscle distributions that correspond to complex hand gestures, allowing the development of a human–machine interface (Supplementary Note 5 and Supplementary Table 1).

Design of the single-transducer EcMG system

The single transducer contains a piezoelectric layer and a backing layer. The piezoelectric layer transmits and receives ultrasound waves, and features a 1–3 composite of lead zirconate titanate and epoxy with a high electromechanical coupling coefficient. The backing layer is bonded to one side of the piezoelectric layer to dampen excess vibration and expand the transducer bandwidth. We designed two single transducers with different geometries and therefore different sound fields to monitor the diaphragm and forearm muscles (Fig. 1a and Methods). The fPCB has two parts with a foldable connector: an analogue front end (AFE) to drive the transducer with a high-voltage pulse and to amplify the received RF signals, and a digital front end (DFE) to record data from the transducer and wirelessly transmit it to a computer (Supplementary Fig. 2 and Supplementary Note 6). The single transducer requires much less wireless bandwidth and power than a conventional transducer array. A lithium-polymer battery with a capacity of 400 mAh can power the entire system continuously for >3 h (Supplementary Fig. 3 and Supplementary Table 2). All components are encapsulated in an ~$4 \times 7 \times 1$ cm^3 silicone elastomer casing (Supplementary Fig. 4, Supplementary Note 7 and Supplementary Table 3).

Figure 1b shows the EcMG system attached to the chest for diaphragm monitoring. We applied a layer of adhesive silicone elastomer between the device and the skin to avoid the need for an ultrasound gel (Supplementary Fig. 5). Unlike conventional bulky ultrasound probes, the system does not need to be held in place manually during operation and thus does not constrain normal activities (Supplementary Fig. 6). Figure 1c shows the ultrasound system on the forearm at different wrist angles. The serpentine connector can decouple the single transducer from the motions of the fPCB and battery during activity, thereby ensuring measurement stability (Fig. 1c (inset) and Supplementary Fig. 7).

Figure 1d shows the system workflow. The fPCB activates the single transducer, which transmits an ultrasound pulse wave and then receives the echo from target tissues. The fPCB records the signal and wirelessly transmits the data to a backend system for processing. Because beamforming is not involved for the single-transducer RF signals, the system does not require any expensive professional image-processing stations as typically used with ultrasound transducer arrays. Only one ultrasound RF signal is acquired by the system per measurement. We can use the ultrasound RF signals directly to monitor the diaphragm thickness, or can develop a deep learning model that correlates the RF signals with complex muscle configurations representing different hand gestures.

Acousto-electric characterization

The AFE interfaces with the single transducer as the DFE samples the analogue signals and wirelessly transmits the data to a backend station for processing (Fig. 2a). The AFE performs sequence control, transducer activation and echo signal amplification (Supplementary Fig. 8). Delicate sequence control by a sequencer circuit is necessary for ultrasonic sensing, and can be divided into pulser charging and transmit/receive periods (Fig. 2b). During pulser charging, the boost converter amplifies the pulser voltage from 3.7 V to 120 V. During the subsequent transmit/receive period, the amplified high-voltage pulse activates the transducer. The transmit/receive switch relays the echo signals to the amplifier. Then, the output control sends the analogue signals to the DFE, where the analogue ultrasound signals are digitized by a built-in analogue-to-digital converter (ADC) in a microcontroller unit at a sampling rate of 12 MHz. A Wi-Fi module transmits the data to a backend station for further processing (Supplementary Fig. 9). The system acquires one RF signal trace every 20 ms (that is, at a frame rate of 50 Hz). This is sufficient to capture the detailed motions of the diaphragm and forearm muscles and maintain low power consumption.

The duration of the high-voltage pulse can be tuned from 100 ns to 500 ns, corresponding to excitation frequencies of 5 MHz to 1 MHz (Fig. 2c and Supplementary Fig. 10). The tunable pulse width is useful for driving transducers with different central frequencies at the maximum excitation efficiency. The amplitude of the driving pulse can vary over a wide range to emit ultrasound waves of different intensities (Fig. 2d). The amplifier can tune the signal amplitude to be recorded by the ADC. The gain should be maximized within the voltage range of the ADC (1.5 V in this study; Fig. 2e). The impulse response quantifies the central frequency, bandwidth and spatial resolution of an ultrasound system (Fig. 2f and Supplementary Figs. 11 and 12).

The sound field defines the detection region of the single transducer, which can be customized for specific applications. To accurately measure the diaphragm thickness, the transducer sound field should ideally be a narrow beam perpendicular to the top and bottom membranes of the diaphragm to avoid echoes from surrounding tissues. On the basis of simulations, the area of the single transducer should be 4×4 mm^2 (Supplementary Fig. 13). The scanned three-dimensional (3D) sound field of the single transducer confirmed the narrow beam (Fig. 2g (left), Supplementary Fig. 14 and Methods). We also designed a single transducer with an area of 0.5×4 mm^2, whose sound field is narrow in one plane and wide in the orthogonal plane, covering the cross section of the forearm (Fig. 2g, right).

Continuous diaphragm monitoring

The diaphragm is a large, dome-shaped muscle that separates the thoracic and abdominal cavities and is the main muscle responsible for respiration. It thickens as it contracts, which creates low pressure in the thoracic cavity and draws air into the lungs. Dysfunction may be caused by diaphragm paralysis, trauma and phrenic nervous diseases[30]. Ultrasonography is often used for point-of-care diaphragm monitoring.

We applied the ultrasound system in the intercostal view on the right side of the body, which accurately monitors the diaphragm thickness without beam tilting[31]. In this setup, the single transducer was attached in the zone of apposition, between the ninth and tenth ribs in the mid-axillary line[32] (Fig. 3a and Supplementary Fig. 15). We can identify three layers. A hypo-echogenic thick layer that is the diaphragm, surrounded by two hyper-echogenic layers representing the pleural and peritoneal membranes. The distance between these two hyper-echogenic layers is the diaphragm thickness, which is maximal and minimal at the end of inspiration and end of expiration, respectively. The diaphragm thickening fraction (DTF) is the difference in thickness between the end of inspiration and end of expiration divided by the thickness at the end of expiration[33]. This is widely used in the clinic to evaluate diaphragm dysfunction[34,35] and to predict the success of mechanical ventilation[32,36].

The continuous acquisition of such RF signals yields an M-mode image, which we simultaneously recorded during eupnea (normal breathing) using the single transducer and a commercial ultrasound linear array (Fig. 3b, Supplementary Fig. 16 and Methods). To verify the accuracy of the single transducer, we compared the diaphragm thicknesses measured by the two devices at end of inspiration and end of expiration during 100 breathing cycles (Fig. 3c). Linear regression revealed a high correlation coefficient. We calculated the DTF for 100 cycles followed by Bland–Altman analysis (Fig. 3d and Supplementary Note 8). We found that ~93% of the data were within the 95% confidence interval in a standard normal distribution, confirming that the single transducer is a good alternative to the commercial device (Supplementary Fig. 17). In addition, because of the stable attachment to the skin, daily activity and regular exercise do not introduce obvious artefacts (Supplementary Fig. 18).

The single transducer was also able to recognize different breathing modes. Abdominal respiration, also called diaphragmatic breathing, involves the use of abdominal muscles to contract the diaphragm, resulting in deeper breaths (Fig. 3e). Thoracic respiration (shallow breathing) mainly involves the movement of intercostal muscles to lift the ribs. Some pathological conditions, including hyperventilation, asthma, anxiety disorders, pneumonia and pulmonary oedema, often involve shallow respiration[37–39]. Shallow respiration may also result in stress, cognitive dysfunction or panic attacks[40,41]. However, most people with constant shallow thoracic breathing remain unaware of it. M-mode images of the diaphragm collected by the single transducer revealed the two different respiration modes (Fig. 3f and Supplementary Fig. 19). We tested the sensor's ability to distinguish between the two breathing modes in 13 healthy study participants (Supplementary Figs. 20–23). For each participant, we extracted the diaphragm thicknesses at the end of expiration and end of inspiration in five breathing cycles for each type of breathing mode and calculated the DTF for each breathing cycle (Fig. 3g). We performed a paired t-test[42]. The results indicated a statistical power of ~100% for detecting a difference of 0.367 in DTF, assuming a standard deviation of 0.194 and using a paired t-test with a two-sided significance level of 0.05. These

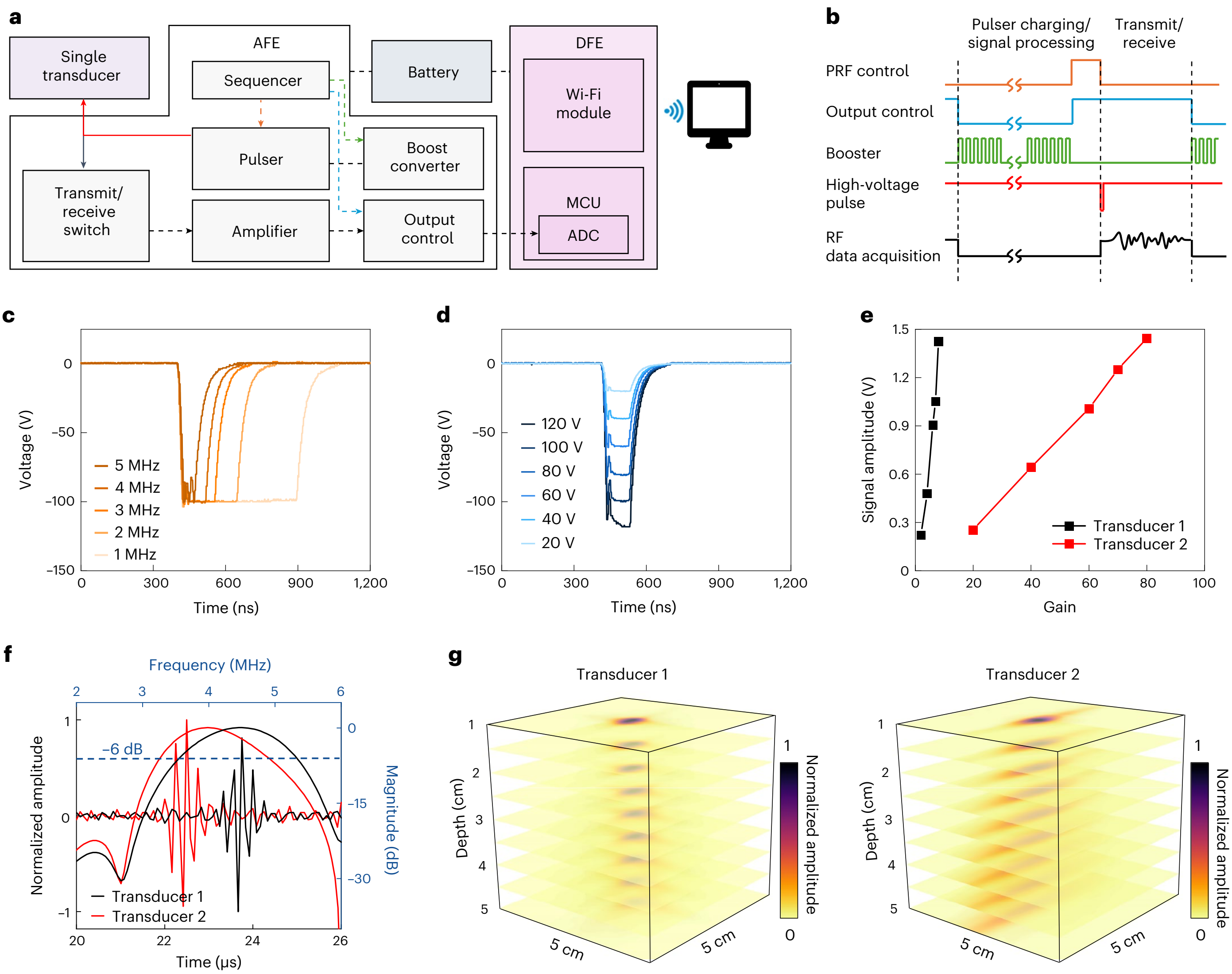

Fig. 2 | Acousto-electric characterization. a, Functional diagram of the system showing hardware blocks including a single transducer, a control circuit and a battery. The control circuit is composed of an AFE for transducer excitation and signal amplification and a DFE for data acquisition and wireless transmission. **b**, Timing sequence of the system. **c**, Duration of a high-voltage pulse is tunable to maximize the excitation efficiency of transducers with different central frequencies. **d**, Amplitude of a high-voltage pulse is tunable to excite transducers at different intensities. Here the pulses last 125 ns (corresponding to a central frequency of 4 MHz) with a maximum voltage of approximately −120 V. **e**, Amplification factor is tunable to fit the transducers with different sensitivities. Transducer 1 monitors the diaphragm and transducer 2 senses the forearm muscles. **f**, Pulse echo waves from a copper wire measured with different single transducers. After Fourier transformation, the frequency-domain curves of the signals show that the central frequencies are ~4 MHz, with a −6 dB bandwidth of ~1.6–1.8 MHz. **g**, Measured sound fields of single transducers for diaphragm monitoring (left) and hand gesture tracking (right). MCU, microcontroller unit. PRF, pulse repetition frequency.

findings validate that our sensor can effectively differentiate between the two breathing patterns.

Diaphragm monitoring of patients with COPD

We recruited three patients with chronic obstructive pulmonary disease (COPD), whose lung airways become inflamed and narrowed and tend to collapse at the expiratory phase (so-called airway obstruction). In such a case, the body forces air through the airways by coughing. Additionally, the expiratory phase of breathing is commonly prolonged[43,44]. In our test, patient 1 had relatively shallow respiration and frequent cough, which resulted in slight movement of the diaphragm in the M-mode image acquired by the single transducer (Fig. 4a). Because coughing was his major symptom, the M-mode image showed frequent fluctuations. Patient 2 had very typical symptoms of short inspiration and long expiration (Fig. 4b). Because patient 3 had mild COPD with minimal symptoms, the M-mode image showed regular periods of both inspiration and expiration with only occasional long expiration (Fig. 4c). In healthy participants, inspiration and expiration periods are relatively consistent (Fig. 4d). These results demonstrate that the single transducer could differentiate the breathing patterns of participants who were healthy and patients with chronic obstructive pulmonary disease, showing its clinical potential.

Dynamic hand gesture tracking

Different hand gestures correspond to a sophisticated but unique configuration of the forearm muscle groups[45] (Fig. 5a and Supplementary Fig. 24) and therefore a unique reflected RF signal. The single-transducer EcMG is much more sensitive than EMG and can therefore capture slight motions of the fingers and wrist (Supplementary Note 9, Supplementary Figs. 25 and 26 and Supplementary Video 1).

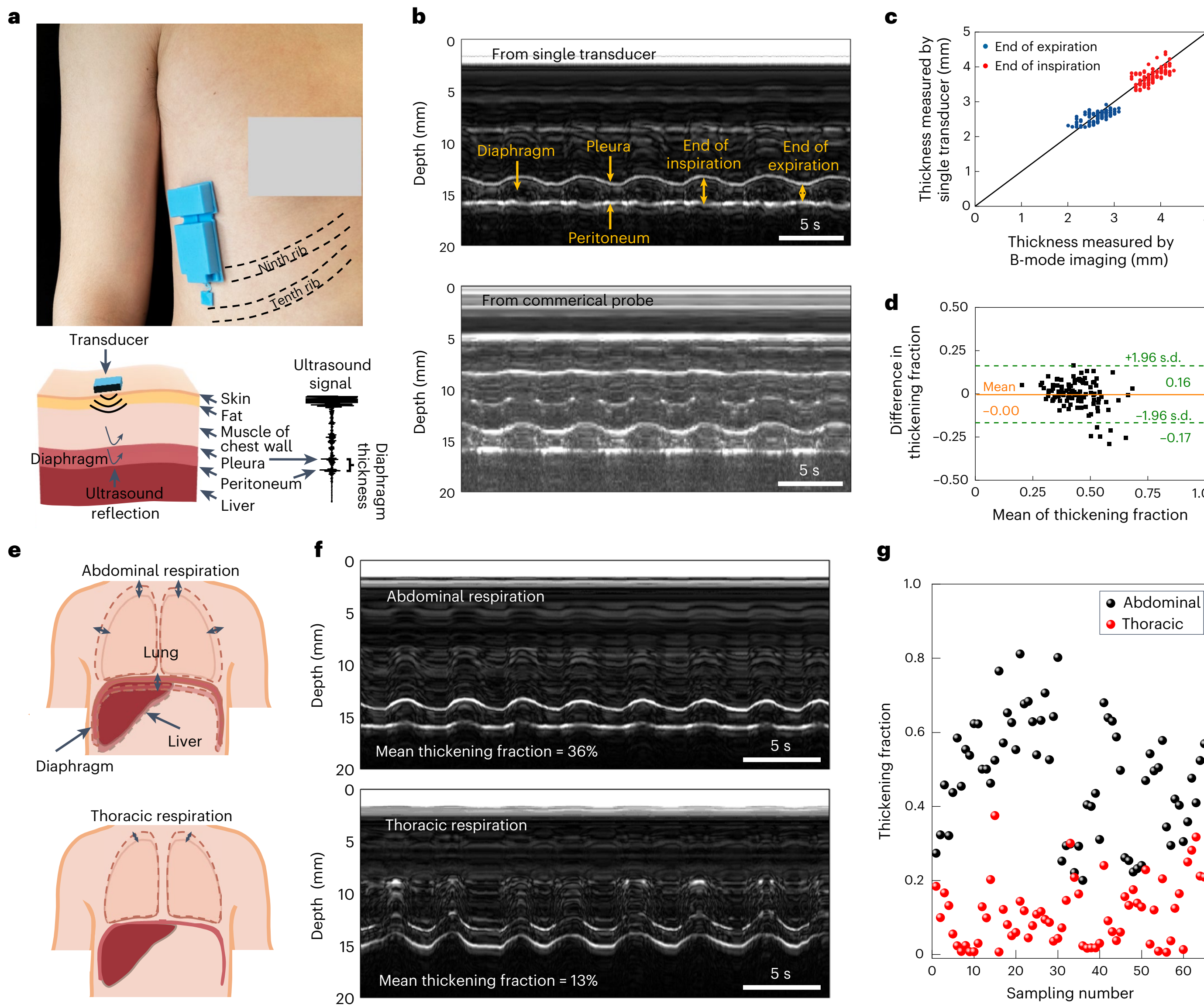

Fig. 3 | Continuous diaphragm monitoring using RF signals directly. **a**, Working setup and principle of diaphragm monitoring. The image shows the detection area of the system on the right side of the body (intercostal view, top). The schematic shows the tissue layers under the single transducer (bottom left). A typical ultrasound RF signal is highlighted to show the boundaries of the diaphragm (bottom right). **b**, M-mode images acquired simultaneously by the single transducer and a commercial probe for comparison. **c**, Quantitative comparison of the diaphragm thicknesses measured by the single transducer and commercial probe. **d**, Bland–Altman analysis of the DTF measured using the single transducer and commercial probe. The *x* axis is the mean DTF measured using the two devices and the *y* axis is the difference between them. **e**, Schematic showing the difference between the abdominal and thoracic respiration modes. **f**, Typical M-mode images corresponding to two different breathing modes. The diaphragm contributes to abdominal breathing but not to thoracic breathing. The diaphragm contracts during abdominal breathing, resulting in large DTFs. Although the diaphragm also moves during thoracic breathing, its thickness does not change substantially. **g**, DTFs measured for 13 healthy participants. Five abdominal and thoracic breathing cycles were measured for each participant.

It is challenging to establish a mathematical relationship between hand gestures and RF signals; therefore, we designed a deep neural network to correlate them. Using RF signals alone, the neural network was able to differentiate hand gestures with 13 degrees of freedom, including the bending angles of ten different finger joints and three rotation angles of the wrist (roll, pitch and yaw). Theoretically, the single transducer can continuously track hand gestures at a rate of several kilohertz. Given that the hand gestures change relatively slowly, we designed the system to accommodate a 50 Hz frame rate to reduce the power consumption (Supplementary Note 10).

The single transducer can capture the motion of muscles at an equivalent depth of ~6.6 cm (Supplementary Note 11). We collected a training dataset of paired RF signals and hand gestures. The ground-truth hand gesture was acquired by a commercial development kit including ten strain sensors and a six-axis inertial measurement unit sensor. The ten strain sensors measured the angles of ten different finger joints (Fig. 5a and Supplementary Fig. 27), whereas the inertial measurement unit sensor recorded the roll, pitch and yaw of the wrist (Supplementary Fig. 28 and Supplementary Note 12). New RF signals were then fed into the trained neural network to track the dynamic hand gestures (Supplementary Fig. 29 and Supplementary Table 4).

Figure 5b shows the RF signals for the relaxed state, followed by bending the middle finger and rotating the wrist (Supplementary Fig. 30 shows data for the other fingers and wrist motions). Each panel contains 20 RF signals, with each RF signal containing 1,024 data points. The initial reflection peaks correspond to shallow muscles, whereas

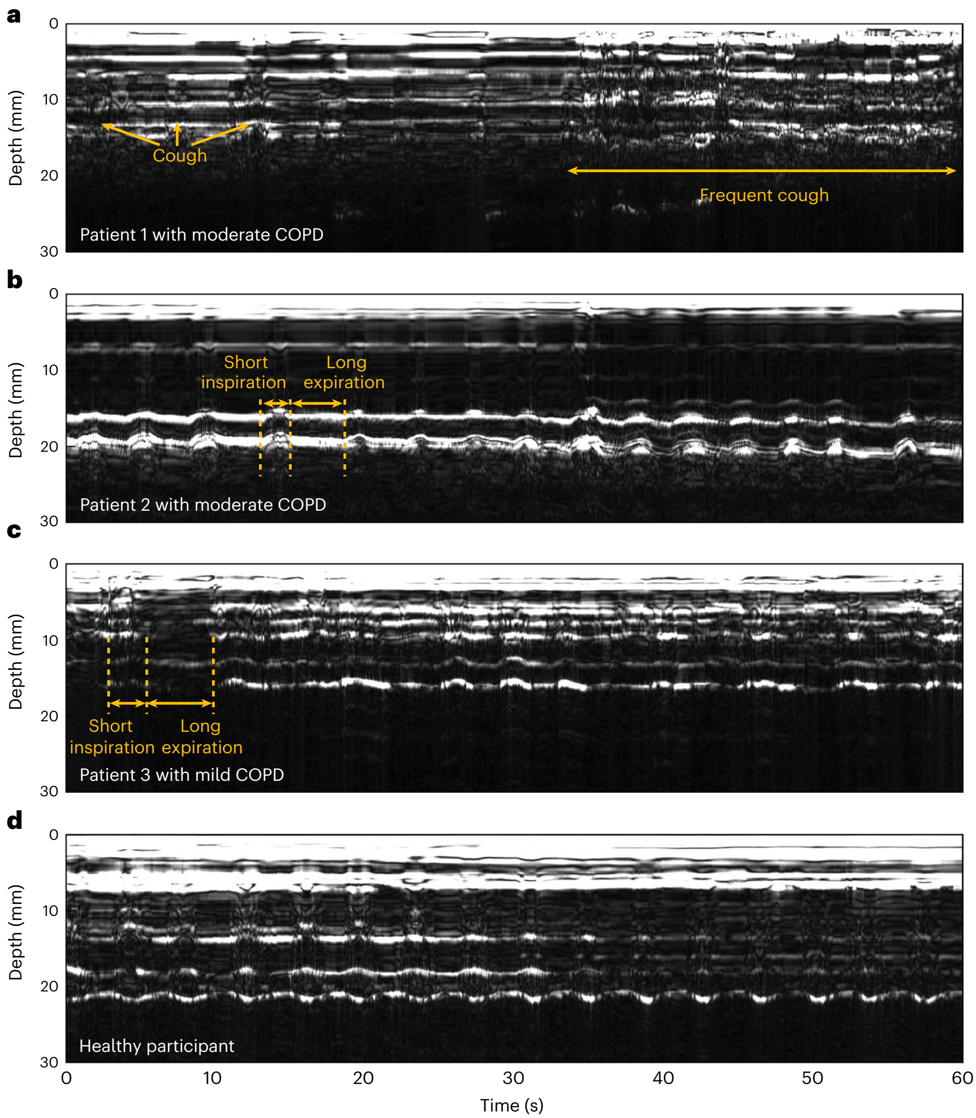

Fig. 4 | Diaphragm monitoring of patients with COPD and healthy participant. **a**, Patient 1 was diagnosed as having moderate COPD whose main symptom was coughing. The diaphragm showed slight movements because the patient exhibited weak respiration most of the time. The diaphragm membranes experienced obvious vibrations when the patient coughed frequently. **b**, Patient 2 had the typical symptom of a short inhaling period and a long exhaling period, which were consistent with ultrasound measurements. **c**, Patient 3 had mild COPD with minimal symptoms. Therefore, patient 3 could perform regular breathing most of the time, that is, with similar inspiration and expiration durations, and rarely having difficult exhaling. **d**, Healthy participant always exhibited regular respiration.

subsequent peaks belong to deep muscles. The shifts in those peaks qualitatively reveal muscle motions. We collected ~30,000 paired RF signals and hand gestures, ~70% of which were used for training and ~30% for validation. The neural network included eight layers of one-dimensional convolution at the front, with a rectified-linear-unit activation layer after each convolution layer (Supplementary Fig. 31). The data then proceeded through a flatten layer, a dropout layer (dropout rate, 0.2) and two fully connected layers. An activation function based on a rectified linear unit was integrated after each fully connected layer. The final layer yielded 13 different degrees of freedom as outputs. The performance of the trained neural network was tested on 1,000 frames of ultrasound signals representing 20 s of continuous hand motions (Fig. 5c); the dynamic hand motions predicted by the neural network (red curves) were superimposed on the ground truth (black curves) for comparison. We computed the prediction discrepancies of all the 13 degrees of freedom (Fig. 5d), with a mean value of only ~7.9° (Supplementary Table 5). These results confirmed that the single transducer can accurately track dynamic hand gestures.

Use cases as human–machine interfaces

To demonstrate the fast response and dynamic tracking of hand gestures, we applied the single transducer as a human–machine interface to control a virtual object and a robotic arm. The height of a virtual flying bird was controlled by the wrist pitch angle (Fig. 6a). We were able to continuously control the bird's trajectory through a cascade of barriers (Fig. 6b and Supplementary Video 2). We also used the single transducer as an interface between a hand gesture and robotic arm (Fig. 6c). We correlated the wrist pitch angle and the index finger metacarpophalangeal joint angle to the robotic arm's rotation angle and clamping distance, respectively. To achieve a designed motion trajectory (Fig. 6d), the single transducer must continuously track the angles of wrist pitching (Fig. 6e, blue curve) and index finger bending (Fig. 6e, orange curve). With these operations, the robotic arm could drop controlled amounts of water into two graduated cylinders (Supplementary Video 3). Five typical hand gestures and the corresponding robotic arm statuses are shown in Fig. 6e (insets). All these sophisticated gestures were captured to control the robotic arm by the fully integrated single-transducer EcMG system.

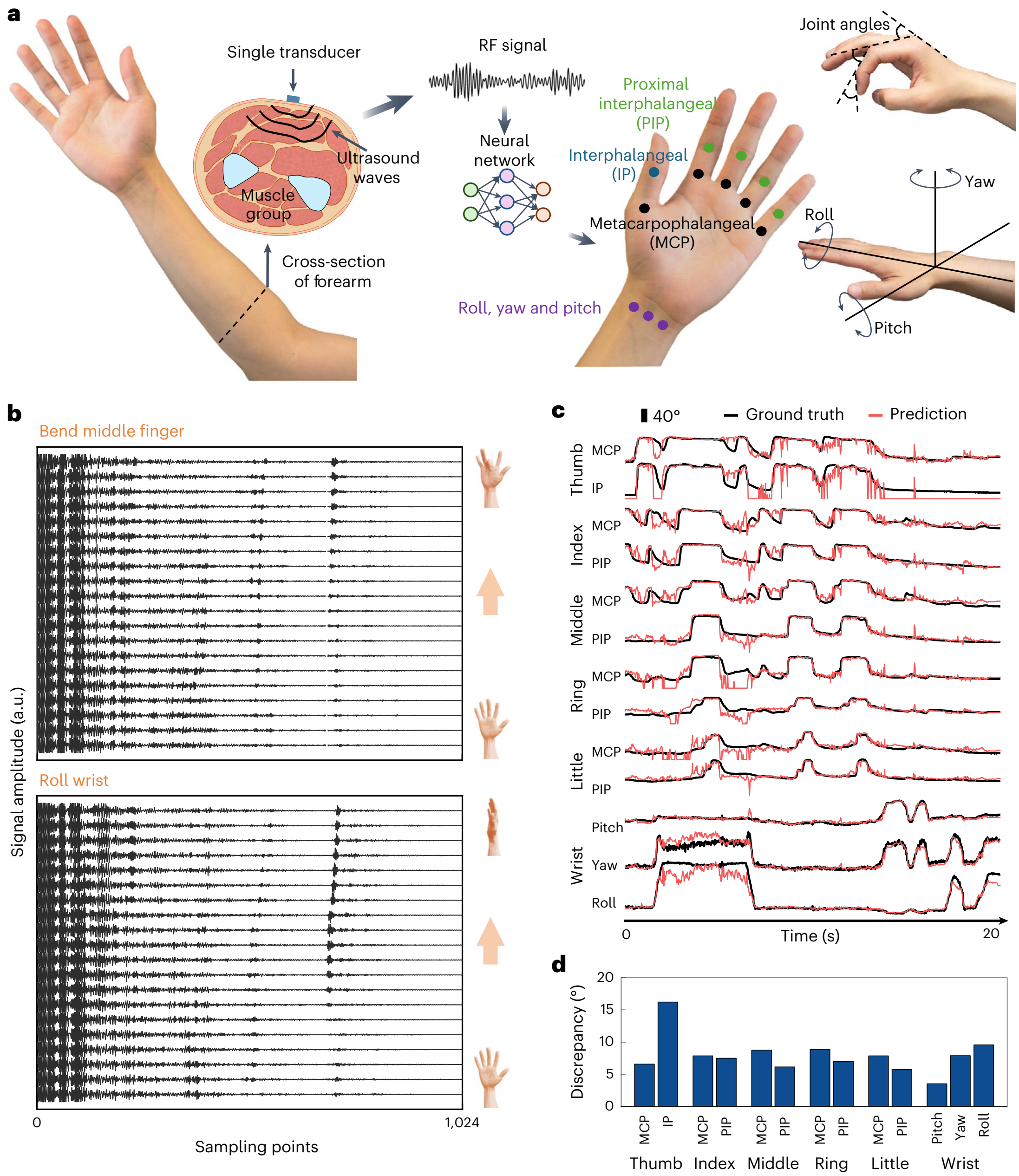

Fig. 5 | Dynamic hand gesture tracking using deep learning. a, Schematic of the working principle and flow chart of hand gesture tracking. Ultrasound pulse echo waves measured by a single transducer, corresponding to muscle distribution in the forearm, are fed to a deep neural network to infer 13 degrees of freedom of the hand gesture. Ten of them correspond to joint bending angles and three are the rotation angles of the wrist. **b**, Dynamic ultrasound echo waves as the finger bends and wrist rotates. Each panel shows 20 RF signals as the participant performs the corresponding motions continuously. The echo peaks shift back and forth because the corresponding tissue interfaces move towards and away from the skin surface. **c**, Continuous tracking of dynamic hand gestures predicted by analysing single-transducer RF signals using a deep neural network. The prediction agrees well with the ground truth collected using a commercial development kit. **d**, Discrepancies between the neural network prediction and ground truth of the 13 degrees of freedom.

Conclusions

We have reported a compact EcMG system that integrates a single transducer, an electrical circuit and a battery, and is encapsulated within a soft silicone elastomer. The device can be attached to the skin without any tethering wires and used for monitoring deep muscular dynamics. We illustrate this by using the EcMG system to sense the diaphragm and forearm muscles to detect breathing and hand gesture patterns, respectively. Compared with EMG, which measures the force generated by muscles, EcMG directly measures the status of muscle distribution (Supplementary Fig. 32). Inertial measurement unit sensors can also track the hand gesture with tens of sensors, but the wearable EcMG system has a smaller form factor and simpler wiring. We only demonstrated dynamic hand gesture tracking in healthy participants, but the wearable EcMG system is potentially suitable for amputees, for whom inertial measurement unit sensors and conventional strain sensor control mechanisms typically struggle to track[46]. The EcMG system can collect RF signals from the residual limb, where muscular motions resemble those in healthy limbs for the control of specific hand gestures[47,48].

The EcMG system can potentially benefit clinical research in two aspects. First, it provides a method for continuously monitoring patients with respiratory diseases[49,50]. The most important aspect of respiratory disease management is to prevent exacerbation, which

 https://doi.org/10.1038/s41928-024-01271-4

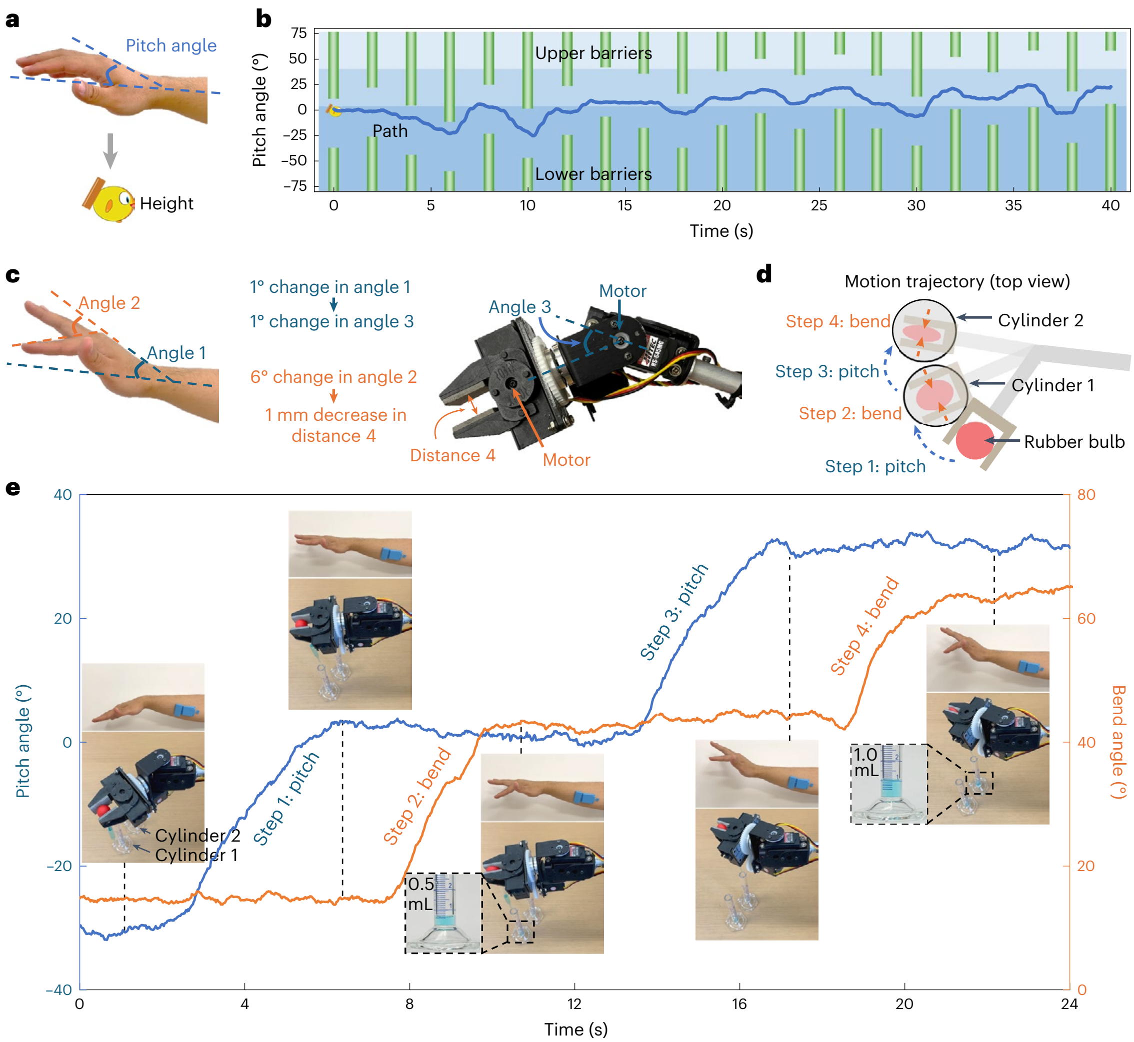

Fig. 6 | Human–machine interface using the wearable EcMG system. a, Pitch angle of the wrist controlling the height of a virtual bird. The height is calculated by multiplying the pitch angle by a scale factor. **b**, Virtual bird, controlled by the wrist, can successfully navigate through an irregular path between barriers. **c**, Control mechanism of the robotic arm to finish pipetting. The pitch angle of the wrist controls the rotation of the robotic arm, and the metacarpophalangeal joint of the index finger controls the clamp contraction. **d**, Designed motion trajectory of the robotic arm. **e**, Continuous tracking of the angles of the wrist and finger during motion. The insets show images of the hand gesture and robotic arm at five typical moments.

can accelerate the decline of lung function and increase mortality[51]. The EcMG system could potentially predict exacerbation and guide personalized preventive treatment by detecting early physiological changes and providing real-time data to healthcare providers or patients. Second, the system can potentially help clinicians find the best timing for initializing and extubating mechanical ventilations. Most pulmonary diseases, particularly bacterial and viral pneumonia, may progress to respiratory failure. Many of these patients need mechanical ventilation support. However, either premature or prolonged mechanical ventilation can cause harm to the patients, such as airway trauma, deconditioning and profound muscle weakness[52,53]. The EcMG system allows for continuous monitoring, potentially enabling doctors to determine the best timing for extubating patients with greater precision and thus better patient experience and treatment outcomes[32,54,55].

Future work on the EcMG technology could address the following issues. First, the analysis of the changes in diaphragm thickness was done manually, which is time-consuming, prone to operational errors and unsuitable for long-term monitoring. Image segmentation methods could be developed to track M-mode images, allowing the diaphragm thickness and relevant parameters to be calculated autonomously. Second, the number of degrees of freedom was limited by the number of strain and inertial measurement unit sensors in the commercial development kit used to acquire the ground truth. Adding more sensors would improve the accuracy of hand gesture tracking even further. Third, after training, the application of the EcMG system to new people and new forearm positions for hand gesture recognition is challenging[7,56]. Potential solutions include developing adaptive learning algorithms[7] and adopting transfer learning to reduce the retraining load[57] (Supplementary Note 13). Fourth, we used a transducer central frequency of 4 MHz, which is limited by the sampling rate of the microcontroller unit (12 MHz). High-rate ADC chips would increase the sampling rate to several tens of megahertz and thus improve the accuracy of monitoring muscle activities. Fifth, the current system integrates many commercial off-the-shelf chips, which account for the device size. Replacing these with application-specific integrated circuit chips could further reduce the form factor and power consumption. Finally, for hand gesture tracking, the current system must be connected to a computer to access the neural network. Machine learning algorithms could instead be run on a chip within the fully integrated wearable system (that is, edge computing) to eliminate the need for a bulky backend system.

https://doi.org/10.1038/s41928-024-01271-4

Methods

Fabrication of wearable single transducers

We used 1–3 lead zirconate titanate 5A composites (Del Piezo) as the piezoelectric material (thickness, ~0.35 mm). We chose E-Solder 3022 silver epoxy composite (EIS) to fabricate the backing layer, which was made by mixing silver epoxy and hardener at a weight ratio of 100:8 before transfering to a mould (thickness, 0.65 mm) for curing at 80 °C for 2 h. The piezoelectric material and backing layer were then bonded with the same silver epoxy composite. We diced the bonded material into small single transducers ($4 \times 4 \times 1\ mm^3$ for diaphragm sensing and $4 \times 0.5 \times 1\ mm^3$ for forearm muscle sensing).

Copper foils (thickness, 20 µm) were used to fabricate serpentine electrodes connecting the transducer to the fPCB. To ensure effective bonding to the silicone elastomer, a polyimide film (PI2545 precursor, HD MicroSystems) was spin coated onto the copper foil at a speed of 4,000 r.p.m. for 60 s. The polyimide layer was cured by soft baking at 100 °C for 5 min and hard baking at 300 °C for 1 h in a nitrogen atmosphere. We used ultraviolet light to activate the polyimide for 3 min and then laminated the copper foil/polyimide on polydimethylsiloxane (SYLGARD 184)-coated glass. Serpentine electrodes were fabricated by laser ablation (LaserMarks) at a wavelength of 1,059–1,065 nm, power of 0.228 mJ and speed of 300 mm s^{-1}. The patterned electrodes were transfer-printed onto glass coated with the silicone elastomer Ecoflex 00-30 (Smooth-On) using water-soluble tape (3M) after 3 min of ultraviolet light activation. The electrodes and Ecoflex-coated glass were then placed in an oven for 10 min at 80 °C to strengthen the bonding. The water-soluble tape was washed away.

The top and bottom electrodes were fabricated in the same way, and were bonded to the top and bottom surfaces of the single transducer with silver epoxy. A silver epoxy vertical interconnect access ($1 \times 1 \times 1\ mm^3$) was used to guide the top and bottom electrodes to the same plane. Finally, all the components were encapsulated in Ecoflex 00-30.

Key components of the integrated circuit

The circuit was fabricated on a four-layered fPCB (PCBWay). Four layers of copper electrodes (each 12 µm thick) were insulated by polyimide layers (each 25 µm thick) between every two copper layers and were covered with two polyimide layers (each 12.5 µm thick) on the top and bottom surfaces. ATmega328P and PIC32 microcontrollers (Microchip Technology) were used for sequence control and sampling, respectively. Operational amplifiers ADA4895 and ADA4897 (Analog Devices) were used for echo signal amplification. An ESP32 Wi-Fi chip (Espressif Systems) was used for wireless communication. A $3.7 \times 1.75 \times 0.82\ cm^3$ lithium-polymer battery (LIPO 801735) was used as the power source. The maximum booster output voltage was limited to 120 V by a Zener diode. The circuit board and battery were encapsulated in Ecoflex 00-30. The device was finally attached to the skin with a layer of Silbione A-4717 adhesive silicone (Factor II).

Characterization of impulse response and sound field

We measured the pulse echo signals of one copper wire (diameter, ~160 µm) at a distance of 1.5 cm from the wearable ultrasound system (Supplementary Fig. 11). The reflected signal was the temporal impulse response. The spectra in the frequency domain were used to extract the bandwidth. The sound fields of the single transducers, decided by their geometrical shapes and frequencies, were measured in a water tank using an HNP-0400 hydrophone (ONDA). An automatic AIMS III scanning system (ONDA) moved the hydrophone in 3D space to map the ultrasound intensity point by point (Supplementary Fig. 14). The peak-to-peak values of the signals measured by the hydrophone were calculated and normalized to reveal the 3D sound fields.

Simulation of sound field

To determine the optimal transducer size, we used the open-source MATLAB toolbox Field II (ref. 58) to study the sound field of a single transducer. The sound speed, medium density and transducer frequency were set as 1,540 m s^{-1}, 1,000 kg m^{-3} and 4 MHz, respectively. For diaphragm monitoring, the transducer shape was set as a square. We simulated the sound fields of transducers with four different widths: 0.5 mm, 2 mm, 4 mm and 6 mm (Supplementary Fig. 13). Because the typical depth range of the diaphragm is 1–4 cm for people with a body mass index of <35 (ref. 59), the sound field in this range should be as narrow and uniform as possible. For small transducers (0.5 and 2 mm in width), the sound beam has a width of >1 cm at a depth of 4 cm. For the large transducer (6 mm in width), it has a long near-field (>2 cm) where its sound intensity fluctuates along its depth, which can cause measurement inaccuracy. For the medium transducer (4 mm in width), the sound beam has uniform width and signal amplitude at a depth of 1–4 cm. We, therefore, chose the 4-mm single transducer for diaphragm monitoring. We used a similar strategy to choose the size of the single transducer for forearm monitoring.

Diaphragm monitoring with wearable and commercial probes

The poor acoustic window of the spleen makes it difficult to acquire a clear image of the diaphragm from the left side of the body[31]. Therefore, the right hemidiaphragm is typically used for ultrasonic diaphragm monitoring. We first used a commercial Vantage 256 ultrasound imaging system (Verasonics) to find the position of the diaphragm by acquiring B-mode images between the ninth and tenth ribs on the right side of the body. The diaphragm is parallel to the skin surface in the B-mode image. After locating the diaphragm in the image, we labelled the position above the diaphragm on the skin, where the single transducer should be placed. The ultrasound patch was then attached to the skin, ensuring the single transducer was in the correct place. The wearable ultrasound system could, thus, record stable RF signals with clearly reflected peaks from the pleura and peritoneum.

Simultaneously, we held the L11-5v commercial probe (Verasonics) and pressed it gently on top of the wearable single transducer. Thus, the single transducer and the commercial probe could simultaneously detect the same position to validate the accuracy of the wearable single transducer. Because the single transducer affected the ultrasound-wave transmission of the commercial probe, the B-mode image of the commercial probe immediately below the single transducer was darker than the other regions (Supplementary Fig. 16). In the image, we selected an A line that was a small lateral distance away from the single transducer for comparison (Supplementary Fig. 16). The participant was sitting on a chair to make sure the commercial probe stably recorded the B-mode images of the diaphragm. We simultaneously recorded data from the single transducer and commercial probe for 15 min as the participant breathed normally. All human tests described here were approved by the University of California San Diego Institutional Review Board (approval no. 804227).

Dataset acquisition representing different breathing modes

The participant was instructed to practice abdominal respiration for 30 min and thoracic respiration for 30 min. Because the frame rate of the ultrasound system is 50 Hz, each dataset comprising 300 frames of RF signals forms an M-mode image covering 6 s. Similarly, 50 frames, 100 frames, 150 frames, 200 frames and 250 frames last 1 s, 2 s, 3 s, 4 s and 5 s, respectively. We randomly extracted 140 M-mode images representing each breathing mode and performed *t*-distributed stochastic neighbour embedding analysis for comparison.

Dataset acquisition and deep neural network training for hand gesture tracking

Although we can track 13 angles, including ten finger joint angles and three wrist rotation angles, bending one joint or one finger inevitably involves the movement of the other joints or fingers. Therefore, Fig. 5b and Supplementary Fig. 30 only show eight, rather than 13, typical motions.

We developed a deep neural network to infer hand gestures from RF signals. Training was necessary for the neural network to learn the relationship between the ultrasound signal and hand gesture. The sampling rate of the ultrasound system was 12 MHz, and the data of each RF signal contained 1,024 sampling points, which meant the system could detect all muscles within a region at an equivalent depth of $1{,}024 \times 1.54\ \mathrm{mm\ \mu s^{-1}}/(12\ \mathrm{MHz} \times 2) \approx 6.6\ \mathrm{cm}$.

We used a Flexpoint glove development kit to collect the ground truth of different hand gestures. The glove kit contained ten strain sensors, which could be placed on ten joints to measure the bending angles, and a six-axis inertial measurement unit sensor, which was fixed on the back of the hand to measure the palm angles based on roll, pitch and yaw. We calibrated the electrical outputs of the strain sensors at several bending angles by applying curve fitting (Supplementary Fig. 27). The six-axis inertial measurement unit sensor (KMX62) included a three-axis accelerometer and a three-axis magnetometer. The influence of the ambient magnetic field was eliminated by calibration (Supplementary Fig. 28). During training dataset acquisition, the participant continuously bent their fingers and rotated their wrist and maintained the same forearm position, because the ultrasound signal also depends on the forearm posture. Maintaining the forearm position during the collection of training and testing datasets ensured that the hand gesture was the only variable that changed the ultrasound signal. A glove data recording session was triggered when one ultrasound RF signal was received by the single transducer. The time delay between signal reception and glove kit data reading was <1 ms, within which the hand gesture changed by only a negligible degree. Therefore, the ultrasound signal and glove kit data were considered to have one-to-one correspondence for neural network training.

The ultrasound signal and hand gesture data were normalized to ranges of −1 to 1 and 0 to 1, respectively, before they were fed into the neural network (Supplementary Fig. 31). All the first eight layers were bilayers of a one-dimensional convolution layer followed by a rectified-linear-unit activation layer. A flatten layer was then used to transform the data into one column. A dropout layer with a drop rate of 0.2 was added to prevent overfitting. The data then passed through two fully connected layers, each with a rectified-linear-unit activation function, and finally fed to an output layer. The network could output 13 values, corresponding to 13 degrees of freedom of the hand gesture. These numbers were scaled by normalization factors used during preprocessing. We used the mean squared error as the loss function and the Adam optimizer in the training procedure.

System setup for human–machine interfaces

When controlling the virtual object or robotic arm, the wearable EcMG system recorded RF data and wirelessly transmitted it to a computer for further processing. The neural network on the computer (equipped with an NVIDIA 2080 Ti graphics card) predicted the hand gesture based on the RF data and used the predicted results to control the virtual object or robotic arm. To control the virtual object, the pitch angle was transformed into height by using a scale factor in Unity software (Unity 2022). The robotic arm had two motors, one controlling rotation and the other controlling clamp contraction. The robotic arm rotated by the same angle as the wrist. The robotic arm clamp contracted 1 mm when the index finger metacarpophalangeal joint bent 6°, considering both the size of the dropper rubber bulb and the accuracy of joint angle bending. We placed two graduated cylinders on the table below the robotic arm, which could hold the rubber bulb of a dropper and rotate horizontally (Fig. 6d). First, we rotated the wrist to move the robotic arm and the dropper above cylinder 1. Second, we bent the metacarpophalangeal joint to contract the clamp and dispense 0.5 ml water into cylinder 1. Third, we rotated the wrist by another angle to move the robotic arm and the dropper above cylinder 2. Finally, we bent the metacarpophalangeal joint again to dispense 1.0 ml water into cylinder 2. To control the virtual object and robotic arm in real time, a moving averaging method with a sliding window of 0.2 s, equivalent to a low-pass filter, was used to reduce angular fluctuations.

Reporting summary

Further information on research design is available in the Nature Portfolio Reporting Summary linked to this article.

Data availability

All data are available in the Article or its Supplementary Information.

Code availability

Code used in this work is available via GitHub at https://github.com/XiaoxiangGao/single_transducer_project.

References

1. Yu, Y. et al. Biofuel-powered soft electronic skin with multiplexed and wireless sensing for human-machine interfaces. *Sci. Robot.* **5**, eaaz7946 (2020).
2. Bandodkar, A. et al. Sweat-activated biocompatible batteries for epidermal electronic and microfluidic systems. *Nat. Electron.* **3**, 554–562 (2020).
3. Liu, Y. et al. Epidermal mechano-acoustic sensing electronics for cardiovascular diagnostics and human-machine interfaces. *Sci. Adv.* **2**, e1601185 (2016).
4. Zhang, L. et al. Fully organic compliant dry electrodes self-adhesive to skin for long-term motion-robust epidermal biopotential monitoring. *Nat. Commun.* **11**, 4683 (2020).
5. Yu, Y. et al. All-printed soft human-machine interface for robotic physicochemical sensing. *Sci. Robot.* **7**, eabn0495 (2022).
6. Ershad, F. et al. Ultra-conformal drawn-on-skin electronics for multifunctional motion artifact-free sensing and point-of-care treatment. *Nat. Commun.* **11**, 3823 (2020).
7. Moin, A. et al. A wearable biosensing system with in-sensor adaptive machine learning for hand gesture recognition. *Nat. Electron.* **4**, 54–63 (2021).
8. Reaz, M. B. I., Hussain, M. S. & Mohd-Yasin, F. Techniques of EMG signal analysis: detection, processing, classification and applications. *Biol. Proced. Online* **8**, 11–35 (2006).
9. McKeown, M. J. & Radtke, R. Phasic and tonic coupling between EEG and EMG demonstrated with independent component analysis. *J. Clin. Neurophysiol.* **18**, 45–57 (2001).
10. Klotz, T., Gizzi, L. & Röhrle, O. Investigating the spatial resolution of EMG and MMG based on a systemic multi-scale model. *Biomech. Model. Mechanobiol.* **21**, 983–997 (2022).
11. Luo, Y. M., Moxham, J. & Polkey, M. I. Diaphragm electromyography using an oesophageal catheter: current concepts. *Clin. Sci.* **115**, 233–244 (2008).
12. Simão, M., Mendes, N., Gibaru, O. & Neto, P. A review on electromyography decoding and pattern recognition for human-machine interaction. *IEEE Access* **7**, 39564–39582 (2019).
13. Sun, Z., Xi, X., Yuan, C., Yang, Y. & Hua, X. Surface electromyography signal denoising via EEMD and improved wavelet thresholds. *Math. Biosci. Eng.* **17**, 6945–6962 (2020).
14. Solnik, S., DeVita, P., Rider, P., Long, B. & Hortobágyi, T. Teager–Kaiser operator improves the accuracy of EMG onset detection independent of signal-to-noise ratio. *Acta Bioeng. Biomech.* **10**, 65–68 (2008).
15. Eskes, M. et al. sEMG-assisted inverse modelling of 3D lip movement: a feasibility study towards person-specific modelling. *Sci. Rep.* **7**, 17729 (2017).
16. Wakefield, R. J. et al. Musculoskeletal ultrasound including definitions for ultrasonographic pathology. *J. Rheumatol.* **32**, 2485–2487 (2005).

https://doi.org/10.1038/s41928-024-01271-4

17. Sconfienza, L. M. et al. Clinical indications for musculoskeletal ultrasound updated in 2017 by European Society of Musculoskeletal Radiology (ESSR) consensus. *Eur. Radiol.* **28**, 5338–5351 (2018).
18. Wang, C. et al. Continuous monitoring of deep-tissue haemodynamics with stretchable ultrasonic phased arrays. *Nat. Biomed. Eng.* **5**, 749–758 (2021).
19. Hu, H. et al. A wearable cardiac ultrasound imager. *Nature* **613**, 667–675 (2023).
20. Hu, H. et al. Stretchable ultrasonic arrays for the three-dimensional mapping of the modulus of deep tissue. *Nat. Biomed. Eng.* **7**, 1321–1334 (2023).
21. Wang, C. et al. Monitoring of the central blood pressure waveform via a conformal ultrasonic device. *Nat. Biomed. Eng.* **2**, 687–695 (2018).
22. Wang, F. et al. Flexible Doppler ultrasound device for the monitoring of blood flow velocity. *Sci. Adv.* **7**, eabi9283 (2021).
23. Gao, X. et al. A photoacoustic patch for three-dimensional imaging of hemoglobin and core temperature. *Nat. Commun.* **13**, 7757 (2022).
24. AlMohimeed, I. & Ono, Y. Ultrasound measurement of skeletal muscle contractile parameters using flexible and wearable single-element ultrasonic sensor. *Sensors* **20**, 3616 (2020).
25. Wang, Z. et al. Ultrasonography and electromyography based hand motion intention recognition for a trans-radial amputee: a case study. *Med. Eng. Phys.* **75**, 45–48 (2020).
26. Ortenzi, V., Tarantino, S., Castellini, C. & Cipriani, C. Ultrasound imaging for hand prosthesis control: a comparative study of features and classification methods. In *2015 IEEE International Conference on Rehabilitation Robotics (ICORR)* 1–6 (IEEE, 2015).
27. Oakley, C. G. Calculation of ultrasonic transducer signal-to-noise ratios using the KLM model. *IEEE Trans. Ultrason. Ferroelectr. Freq. Control* **44**, 1018–1026 (1997).
28. Yang, X., Yan, J., Fang, Y., Zhou, D. & Liu, H. Simultaneous prediction of wrist/hand motion via wearable ultrasound sensing. *IEEE Trans. Neural Syst. Rehabil. Eng.* **28**, 970–977 (2020).
29. Xue, X. et al. Development of a wearable ultrasound transducer for sensing muscle activities in assistive robotics applications. *Biosensors* **13**, 134 (2023).
30. McCool, F. D. & Tzelepis, G. E. Dysfunction of the diaphragm. *N. Engl. J. Med.* **366**, 932–942 (2012).
31. Tuinman, P. R. et al. Respiratory muscle ultrasonography: methodology, basic and advanced principles and clinical applications in ICU and ED patients—a narrative review. *Intensive Care Med.* **46**, 594–605 (2020).
32. DiNino, E., Gartman, E. J., Sethi, J. M. & McCool, F. D. Diaphragm ultrasound as a predictor of successful extubation from mechanical ventilation. *Thorax* **69**, 431–435 (2014).
33. Guarracino, F. et al. Lung, heart, vascular, and diaphragm ultrasound examination of COVID-19 patients: a comprehensive approach. *J. Cardiothorac. Vasc. Anesth.* **35**, 1866–1874 (2021).
34. Gottesman, E. & McCool, F. D. Ultrasound evaluation of the paralyzed diaphragm. *Am. J. Resp. Crit. Care Med.* **155**, 1570–1574 (1997).
35. Summerhill, E. M., El-Sameed, Y. A., Glidden, T. J. & McCool, F. D. Monitoring recovery from diaphragm paralysis with ultrasound. *Chest* **133**, 737–743 (2008).
36. Pirompanich, P. & Romsaiyut, S. Use of diaphragm thickening fraction combined with rapid shallow breathing index for predicting success of weaning from mechanical ventilator in medical patients. *J. Intensive Care* **6**, 6 (2018).
37. Krisanaprakornkit, T., Sriraj, W., Piyavhatkul, N. & Laopaiboon, M. Meditation therapy for anxiety disorders. *Cochrane Database Syst. Rev.* 10.1002/14651858.CD004998.pub2 (2006).
38. Dries, D. J., McGonigal, M. D., Malian, M. S., Bor, B. J. & Sullivan, C. Protocol-driven ventilator weaning reduces use of mechanical ventilation, rate of early reintubation, and ventilator-associated pneumonia. *J. Trauma* **56**, 943–952 (2004).
39. Roux, F., D'Ambrosio, C. & Mohsenin, V. Sleep-related breathing disorders and cardiovascular disease. *Am. J. Med.* **108**, 396–402 (2000).
40. Conrad, A. et al. Psychophysiological effects of breathing instructions for stress management. *Appl. Psychophysiol. Biofeedback* **32**, 89–98 (2007).
41. Pfaltz, M. C., Michael, T., Grossman, P., Blechert, J. & Wilhelm, F. H. Respiratory pathophysiology of panic disorder: an ambulatory monitoring study. *Psychosom. Med.* **71**, 869–876 (2009).
42. Julious, S. A. *Sample Sizes for Clinical Trials* (Chapman and Hall/CRC, 2023).
43. Barnes, P. J. Small airway fibrosis in COPD. *Int. J. Biochem. Cell Biol.* **116**, 105598 (2019).
44. Jones, R. L., Noble, P. B., Elliot, J. G. & James, A. L. Airway remodelling in COPD: it's not asthma! *Respirology* **21**, 1347–1356 (2016).
45. Pallotti, A., Orengo, G. & Saggio, G. Measurements comparison of finger joint angles in hand postures between an sEMG armband and a sensory glove. *Biocybern. Biomed. Eng.* **41**, 605–616 (2021).
46. Kim, K. K. et al. A substrate-less nanomesh receptor with meta-learning for rapid hand task recognition. *Nat. Electron.* 6, 64–75 (2022).
47. Zheng, Y.-P., Chan, M., Shi, J., Chen, X. & Huang, Q.-H. Sonomyography: monitoring morphological changes of forearm muscles in actions with the feasibility for the control of powered prosthesis. *Med. Eng. Phys.* **28**, 405–415 (2006).
48. Dhawan, A. S. et al. Proprioceptive sonomyographic control: a novel method for intuitive and proportional control of multiple degrees-of-freedom for individuals with upper extremity limb loss. *Sci. Rep.* **9**, 9499 (2019).
49. Kotses, H., Harver, A. & Humphries, C. T. Home monitoring in asthma self-management. *J. Asthma* **43**, 649–655 (2006).
50. Côté, J., Cartier, A., Malo, J. L., Rouleau, M. & Boulet, L. P. Compliance with peak expiratory flow monitoring in home management of asthma. *Chest* **113**, 968–972 (1998).
51. Donaldson, G., Seemungal, T. A., Bhowmik, A. & Wedzicha, J. Relationship between exacerbation frequency and lung function decline in chronic obstructive pulmonary disease. *Thorax* **57**, 847–852 (2002).
52. Goligher, E. C. et al. Mechanical ventilation-induced diaphragm atrophy strongly impacts clinical outcomes. *Am. J. Resp. Crit. Care Med.* **197**, 204–213 (2018).
53. Thille, A. W., Harrois, A., Schortgen, F., Brun-Buisson, C. & Brochard, L. Outcomes of extubation failure in medical intensive care unit patients. *Crit. Care Med.* **39**, 2612–2618 (2011).
54. Li, S., Chen, Z. & Yan, W. Application of bedside ultrasound in predicting the outcome of weaning from mechanical ventilation in elderly patients. *BMC Pulm. Med.* **21**, 217 (2021).
55. DiNino, E., Gartman, E. J., Sethi, J. M. & McCool, F. D. Diaphragm ultrasound as a predictor of successful extubation from mechanical ventilation. *Thorax* **69**, 423–427 (2014).
56. Liu, Y., Zhang, S. & Gowda, M. NeuroPose: 3D hand pose tracking using EMG wearables. In *Proc. Web Conference 2021* 1471–1482 (ACM, 2021).
57. Côté-Allard, U. et al. Deep learning for electromyographic hand gesture signal classification using transfer learning. *IEEE Trans. Neural Syst. Rehabil. Eng.* **27**, 760–771 (2019).
58. Jensen, J. A. Field: a program for simulating ultrasound systems. In *10th Nordic-Baltic Conference on Biomedical Imaging* 351–353 (Citeseer, 1996).

59. Shahgholi, L. et al. Diaphragm depth in normal subjects. *Muscle Nerve* **49**, 666–668 (2014).

Acknowledgements

The system was based on research sponsored by the National Institutes of Health (NIH) grant no. 1R21EB025521-01 (S.X.), grant no. 1R21EB027303-01A1 (S.X.), grant no. 3R21EB027303-02S1 (S.X.) and grant no. 1R01 EB033464-01 (S.X.). The content is solely the responsibility of the authors and does not necessarily represent the official views of the NIH. All the biological experiments were conducted in accordance with the ethical guidelines with the approval of the Institutional Review Board of the University of California San Diego.

Author contributions

X.G. and S.X. conceived the study and designed the experiments. X.G., X.C., W.Y., S.Q., F.Z. and Z.L. performed the experiments. X.G. processed the data. M.L. designed the circuit. L.Y. fabricated the 3D-printed mould. J.L. recruited the patients. X.G., X.C., M.L., J.L. and S.X. wrote the manuscript. H. Hu, H. Huang, S.Z., Y.B., X.Y., Y.Z., J.M., X.W., G.P., C.L., R.W., R.S.W., J.W. and J.L. discussed the experimental results and reviewed the manuscript.

Competing interests

The authors declare no competing interests.

Additional information

Supplementary information The online version contains supplementary material available at https://doi.org/10.1038/s41928-024-01271-4.

Correspondence and requests for materials should be addressed to Sheng Xu.

Peer review information *Nature Electronics* thanks Yuan Huang, Alina Rwei and Lizhi Xu for their contribution to the peer review of this work.

Reprints and permissions information is available at www.nature.com/reprints.

Publisher's note Springer Nature remains neutral with regard to jurisdictional claims in published maps and institutional affiliations.

Springer Nature or its licensor (e.g. a society or other partner) holds exclusive rights to this article under a publishing agreement with the author(s) or other rightsholder(s); author self-archiving of the accepted manuscript version of this article is solely governed by the terms of such publishing agreement and applicable law.

© The Author(s), under exclusive licence to Springer Nature Limited 2024

nature portfolio

Corresponding author(s): Sheng Xu

Last updated by author(s): Sep 2, 2024

Reporting Summary

Nature Portfolio wishes to improve the reproducibility of the work that we publish. This form provides structure for consistency and transparency in reporting. For further information on Nature Portfolio policies, see our Editorial Policies and the Editorial Policy Checklist.

Statistics

For all statistical analyses, confirm that the following items are present in the figure legend, table legend, main text, or Methods section.

n/a	Confirmed	
☐	☒	The exact sample size (n) for each experimental group/condition, given as a discrete number and unit of measurement
☐	☒	A statement on whether measurements were taken from distinct samples or whether the same sample was measured repeatedly
☐	☒	The statistical test(s) used AND whether they are one- or two-sided *Only common tests should be described solely by name; describe more complex techniques in the Methods section.*
☒	☐	A description of all covariates tested
☒	☐	A description of any assumptions or corrections, such as tests of normality and adjustment for multiple comparisons
☐	☒	A full description of the statistical parameters including central tendency (e.g. means) or other basic estimates (e.g. regression coefficient) AND variation (e.g. standard deviation) or associated estimates of uncertainty (e.g. confidence intervals)
☒	☐	For null hypothesis testing, the test statistic (e.g. F, t, r) with confidence intervals, effect sizes, degrees of freedom and P value noted *Give P values as exact values whenever suitable.*
☒	☐	For Bayesian analysis, information on the choice of priors and Markov chain Monte Carlo settings
☒	☐	For hierarchical and complex designs, identification of the appropriate level for tests and full reporting of outcomes
☒	☐	Estimates of effect sizes (e.g. Cohen's d, Pearson's r), indicating how they were calculated

Our web collection on statistics for biologists contains articles on many of the points above.

Software and code

Policy information about availability of computer code

Data collection	The data was collected using commercial software Python 3.7 and Matlab 2019b.
Data analysis	The data was analyzed using commercial software Python 3.7, Matlab 2019b and Origin 2021b The demo of the game is coded in Unity 2022.

For manuscripts utilizing custom algorithms or software that are central to the research but not yet described in published literature, software must be made available to editors and reviewers. We strongly encourage code deposition in a community repository (e.g. GitHub). See the Nature Portfolio guidelines for submitting code & software for further information.

Data

Policy information about availability of data

All manuscripts must include a data availability statement. This statement should provide the following information, where applicable:

- Accession codes, unique identifiers, or web links for publicly available datasets
- A description of any restrictions on data availability
- For clinical datasets or third party data, please ensure that the statement adheres to our policy

All data are available in the main text or the supplementary materials.

Research involving human participants, their data, or biological material

Policy information about studies with human participants or human data. See also policy information about sex, gender (identity/presentation), and sexual orientation and race, ethnicity and racism.

Reporting on sex and gender	In our research, all subjects were male. Gender was not considered in the experimental design, as it was determined through self-reporting and was not a variable expected to influence the results.
Reporting on race, ethnicity, or other socially relevant groupings	These are not applicable to our research.
Population characteristics	We recruited three patients who were diagonalized as COPD, aging from 61 to 84. And we recruited 12 healthy subjects, aging from 21 to 34.
Recruitment	We posted recruitment flyers in the office building and the hospital to recruit the healthy volunteer.
Ethics oversight	University of California, San Diego Institutional Review Board

Note that full information on the approval of the study protocol must also be provided in the manuscript.

Field-specific reporting

Please select the one below that is the best fit for your research. If you are not sure, read the appropriate sections before making your selection.

☒ Life sciences ☐ Behavioural & social sciences ☐ Ecological, evolutionary & environmental sciences

For a reference copy of the document with all sections, see nature.com/documents/nr-reporting-summary-flat.pdf

Life sciences study design

All studies must disclose on these points even when the disclosure is negative.

Sample size	For the gesture recognition application, we recruited one subject, as this is a non-clinical proof-of-concept demonstration of the device. For diaphragm monitoring, we recruited 12 healthy subjects to differentiate between two breathing modes. The sample size was initially chosen randomly due to the uncertainty of the mean difference. After data collection from these 12 subjects, we evaluated the statistical power using a paired t-test to confirm that the sample size was sufficient. For patient testing, we recruited three subjects solely to demonstrate different breathing patterns, as no quantitative results were required.
Data exclusions	No data was excluded from analysis
Replication	We did the test on different subjects individually for multiple times. The data collected from different subjects at multiple time stamp shows high similarity, which proves that the reproducibility of all kinds of measurement was good.
Randomization	All subjects was randomly selected by posting flyers.
Blinding	All subjects were only told the experimental process. All subjects did not know test results. The subjects did not participate in data processing.

Reporting for specific materials, systems and methods

We require information from authors about some types of materials, experimental systems and methods used in many studies. Here, indicate whether each material, system or method listed is relevant to your study. If you are not sure if a list item applies to your research, read the appropriate section before selecting a response.

Materials & experimental systems

n/a	Involved in the study	
☒	☐	Antibodies
☒	☐	Eukaryotic cell lines
☒	☐	Palaeontology and archaeology
☒	☐	Animals and other organisms
☒	☐	Clinical data
☒	☐	Dual use research of concern
☒	☐	Plants

Methods

n/a	Involved in the study	
☒	☐	ChIP-seq
☒	☐	Flow cytometry
☒	☐	MRI-based neuroimaging

Plants

Seed stocks	*Report on the source of all seed stocks or other plant material used. If applicable, state the seed stock centre and catalogue number. If plant specimens were collected from the field, describe the collection location, date and sampling procedures.*
Novel plant genotypes	*Describe the methods by which all novel plant genotypes were produced. This includes those generated by transgenic approaches, gene editing, chemical/radiation-based mutagenesis and hybridization. For transgenic lines, describe the transformation method, the number of independent lines analyzed and the generation upon which experiments were performed. For gene-edited lines, describe the editor used, the endogenous sequence targeted for editing, the targeting guide RNA sequence (if applicable) and how the editor was applied.*
Authentication	*Describe any authentication procedures for each seed stock used or novel genotype generated. Describe any experiments used to assess the effect of a mutation and, where applicable, how potential secondary effects (e.g. second site T-DNA insertions, mosiacism, off-target gene editing) were examined.*

nature electronics

Supplementary information

https://doi.org/10.1038/s41928-024-01271-4

A wearable echomyography system based on a single transducer

In the format provided by the authors and unedited

Table of contents

Supplementary Note 1 | Existing wearable devices for noninvasive sensing of the human body

Supplementary Note 2 | Generation and stochasticity of surface EMG signals

Supplementary Note 3 | Can surface EMG measure signals from deep muscles?

Supplementary Note 4 | Limitations of current soft wearable ultrasound transducer arrays

Supplementary Note 5 | Comparison of this study with our previous work

Supplementary Note 6 | Interference sources in the signals and methods to mitigate them

Supplementary Note 7 | Comparison of our wearable ultrasound patch with other reported wireless sensors

Supplementary Note 8 | Bland-Altman analysis

Supplementary Note 9 | Techniques for recognizing and tracking hand gestures

Supplementary Note 10 | Frame rate of hand gesture tracking using EcMG

Supplementary Note 11 | Detection depth and data acquisition time

Supplementary Note 12 | Angle estimation based on the accelerometer and magnetometer

Supplementary Note 13 | Improving the accuracy and generalization capability with a transducer array

Supplementary Fig. 1 | Propagation of an action potential along and outside the muscle fiber.

Supplementary Fig. 2 | Design and fabrication of the fPCB.

Supplementary Fig. 3 | Power consumption of key components in the fPCB.

Supplementary Fig. 4 | Cross-sectional architecture of the wearable single-channel ultrasound system.

Supplementary Fig. 5 | Ultrasound coupling properties of adhesive silicone (Silbione).

Supplementary Fig. 6 | Comparison among different ultrasound systems.

Supplementary Fig. 7 | Serpentine connector of the fPCB for motion isolation.

Supplementary Fig. 8 | Schematic circuit diagrams of the analog front-end components.

Supplementary Fig. 9 | Schematic circuit diagrams of the digital front-end components.

Supplementary Fig. 10 | Schematic illustration of high-voltage driving pulses.

Supplementary Fig. 11 | Impulse response measurements of the single-transducer ultrasound system.

Supplementary Fig. 12 | Characterization of the axial resolution.

Supplementary Fig. 13 | Simulated sound fields of single transducers with different sizes.

Supplementary Fig. 14 | Schematics of the sound field scanning system.

Supplementary Fig. 15 | Different modes of detecting the diaphragm.

Supplementary Fig. 16 | Simultaneous measurements of the diaphragm with the single-transducer system and a commercial probe.

Supplementary Fig. 17 | Comparison between conventional electromyography and our echomyography for diaphragm monitoring.

Supplementary Fig. 18 | Testing potential motion artefacts during running on a treadmill.

Supplementary Fig. 19 | *t*-SNE plots of M-mode images under different respiration modes.

Supplementary Fig. 20 | M-mode images of subjects 1, 2, and 3 during abdominal and thoracic respirations.

Supplementary Fig. 21 | M-mode images of subjects 4, 5, and 6 during abdominal and thoracic respirations.

Supplementary Fig. 22 | M-mode images of subjects 7, 8, and 9 during abdominal and thoracic respirations.

Supplementary Fig. 23 | M-mode images of subjects 10, 11, and 12 during abdominal and thoracic respirations.

Supplementary Fig. 24 | Components of the forearm muscles.

Supplementary Fig. 25 | Comparison of data acquisition and temporal resolution between conventional electromyography and the ultrasound system in this work.

Supplementary Fig. 26 | Surface EMG is insensitive to normal finger and wrist motions.

Supplementary Fig. 27 | Calibration of strain sensors.

Supplementary Fig. 28 | Calibration of the magnetometer outputs.

Supplementary Fig. 29 | Flowchart of training and testing of deep learning-based continuous hand gesture tracking.

Supplementary Fig. 30 | RF signals as the fingers bend and the wrist rotates.

Supplementary Fig. 31 | Framework of the deep neural network for hand gesture tracking.

Supplementary Fig. 32 | Comparison between EMG and EcMG when the hand was constrained.

Supplementary Table 1 | Comparison between the device in this study and our previously reported works.

Supplementary Table 2 | Specifics of key components in the PCB.

Supplementary Table 3 | Comparison with other fully integrated wearable ultrasound devices.

Supplementary Table 4 | Comparison among different EcMG studies for hand gesture recognition.

Supplementary Table 5 | Accuracies of hand gesture recognition based on EMG and EcMG.

Caption for Supplementary Video 1

Caption for Supplementary Video 2

Caption for Supplementary Video 3

References

Supplementary Note 1 | Existing wearable devices for noninvasive sensing of the human body

Many wearable electronic devices have been reported in the past decade for sensing physiological signals from the human body. These devices usually have small form factors and soft encapsulation layers to minimize restrictions to body motions. They could sense a wide range of signals from the human body, such as temperature[1], body motion[2], skin curvature[3], contact pressure with surrounding environment[4,5], biochemical components in sweat and interstitial fluids[6,7], and peripheral capillary oxygen saturation[1]. Wearable devices are based on different sensing mechanisms to acquire multimodal parameters, as elaborated in the following.

- Local field potential sensors

Local field potential sensors, such as electromyogram (EMG), use electrodes to collect biopotentials on the skin surface generated by motor units. EMG sensors are widely applied for different applications, such as forearm muscles for hand gesture recognition[8], hind limb muscles for monitoring spinal cord injury[9], respiration muscles for diagnosing breathing functions[10], and facial muscles for managing oropharyngeal swallowing disorder[11], nonverbal expression[12], and oral cancers[13].

- Inertial Measurement Unit (IMU) sensors

IMU sensors commonly contain at least three-axis accelerometers, which can detect body motion and skin surface vibrations in 3D space. Advanced IMU sensors also integrate three-axis gyroscopes that measure angular rate and three-axis magnetometers that measure magnetic field surrounding the system. IMU sensors can be attached to different body positions, like chest, neck, arm, and hand. Analyzing the data of IMU sensors can extract the heart rate[1], respiration rate[1], speech[14], pruritus[15], and body orientation[2].

- Strain and pressure sensors

Strain and pressure sensors are usually composed of resistive materials or capacitive structures that respond to deformation or pressure. They are widely used for the detection of skin surface motion and force to monitor arterial pulsation[16], facial expressions[17], muscle activities[18], and human-prosthesis interface[4]. But they can only detect vibrations on the skin surface. Although vibrations in deep tissues can propagate to the skin surface if the vibration magnitude is large enough, like heartbeat, the vibration on the surface can only reveal very limited information, such as heart rate. Capturing more comprehensive information, such as the volume change of heart chamber, blood perfusion of aorta, and diaphragm contraction, requires direct accurate measurements of deep tissues.

- Optical sensors

Optical devices composed of light-emitting diodes (LEDs) and photodetectors emit light into tissues and measure reflected optical intensity. The reflected light intensity reveals the optical absorption and scattering properties of tissues. Usually, several LEDs at different wavelengths are used together to measure tissue properties, including blood oxygen saturation[1,19], cerebral hemodynamics[20], and blood pressure[21]. Because light diffuses in tissues, these devices only measure average properties of a tissue volume. Therefore, it is challenging to measure deep tissue properties with high-spatial resolution.

- Temperature sensors

Temperature sensors[1,2,4,19] based on electrical resistance changes are usually used to monitor the skin surface temperature. A dual temperature sensing[2] mechanism was applied for monitoring core body temperatures at a depth of ~1 cm. Temperature sensors based on photoacoustic technologies can noninvasively map temperature distributions at a depth of ~2 cm[22].

- Electrochemical sensors

Wearable electrochemical sensors continuously monitor the molecular components in biofluids, such as sweat[23], interstitial fluids[24], saliva[25], and tear[26]. Although these biofluids are only from the skin surface or shallow tissues, there are some correlations of molecular compositions between these biofluids and blood[27].

- Electrical impedance sensors

Electrical impedance tomography measures electrical impedances by an electrode array, which is suitable for noninvasive deep tissue monitoring. It is easy to be applied to monitoring large organs, like heart[28] and lung[29]. The spatial resolution is positively correlated to the number of electrodes for electrical impedance imaging. Therefore, a large number of electrodes are usually required to improve the spatial resolution, which increases the complexity and form factor of the whole system.

- Ultrasound sensors

Ultrasound transducers actively emit ultrasound waves into tissues and receive reflected waves for deep tissue sensing. Biomedical ultrasound waves usually have a short wavelength of tens to hundreds of micrometers, leading to high spatial resolution. Wearable ultrasound transducer arrays have high penetration depth (more than 14 cm) and high spatial resolution (better than 1 mm), as shown in the applications of monitoring central blood pressure[30], blood flow[31,32], heart chamber motion[33], hemoglobin distribution[22], and tissue modulus[34].

Supplementary Note 2 | Generation and stochasticity of surface EMG signals

A motor unit is the smallest system controlling muscle contraction. One motor unit is composed of a motor neuron, a neuron axon, and muscle fibers connected to axon branches[35]. The brain controls muscles by sending an electrical signal through the upper motor neuron to the spinal cord, the lower motor neuron, and finally the muscle fiber, causing muscle contraction. One motor unit firing instance means the motor unit receives a signal from the brain. Because one motor unit contains multiple muscle fibers, summation of electrical potentials of all muscle fibers is the motor unit action potential. Finally, an EMG signal is the algebraic summation of action potentials of fired motor units.

Surface EMG electrodes can noninvasively measure the EMG signals through electrolytic conduction, where the current can flow from tissues to the electrodes[36]. The surface EMG signal measured by an electrode on the skin surface can be mathematically modeled as[37]:

$$x(t) = \sum_{i}^{N} m_i(t) = \sum_{i}^{N} \sum_{j}^{M_i} \delta(t - t_{ij}) * s_i(t) + n(t).$$

(1)

$x(t)$ is the measured surface EMG signal; t is the time; $m_i(t)$ is the action potential trace of the i^{th} motor unit, which is the temporal convolution between the firing instant $\delta(t\text{-}t_{ij})$ and the action potential waveform $s_i(t)$ of the i-th motor unit; $n(t)$ is the noise; t_{ij} is the moment of the j-th firing instance of i-th motor unit; N is the number of motor units; and M_i is the number of firing instances of the i^{th} motor unit. The firing rate of a motor unit and the number of fired motor units are both random. These factors make the surface EMG signal $x(t)$ inherently random for different measurements. Furthermore, the action potential waveform is bi-phasic or tri-phasic, which means it has both positive and negative phases[35]. Because of the randomness of firing of each motor unit and a low level of synchronization of firing between different motor units, the algebraic summation of motor unit action potentials could cause in-phase (enhancement) or out-of-phase (cancellation) summation. This also makes surface EMG signals inconsistent for different measurements.

Supplementary Note 3 | Can surface EMG measure signals from deep muscles?

Surface EMG is a non-invasive method that assesses the electrical activities of muscles by using electrodes placed on the skin surface. The efficacy of surface EMG in measuring signals from deep muscles is reliant on a variety of factors, including the size and location of the muscle, the thickness and conductivity of the surrounding tissues (such as skin and fat), and the attributes (such as the impedance, size) and placement of the electrodes. In general, surface EMG is more suitable for measuring signals from superficial muscles located near the skin surface, because the signals of electrical activities of deeper muscles are often attenuated by the overlying tissues. Nonetheless, through appropriate electrode placement and signal processing techniques, it may be possible to obtain useful surface EMG signals from certain deep muscles.

Supplementary Note 4 | Limitations of current soft wearable ultrasound transducer arrays

Soft wearable ultrasound transducer arrays with non-constraining integration on the human body allow continuous monitoring of deep tissues[30,31]. An array with many ultrasound transducers can provide more detailed information of muscles than one single transducer, which can further enhance the functionality, such as improving the accuracy of hand gesture tracking. However, a soft transducer array has uncertain morphologies when integrated on curved dynamic skin surface, resulting in unknown locations and orientations of the transducer elements in the array and thus inaccurate beamforming[31]. In addition, these arrays are still tethered to external bulky electrical controlling systems through wires, which would largely limit the subject mobility in daily applications.

In this work, we designed and fabricated a compact electrical system that integrated a single transducer, an electrical circuit, and a battery, with all components encapsulated in soft silicone elastomer. We would like to bring to the community that the data from a single-transducer ultrasound device is sufficient to infer health status of some respiratory patient groups and to reveal the muscle distributions for human machine interface. The single-transducer ultrasound device substantially simplifies the circuit components, lowers power consumption, and reduces the burden of data collection and processing. The final device could be attached to the skin without any tethering wires, suitable for daily monitoring applications. Potential applications of the fully integrated soft wearable ultrasound system include continuous tracking of arterial wall motions at great depth as a surrogate for blood pressure, measuring the sizes and motions of cardiac chambers to assess the anatomical and functional abnormalities of the heart, and evaluating the bladder volume for timely warning of patients with urinary incontinence.

Supplementary Note 5 | Comparison of this study with our previous work

The uniqueness of this device compared to our previously reported works can be summarized in terms of transducer array design, system integration level, applications, and deep learning algorithm, as shown in the Supplementary Table 1. Details are discussed below:

(1) Our previous research focused on fabricating ultrasound devices with multiple channels to achieve maximum signal quality and imaging capabilities. In this study, we demonstrate a device with a single transducer, substantially simplifying system complexity in terms of fabrication, circuitry, control logic, and device size, weight and power consumption while realizing health monitoring and human-machine interface simultaneously.

(2) Our previously reported device mainly focused on the ultrasound patch itself. A bundle of signal wires was required to connect the patch and the electrical controlling system, which limited the mobility of ultrasound patches. In this work, leveraging the small form factor of single ultrasound transducer and low burden of data, we specifically developed a fully-integrated circuit for driving the ultrasound transducer and collecting the data. This makes the wireless ultrasound system provide much enhanced mobility to wearers.

(3) Our previous applications primarily focused on biomedical applications such as blood pressure and flow monitoring, heart and brain imaging, and elastography. In this work, we demonstrated that this device can be used for two main applications. First, it can monitor the breathing patterns by tracking diaphragm movements in both healthy subjects and patients with respiratory diseases. Second, the device could be used as a human-machine interface by continuously tracking the hand gestures by analyzing ultrasound radiofrequency signals.

(4) In our previously reported works, deep learning algorithms were applied for segmenting and classifying processed ultrasound images. In this study, we demonstrate the deep learning algorithms can extract rich information from raw radiofrequency signals of only one

single transducer, establishing the connection between muscular ultrasound signals and hand gestures. Therefore, we extend the application scenarios of deep learning in ultrasound signal analysis.

Supplementary Note 6 | Interference sources in the signals and methods to mitigate them

Electromagnetic interference (EMI) in ultrasound systems can be classified into two main categories according to their frequencies: out-of-band noise and in-band noise. To attenuate EMI outside the frequency band of interest, we can use either analog or digital filtering[38]. Sources of such interference commonly include power lines and wireless communication devices like Bluetooth, Wi-Fi, and radio transmitters.

To attenuate EMI that falls within the frequency band of interest, the efficacy of conventional filters is substantially reduced. There are two main EMI sources in this band. First, EMI can be generated by the switching voltage regulators on the integrated PCB. These regulators adjust the voltage by rapidly toggling transistor switches, which operate at or near the ultrasound's operational frequency range and can handle substantial electrical currents, producing substantial EMI. To mitigate this, we physically separated the regulators from noise-sensitive components such as ultrasound transducers and amplifiers. In addition, we temporally separated switching operation from signal receiving and amplification. The switching regulators are deactivated in the ultrasound transmit/receive period (Fig. 2b). When the transmit/receive is finished, the switching regulators are activated again to charge the pulser. Second, other devices in the testing environment, such as wireless chargers and near-field communication systems operating within the megahertz range, may interfere with the ultrasound frequency band.

Because there were not these kinds of devices in our testing environment, such EMIR source is negligible.

Supplementary Note 7 | Comparison of our wearable ultrasound patch with other reported wireless sensors

Our echomyography device has three key advantages compared to the reported sensors in the literature.

First, most of the reported sensors typically involve rigid bulky circuits lacking flexibility[39-41]. This makes it challenging to conform to highly curved, dynamic body surfaces, introducing irritation and uncomfortableness to the skin for long-term wearable applications. In contrast, our system is built on flexible printed circuit boards and engineered with soft packaging, allowing it to conform seamlessly to the human skin. Our design and fabrication techniques can ensure reliable attachment, ultrasound coupling, signal fidelity, and comfort of wearing.

Second, some of the reported sensors still focus on the skin surface sensing. Typically, a wearable lung volume monitoring sensor integrated two polyvinylidene fluoride (PVDF) transducers for independent ultrasound emission and receiving[42]. The generated ultrasound wave propagates on the chest skin surface. Detecting the distance between the two PVDF sensors could infer the lung volume, similar to what a resistance-based strain sensor does[43]. Therefore, this kind of device does not directly capture the deep tissue information. In our work, we applied PZT 1-3 composite as the piezoelectrical transducer whose ultrasound wave penetrates several centimeters below the skin surface. Hence our device can directly capture deep tissue information and provide a high spatial resolution.

Third, previously reported wireless ultrasound sensors rely on traditional signal processing methods, which inherently limit their capabilities and applications. Wearable ultrasound sensors can be based on A-mode to reduce the burden of data collection, transmission, and processing. However, in this case the acquired data is only suitable for distance detection of tissue interfaces. For example, bladder volume can be inferred by sensing the distance between the anterior and posterior walls of the bladder. In this work, we developed deep learning algorithms to analyze the signals from a single-channel transducer and extract much more information than only the distance. Specifically, we demonstrated deep learning algorithms could infer the hand gesture from only one radiofrequency signal trace, which could be used as a wearable human-machine interface. This work is qualitatively different in the data processing methods and applications of wearable ultrasound sensors from the other studies.

Supplementary Note 8 | Bland-Altman analysis

Bland-Altman plot analyzes the agreement between two groups of datasets captured by two measurement techniques. This plot has been widely used in analytical chemistry and biomedicine[44] to compare a new measurement method with the gold standard. X and Y are the datasets measured by the two methods. The x-coordinate of Bland-Altman plot is the average of X and Y while the y-coordinate is the difference between each paired X and Y. In Bland-Altman plot, there are three horizontal lines, representing the mean bias $\overline{d}$, the upper limit of agreement E_{upper} and the lower limit of agreement E_{lower}. They are calculated as:

$$\overline{d} = \frac{1}{n}\sum_{i=1}^{n}\left(Y_i - X_i\right) \tag{2}$$

$$E_{lower} = \overline{d} - 1.96 \times sd \tag{3}$$

$$E_{upper} = \bar{d} + 1.96 \times sd \qquad (4)$$

where *sd* is the standard deviation. 1.96 is the boundary for the 95%-confidence interval in a standard normal distribution.

Supplementary Note 9 | Techniques for recognizing and tracking hand gestures

Recognizing hand gestures means differentiating limited number of specific discrete hand gestures based on measured signals. However, tracking hand gestures requires measuring the bending angles of finger joints and the rotation angles of the wrist continuously. Tracking hand gestures is not limited to several specific discrete gestures, but involves continuously monitoring the angles of finger bending and wrist rotating for each specific discrete hand gesture[45]. There are several techniques for recognizing discrete and tracking continuous hand gestures, including computer vision[46-48], strain sensing[6,49,50], IMU sensing[51], electromyography[52], and ultrasonography[53-55].

- Computer vision

Computer vision uses cameras to acquire photos or depth images of the human body and process them with machine learning algorithms. It can continuously track the motion of fingers and wrist without the need for wearing any sensors. However, the hand can sometimes be occluded by other objects, and the fingers can block each other from the camera. A potential solution is to detect the gesture from multiple views by combining multiple cameras, which increases the cost and complexity of the system. Because the cameras are usually bulky and not portable, this method is not always applicable if the hand is not within the view of cameras. In addition, the light in surrounding environment has a strong influence on the tracking accuracy.

- Strain or IMU sensor-based gloves

Many studies also developed wearable gloves to track the motion of fingers and wrist[56-58]. Researchers usually install a strain sensor on each finger joint to measure the bending of the joints, then the hand gesture can be depicted after the angles of all finger joints are determined. They may also use IMU sensors to measure the movements of fingers and the palm in the 3D space. These wearable gloves can work at any position and in any light environment. But they need many sensors to track the configuration of one hand, resulting in complex wire connections and a large device form factor. Furthermore, gloves are totally inapplicable for amputees.

- Surface EMG

Surface EMG is another widely used technique for recognizing and tracking hand gesture. Surface EMG electrodes detect electrical potential generated by motor units, traveling along muscle fibers[52]. However, surface EMG signals are weak and have low signal to noise ratio during low-level muscle activation, resulting in low classification accuracy for discrete hand gestures[59]. Previous studies have also demonstrated the low accuracy of surface EMG signals for recognizing different facial expressions[12].

- Ultrasonography

As a convenient way to detect muscle activities, ultrasonography has also been demonstrated in recognizing hand gestures[53-55]. Ultrasound can penetrate deeply into tissues and noninvasively image muscle groups during hand motion, including deep muscles that are inaccessible for surface EMG electrodes. However, previous studies by fixing bulky ultrasound probes on the forearm with rigid fixtures are not user-friendly because of the large volume and weight of the setup[53-55]. Furthermore, these studies only demonstrated classifying several specific discrete gestures, unable to track dynamic hand gestures continuously.

In this work, we designed and fabricated a fully integrated single-channel echomyography **(**EcMG) system, which is composed of a compact single ultrasound transducer, a flexible printed circuit board (fPCB) for transducer activation and wireless data communication, and a lithium-polymer battery. The ultrasound system has a small form factor and soft mechanical interface with the skin, making it wearable and user-friendly. The system can continuously measure the motion of muscle groups in the forearm (and other body parts). We also developed a deep neural network to analyze the radiofrequency (RF) data of the single transducer to track the dynamic finger and wrist motions with high accuracy in real time.

Supplementary Note 10 | Frame rate of hand gesture tracking using EcMG

One ultrasound RF signal has a time duration of several tens of microseconds. We can acquire thousands of such RF signals in one second in principle. Each RF signal can be used to predict one hand gesture. So, EcMG can theoretically achieve a frame rate of thousands of Hz. In consideration of the fact that hand gesture does not change too fast, and a lower frame rate can lower the data acquisition frequency and thus power consumption, we designed the system with a frame rate of 50 Hz.

Supplementary Note 11 | Detection depth and data acquisition time

For detecting forearm muscles, we recorded 1024 sampling points per RF signal. Because the sampling rate is 12 MHz, the corresponding data acquisition time is about 1024/12 MHz $\approx$

85 μs. In consideration of the sound speed of about 1540 m/s, the nominal detection depth is about 6.6 cm. The typical thickness of forearm muscles is <6.6 cm. However, because ultrasound waves could experience multiple reflections in the forearm, we could record a signal with a nominal depth greater than the forearm thickness.

Supplementary Note 12 | Angle estimation based on the accelerometer and magnetometer

The IMU sensor (KMX62) in the commercial glove development kit in this work had a three-axis accelerometer and a three-axis magnetometer. Their outputs could be defined as X_{Acc}, Y_{Acc}, Z_{Acc}, X_{Mag}, Y_{Mag}, and Z_{Mag}. Then the roll and pitch angles could be easily calculated based on the following equations[60]:

$$Roll = atan2\left(\frac{Y_{Acc}}{Z_{Acc}}\right) \tag{5}$$

$$Pitch = atan\left(\frac{-X_{Acc}}{Y_{Acc}sin(Roll) + Z_{Acc}cos(Roll)}\right) \tag{6}$$

Function *atan*2 has an output angle range of -180° to 180°, while *atan* has an out angle range of -90° to 90°.

The magnetometer data were used to calculate the yaw angle. However, the magnetic measurement is usually affected by the magnetic field created by the surrounding environment. Assuming no distortion, the output of the magnetometer in three directions should form a spherical surface in the 3D space, with the origin at X_{Mag}=0, Y_{Mag}=0, and Z_{Mag}=0. The environmental magnetic field will shift the center of the sphere by a bias, while the shape of the sphere is maintained. In this work, we adopted a convenient way to eliminate the distortion of the surrounding environment[61]. We spun the IMU sensor in a spherical surface in the 3D space over 1000 periods and collected more than 10000 magnetometer outputs. The average values of the magnetometer in the *X*, *Y*, and *Z* directions were calculated as X_{Offset}, Y_{Offset}, and Z_{Offset}. Then the real magnetometer values were computed according to:

$$X_{Real} = X_{Mag} - X_{Offset} \tag{7}$$

$$Y_{Real} = Y_{Mag} - Y_{Offset} \tag{8}$$

$$Z_{Real} = Z_{Mag} - Z_{Offset} \tag{9}$$

The outputs of the magnetometer before and after the calibration are shown in Supplementary Fig. 21. Obviously, the calibrated magnetometer values were distributed on a spherical surface with the origin at X_{Mag}=0, Y_{Mag}=0, and Z_{Mag}=0. After the calibration, the yaw angle could be calculated by:

$$Yaw = atan2\left(\frac{Y_{Real}}{X_{Real}}\right) \tag{10}$$

However, this equation was only applicable when the sensor was flat, i.e., when the roll and pitch angles were both zero. It was impossible to maintain this condition all the time. Therefore, we compensated the influence of arbitrary roll and pitch by[61]:

$$Yaw = atan2\left(\frac{Y_{Real}cos(Roll) - Z_{Real}cos(Pitch)sin(Roll) + X_{Real}sin(Roll)sin(Pitch)}{X_{Real}cos(Pitch) + Z_{Real}sin(Pitch)}\right) \tag{11}$$

Supplementary Note 13 | Improving the accuracy and generalization capability with a transducer array

For the single transducer, the measured RF signal may change pronouncedly if the detect position changes. To improve the accuracy and generalization capability of this technology for continuous hand gesture tracking, we could extend the single transducer to a transducer array. In this case, the array does not need beamforming as conventional transducer arrays do, because here each transducer would work independently to acquire the RF signals from different angles/locations of muscles. A transducer array can capture multi-channel RF signals from multiple angles/locations, acquiring more comprehensive information of the muscle activity. Even the detection position of the transducer array changes, the multi-channel signals may still keep similar. Therefore, a transducer array could be less sensitive to the placement angles/locations of the transducers, having higher accuracy and generalization capability. Those RF signals from the transducer array could be fed into the deep neural network for processing separately.

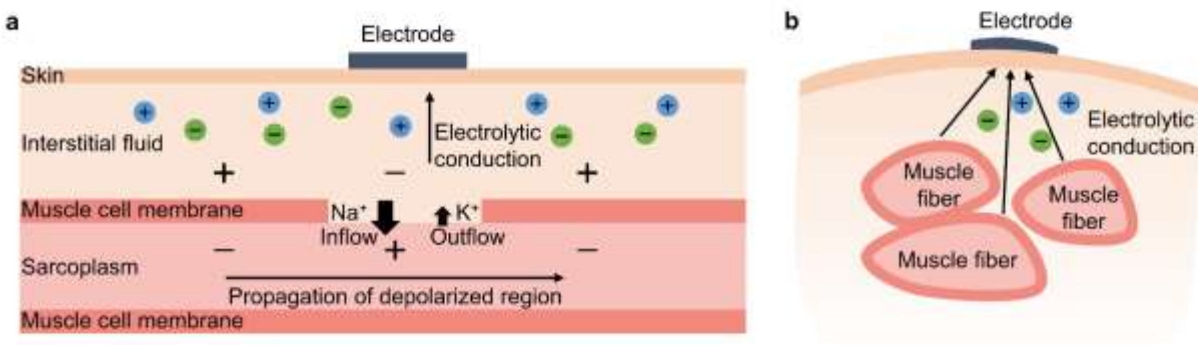

Supplementary Fig. 1 | Propagation of an action potential along and outside the muscle fiber. a, The excitation of a muscle fiber causes depolarization in the muscle cell membrane, which induces an inflow of Na^+, an outflow of K^+, and a potential change at that region[62]. The depolarization area will then be restored to the original state due to active ion pumping[63]. On one hand, the depolarization area travels along the muscle fiber, resulting in the propagation of an action potential. On the other hand, the action potential causes ions in the interstitial fluid to flow, i.e., electrolytic conduction, which can be captured by surface electrodes[36]. **b**, One surface electrode can collect such biopotentials from multiple muscle fibers in the vicinity and thus lack one-to-one correspondence and spatial resolution.

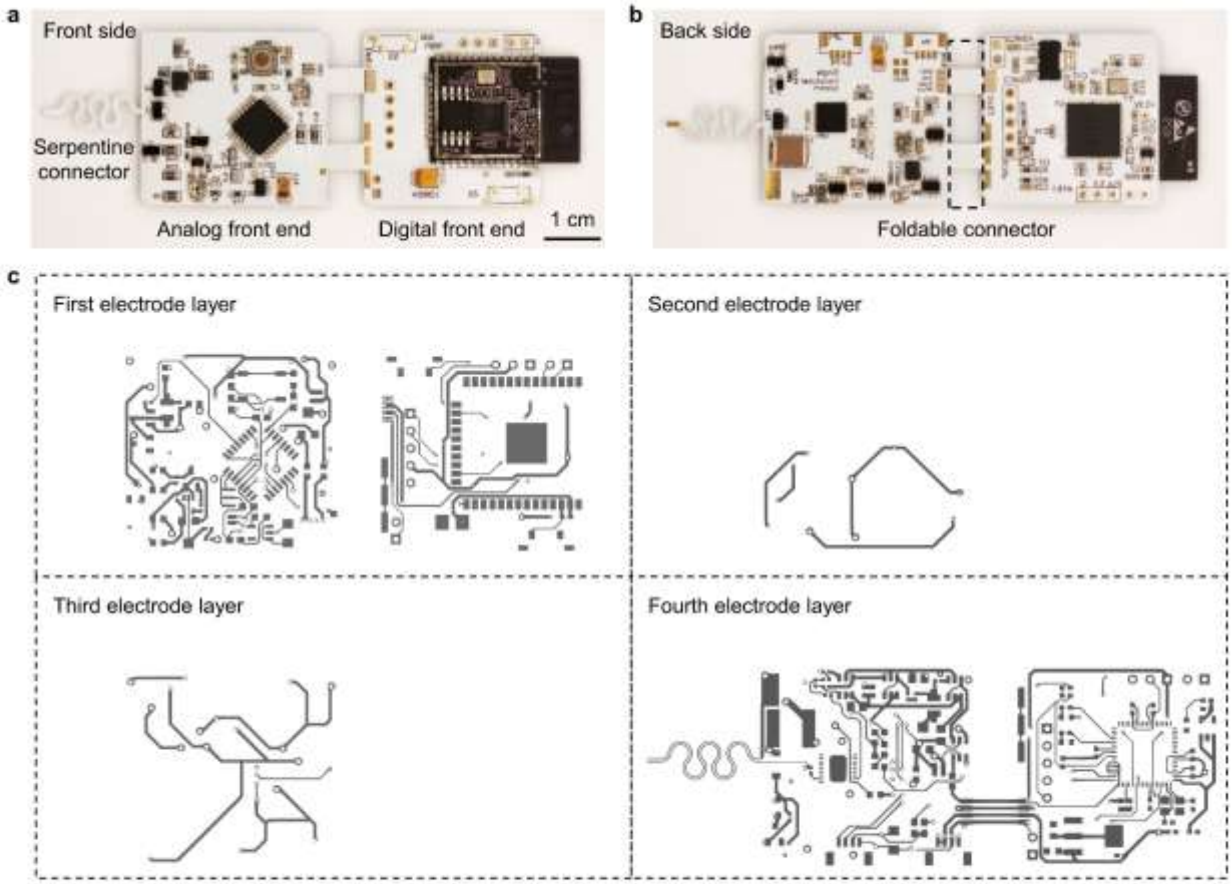

Supplementary Fig. 2 | Design and fabrication of the fPCB. a, Front side of the fPCB, which is composed of an analog front end and a digital front end. The serpentine connector links the circuit board to the single transducer. **b**, Back side of the fPCB. The two sub-boards are linked by a foldable connector. **c**, Four electrode layers of the fPCB to minimize its overall footprint.

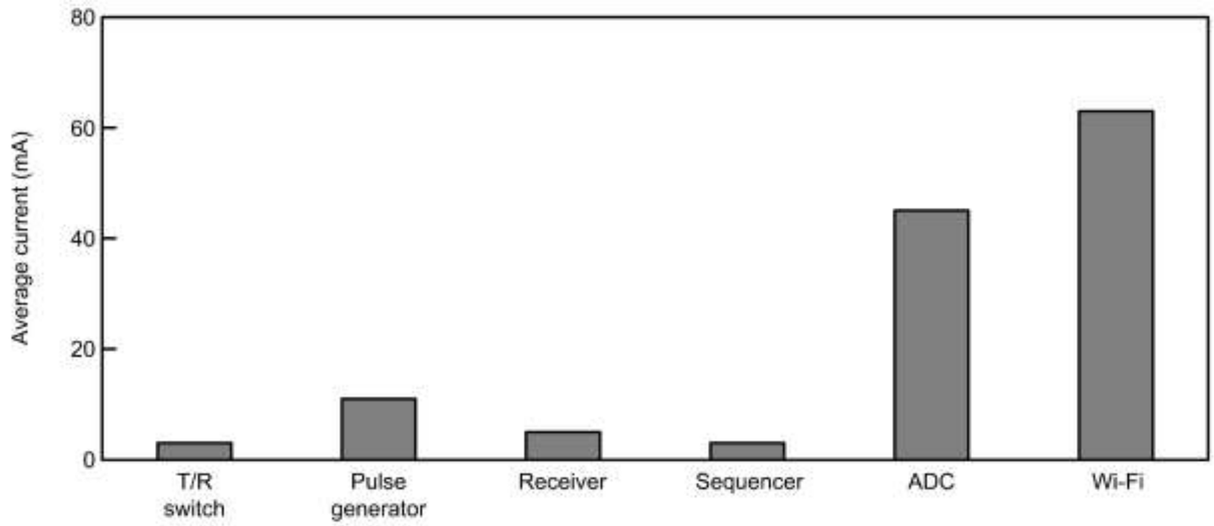

Supplementary Fig. 3 | Power consumption of key components in the fPCB. All components operate at 3.7 V. The Wi-Fi module transmits a group of data to the backend receiver every 20 ms to reduce the power consumption. T/R: transmit/receive. ADC: analog to digital converter. Our ultrasound system used a commercially off-the-shelf lithium battery as the power source, for which 3.7 V is a standard voltage. Because many chips (such as the operational amplifier ADA4895-1ARJZ-R7) can be powered in a range of supply voltages, a 3.7-V battery can directly power the chip. For some chips that 3.7 V is not suitable, we also integrated linear regulators in our PCB circuit, which transformed the 3.7 V to acceptable voltage levels.

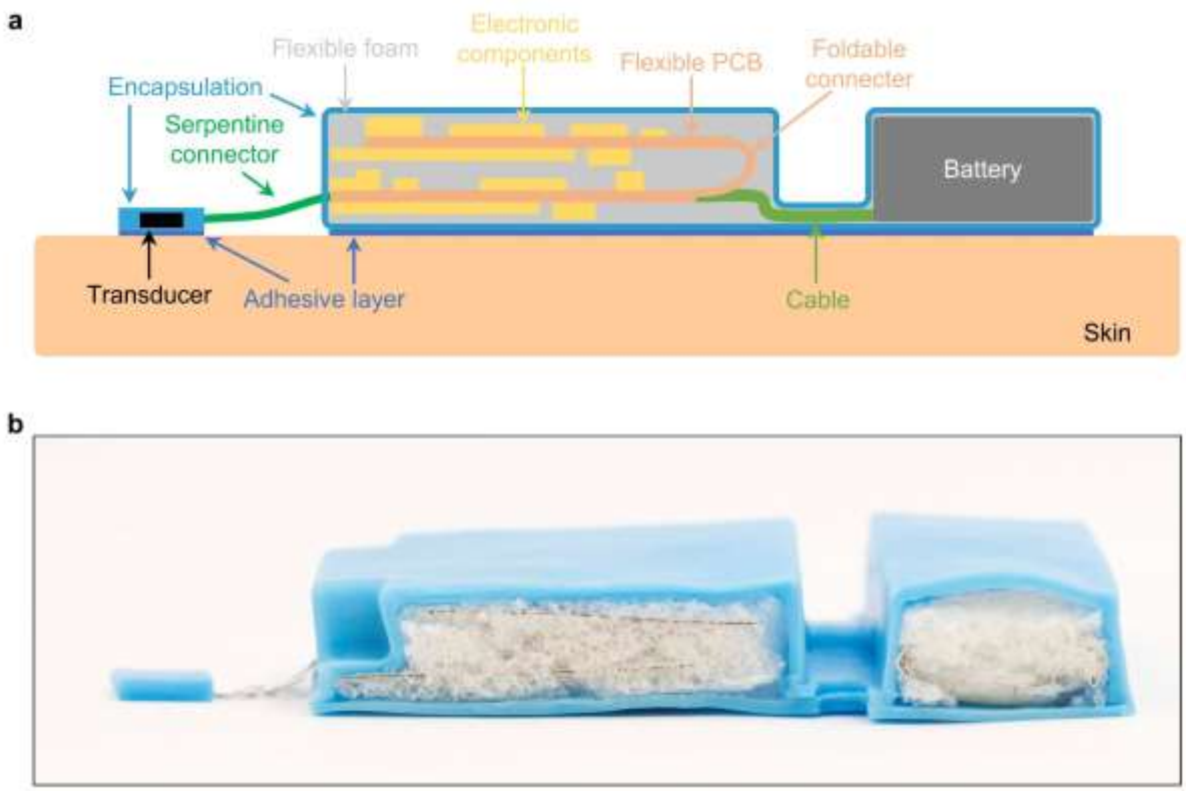

Supplementary Fig. 4 | Cross-sectional architecture of the wearable single-channel ultrasound system. a, Schematics of the cross section of the ultrasound system. The single transducer, fPCB, and battery are all encapsulated in silicone elastomer (Ecoflex 00-30). The patch is attached to the skin with a thin layer of adhesive silicone (Silbione). **b**, Image of the cross section of the ultrasound system.

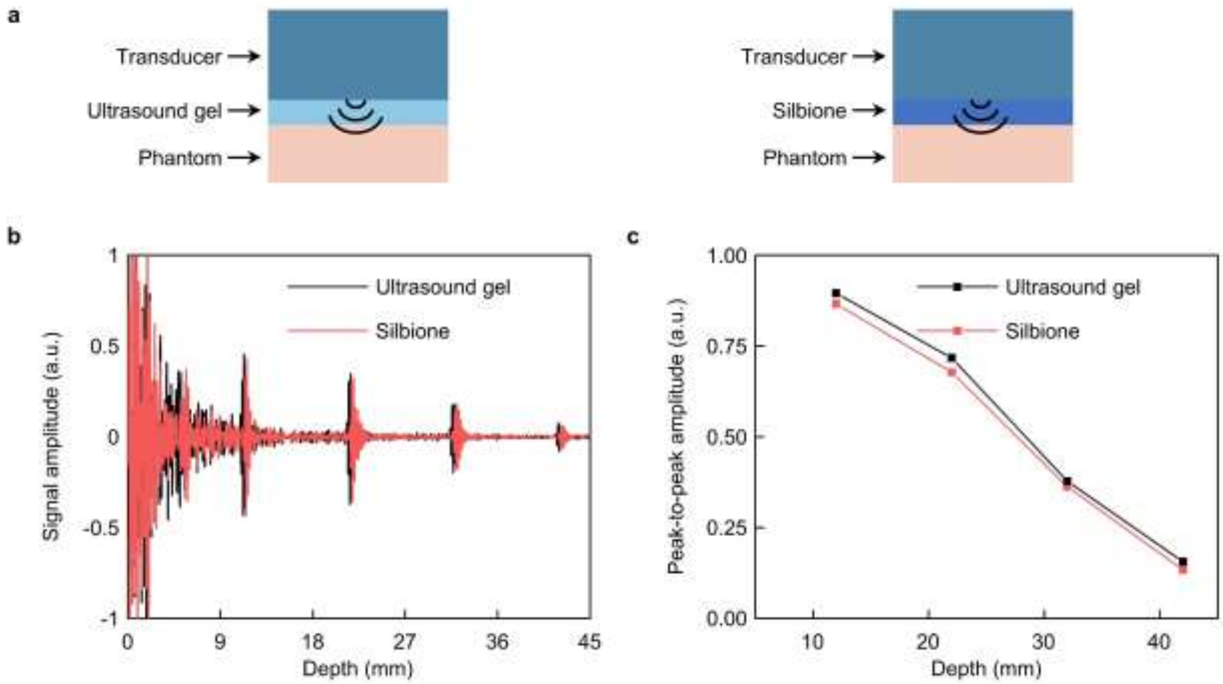

Supplementary Fig. 5 | Ultrasound coupling properties of adhesive silicone (Silbione). a, Schematics showing the comparison of ultrasound transmission properties between the ultrasound gel and Silbione adhesive layer. **b**, Ultrasound echo signals reflected by scatterers in a commercial phantom (CIRS, Model ATS 539) as measured using ultrasound gel and Silbione as the couplant. **c**, Peak-to-peak amplitudes of the signals in **b**. Their similar magnitudes reveal the similar coupling behavior of Silbione to ultrasound gel.

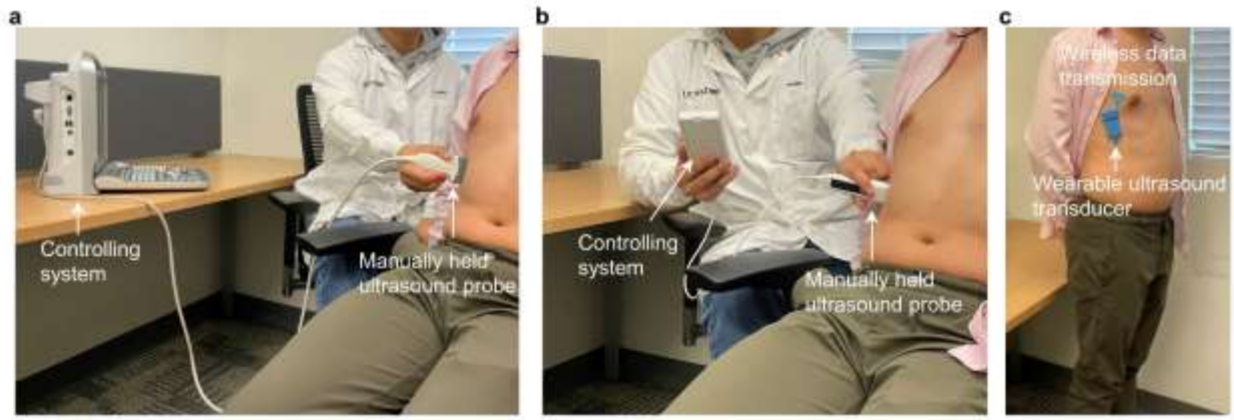

Supplementary Fig. 6 | Comparison among different ultrasound systems. a, A commercial portable ultrasound system with a laptop-sized controller. Operators need to manually hold the bulky ultrasound probe during examination. The subject needs to keep static to reduce the relative motion between the body and the probe. **b**, A commercial portable ultrasound system with a mobile phone-sized controller. Operators also need to manually hold the bulky ultrasound probe during examination and the subject must keep static to reduce any relative motion between the body and the probe. **c**, The fully integrated wearable ultrasound system demonstrated in this work. The entire system has a low form factor and can be attached to the skin without manual holding. The wireless operation substantially reduces restrictions to the human body.

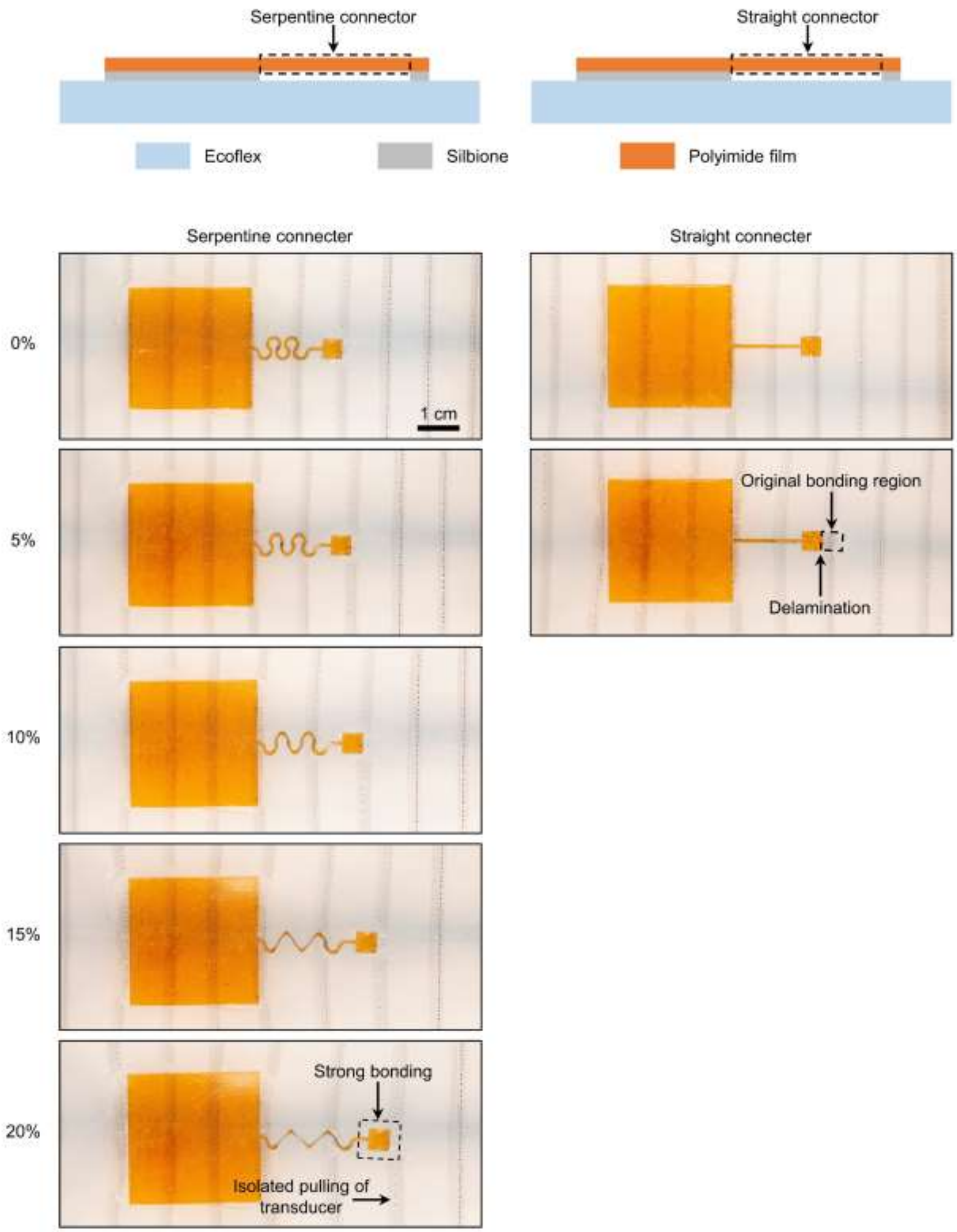

Supplementary Fig. 7 | Serpentine connecter of the fPCB for motion isolation. An Ecoflex substrate with a thickness of 3 mm was used to mimic human tissues. We fabricated two polyimide sheets with shapes similar to the fPCB and the single transducer. One of them has a serpentine connector while the other one has a straight connector. The Ecoflex substrate is bonded with the polyimide sheet with adhesive silicone (Silbione). For the serpentine connector, even if the substrate is stretched up to 20%, the smaller part, which mimics the single transducer, is not pulled by the larger part, which mimics the fPCB. The smaller part is still bonded with the substrate strongly, which means the motion of the fPCB has slight influence on the single transducer. But for the straight connector, the fPCB part has large influence on the single transducer. The delamination between the single transducer and substrate occurs even under only 5% stretching.

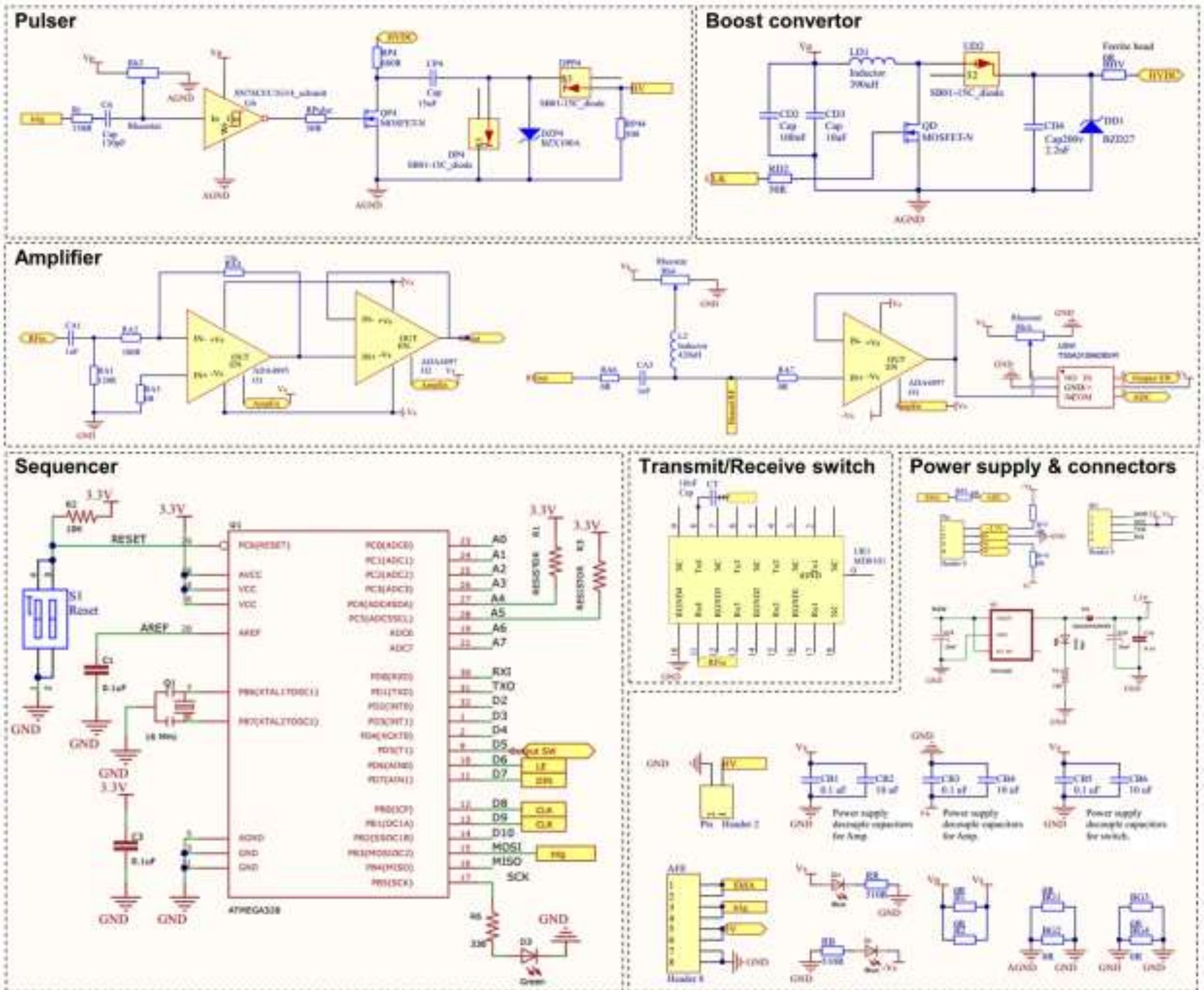

Supplementary Fig. 8 | Schematic circuit diagrams of the analog front-end components. The analog front end includes the pulser, boost convertor, amplifier, sequencer, transmit/receive switch, and power supply and connectors.

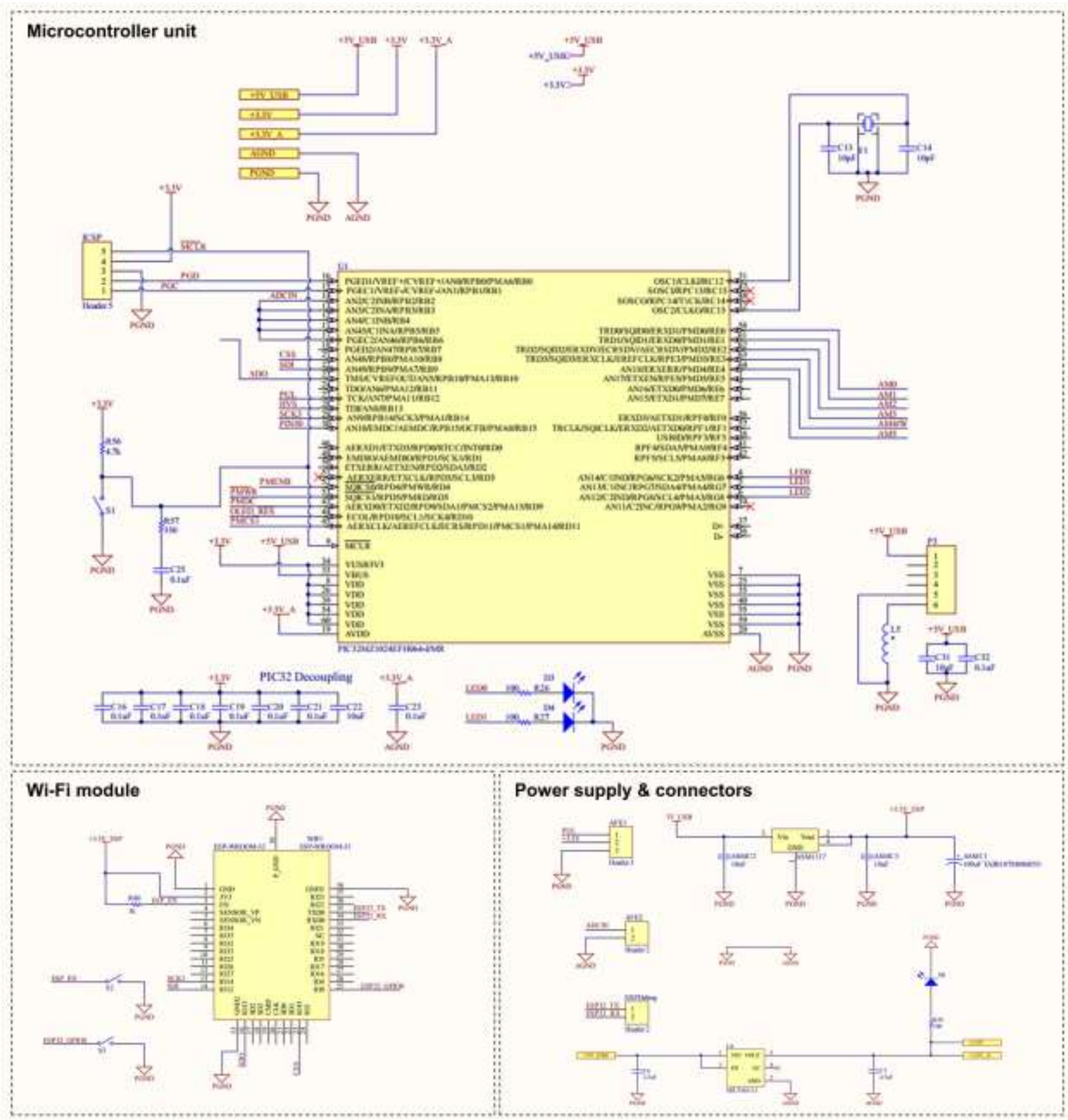

Supplementary Fig. 9 | Schematic circuit diagrams of the digital front-end components. The digital front end includes the microcontroller unit, Wi-Fi module, and power supply and connectors.

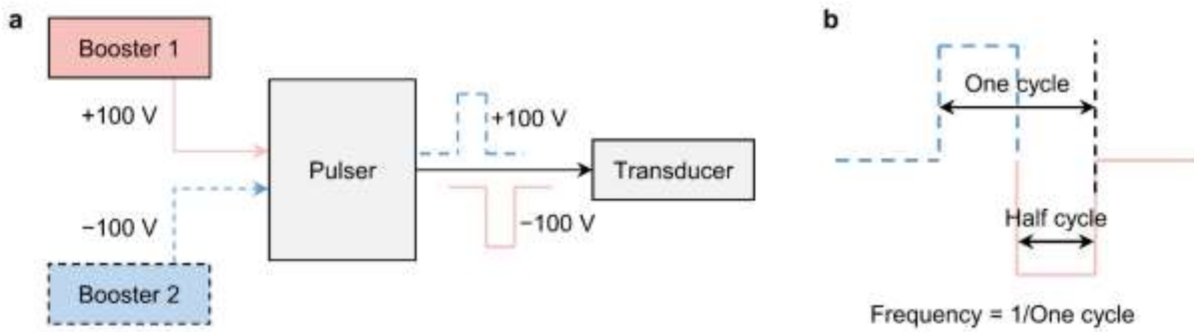

Supplementary Fig. 10 | Schematic illustration of high-voltage driving pulses. a, The booster circuit provides high direct current voltage to the pulser circuit, which then generates a high-voltage pulse wave to drive the transducer. Two booster circuits are required to provide bipolar high voltages, if a bipolar pulse wave is needed. In this work, we only integrated one booster for the positive high voltage supply. Then the pulser circuit only drives the transducer with a negative high-voltage pulse. Both a full cycle and a half cycle pulses can be used to drive the transducer. The half cycle pulse could result in a lower signal amplitude but higher signal bandwidth than the full cycle pulse. **b**, For the bipolar pulse, the frequency equals 1/one full cycle duration. For the half cycle used in this work, the frequency still equals 1/one full cycle duration.

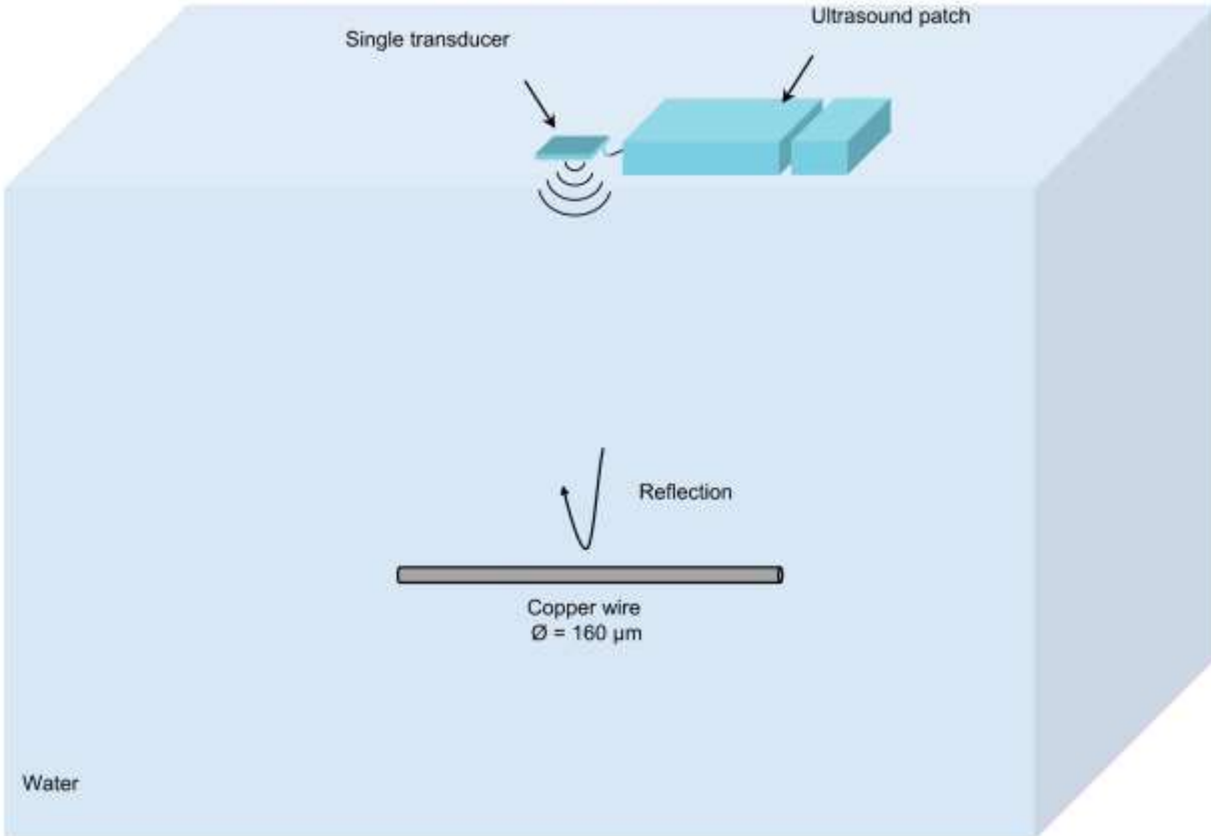

Supplementary Fig. 11 | Impulse response measurements of the single-transducer ultrasound system. The single-transducer ultrasound system is supported on the water surface. It emits a pulse wave in the direction perpendicular to a copper wire (diameter = 160 μm), receives the echo signal, and wirelessly transmits the received signals to a computer for further processing.

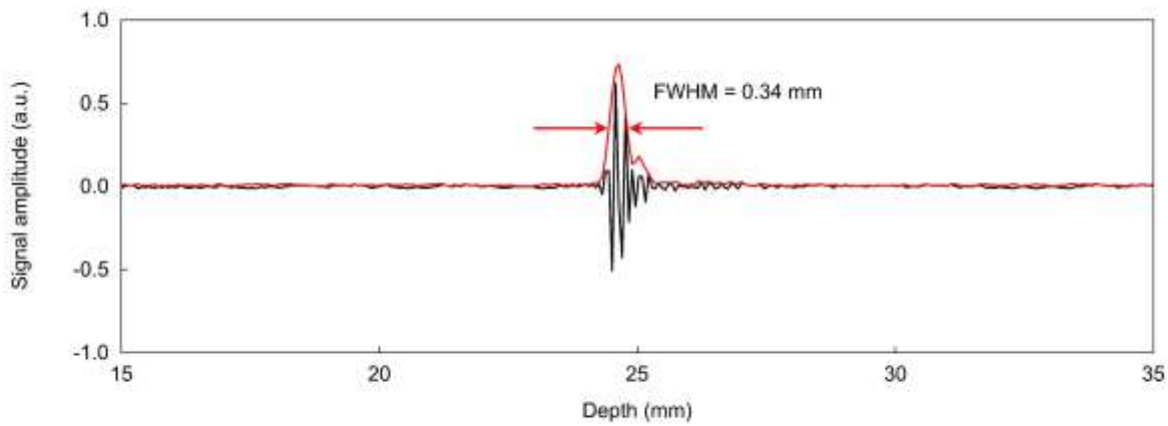

Supplementary Fig. 12 | Characterization of the axial resolution. The spatial resolution is an important metric that characterizes the accuracy of diaphragm thickness measurements. Because our ultrasound system operates at the A-mode, which reflects the dimensions of tissue layers at different depths, the axial resolution represents the spatial resolution of our system. We measured the pulse echo signal of one thin copper wire (diameter = 0.16 mm). The full width at half maximum (FWHM) was calculated from the signal envelope to be 0.34 mm. Therefore, the axial resolution of our system is 0.34 mm.

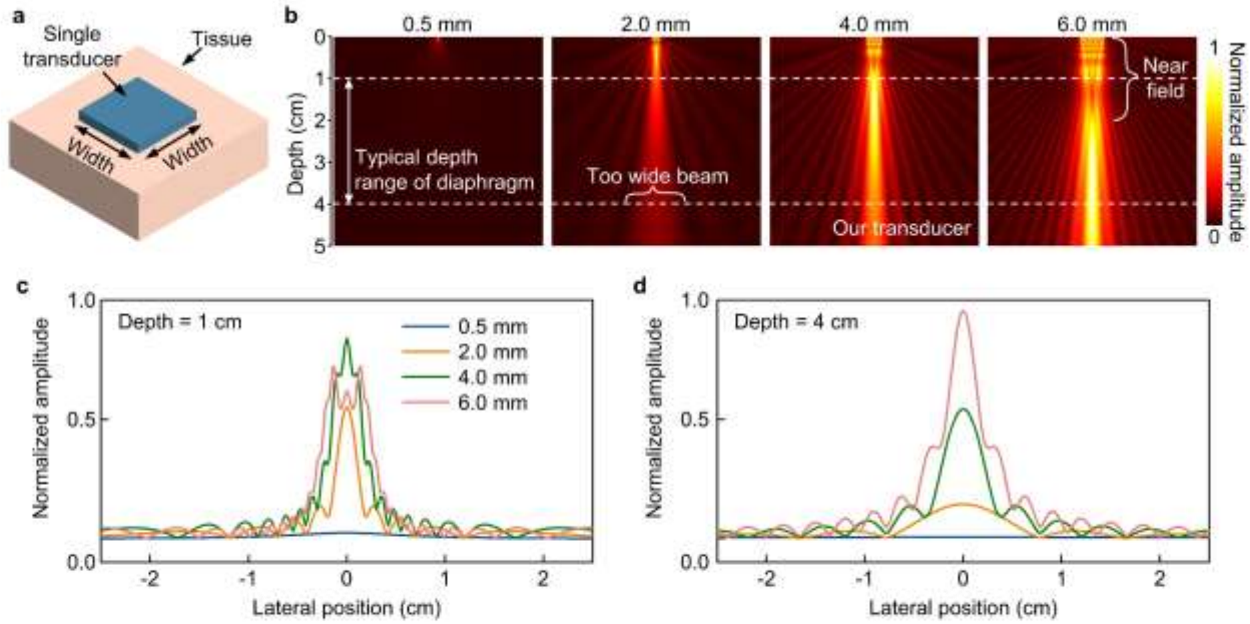

Supplementary Fig. 13 | Simulated sound fields of single transducers with different sizes. a, Schematics of the single transducer on a tissue surface. **b**, Simulated sound fields in the vertical plane of different single transducers. The widths of square single transducers are 0.5 mm, 2.0 mm, 4.0 mm, and 6.0 mm. When the width is small, e.g., 0.5 mm and 2.0 mm, the sound beam is too wide at great depth. When the width is large, e.g., 6.0 mm, the near field of the single transducer is too long. Amplitudes of ultrasound waves fluctuate greatly in the near field region. Ideally, the sound beam should be narrow in the typical diaphragm depth range from 1 to 4 cm. Therefore, 4 mm is selected as the transducer width in this work. **c**, Sound field profiles of the transducers of different widths at the depth of 1 cm. **d**, Sound field profiles of the transducers of different widths at the depth of 4 cm.

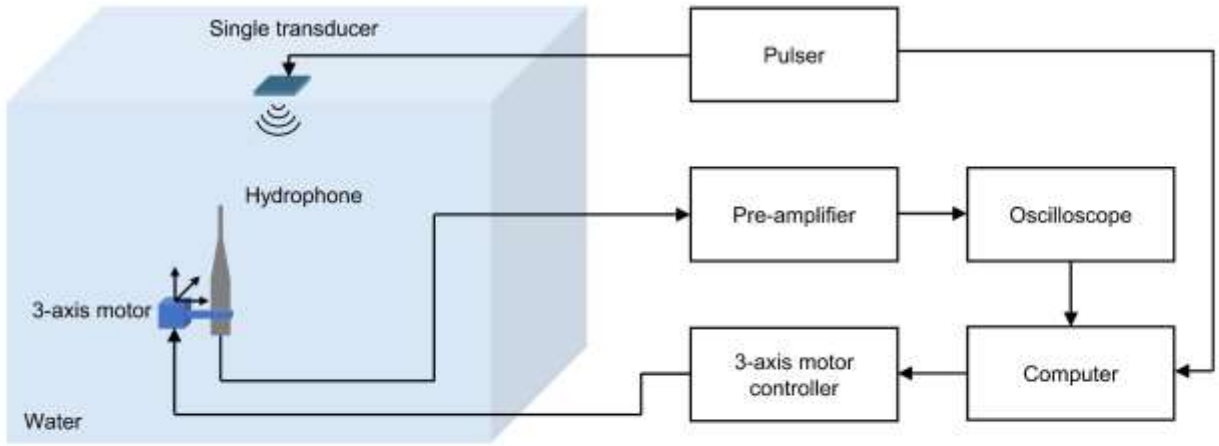

Supplementary Fig. 14 | Schematics of the sound field scanning system. A pulser (Olympus, 5077PR) emits a pulse voltage with an amplitude of 100 V to excite the single transducer. The ultrasound wave emitted from the single transducer is received by the hydrophone (ONDA, Model no. HNP-0400), amplified by the pre-amplifier, digitized by the oscilloscope (PicoScope 5000), and then recorded by the computer. The pulser sends a trigger signal to the computer to synchronize the wave transmission and receiving. The peak-to-peak value of the received signal is extracted as the sound field amplitude at the scanning point. A three-axis motor controlled by the computer moves the hydrophone to map the sound field in the 3D space.

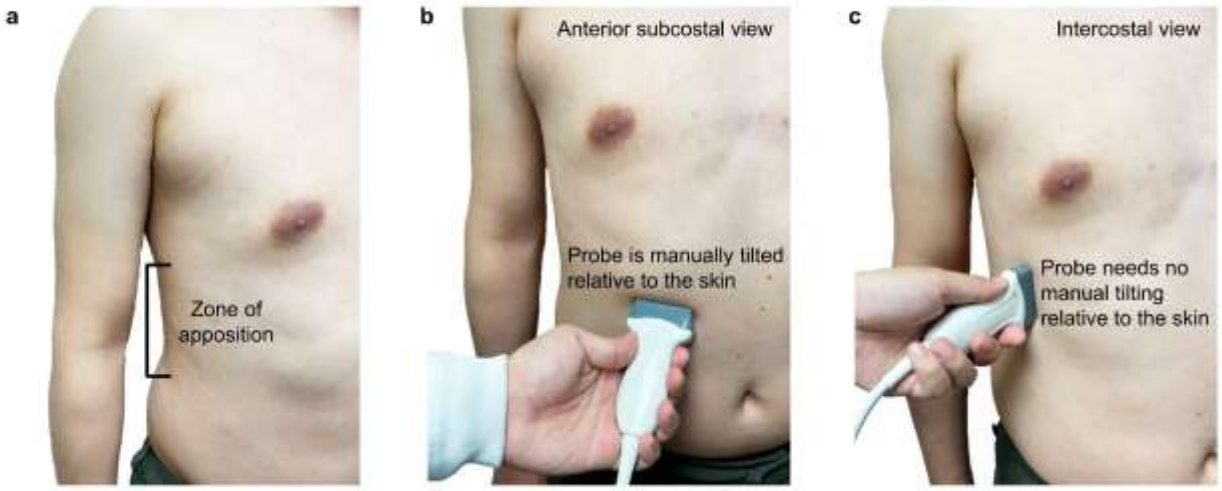

Supplementary Fig. 15 | Different modes of detecting the diaphragm. a, The zone of apposition is the vertical area that is directly behind the inner aspect of the lower chest wall and the rib cage. Anterior subcostal view and intercostal view within the zone of apposition are widely used for diagnosing diaphragm in clinics. **b**, An ultrasound probe can detect the maximum diaphragm displacement during breathing from the anterior subcostal view to assess the inspired volume[64]. But the ultrasound probe needs to be manually tilted to make sure the ultrasound beam goes towards the diaphragm, which is not practical for hand-free long-term monitoring. Moreover, this view only reveals the lung volume during the inspiratory phase, incapable of differentiating the contributions from assistive devices (e.g., a mechanical ventilator) or the subject's diaphragmatic contraction[65]. **c**, An ultrasound probe detects the diaphragm thickness from the intercostal view. The probe can be held vertical to the skin for examination, without manual tilting. This view is suitable for hand-free wearable ultrasound applications.

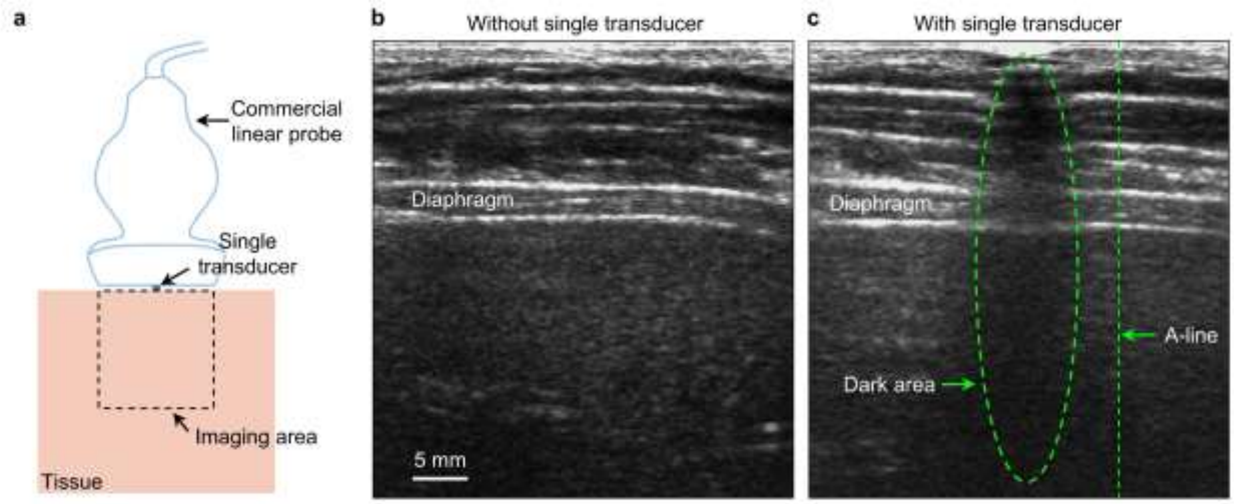

Supplementary Fig. 16 | Simultaneous measurements of the diaphragm with the single-transducer system and a commercial probe. a, Schematics of placing a commercial probe on the single-transducer system to simultaneously measure the diaphragm. **b**, If the single-transducer system is absent between the tissue and the commercial probe, the commercial probe can get a clear B-mode ultrasound image. **c**, If the single-transducer system lies between the tissue and the commercial probe, it blocks a small portion of the commercial ultrasound probe. Therefore, there is a dark area in the B-mode image of the commercial probe, underneath the position of the single transducer. An A-line in the B-mode image, which has a slight horizontal offset (~1 cm) to the single transducer, is extracted to compare it with the measurement of the single transducer. The diaphragm is parallel to skin judging from the B-mode image. Therefore, the ultrasound beam vertical to the diaphragm can detect the diaphragm thickness accurately.

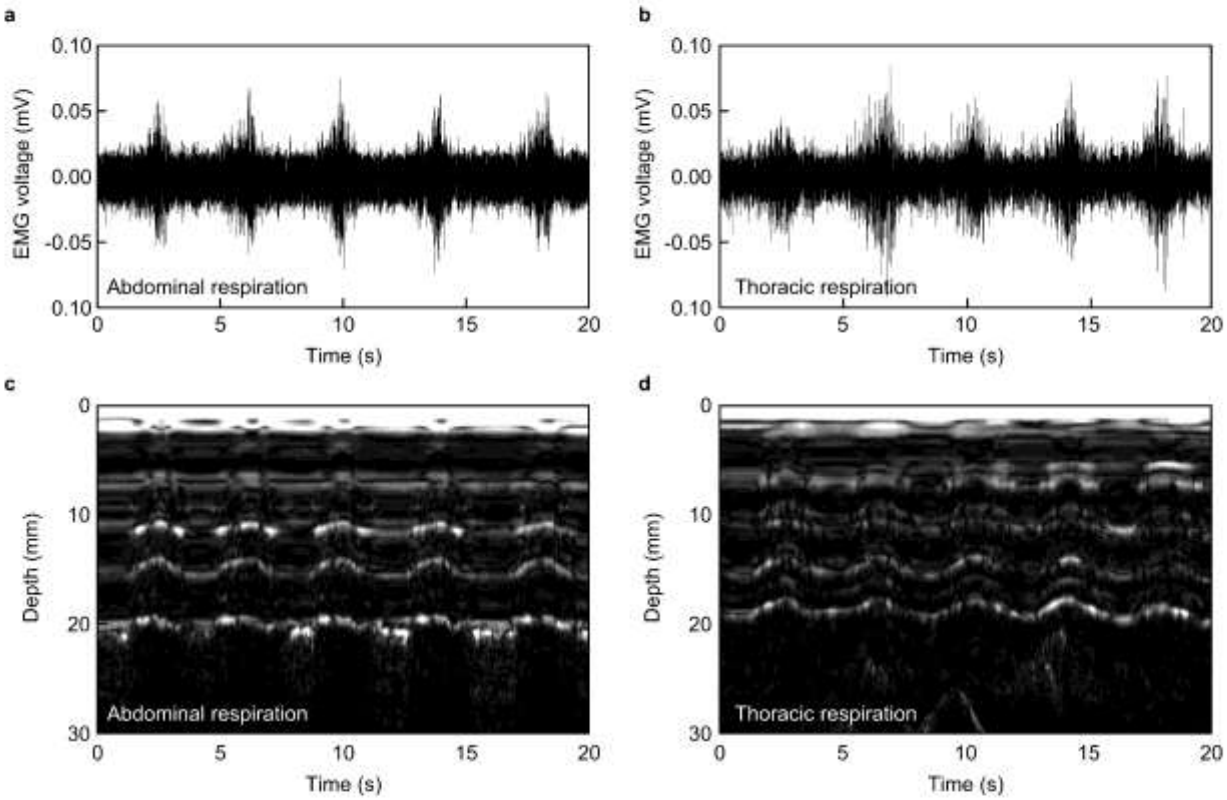

Supplementary Fig. 17 | Comparison between conventional electromyography and our echomyography for diaphragm monitoring. EMG signals during (**a**) abdominal and (**b**) thoracic respirations. Ultrasound signals during (**c**) abdominal and (**d**) thoracic respirations. A volunteering participant did abdominal and thoracic respirations for several tens of seconds. In the meantime, we recorded the EMG and ultrasound signals of the diaphragm using BioRadio and our wearable ultrasound system. The raw EMG signal was filtered by a 60 Hz notch filter and a 100~500 Hz bandpass filter. Such a bandpass filter was used because the surface EMG signals were mainly in this frequency band[66]. Because the surface electrodes capture signals from all muscles, the EMG signals are the mixture of all of them. It is challenging to recognize the diaphragm activity because other muscles could have also contributed to some of the EMG signals. However, the wearable ultrasound system directly measures the movement of diaphragm, which clearly shows the diaphragm motion patterns during different breathing modes.

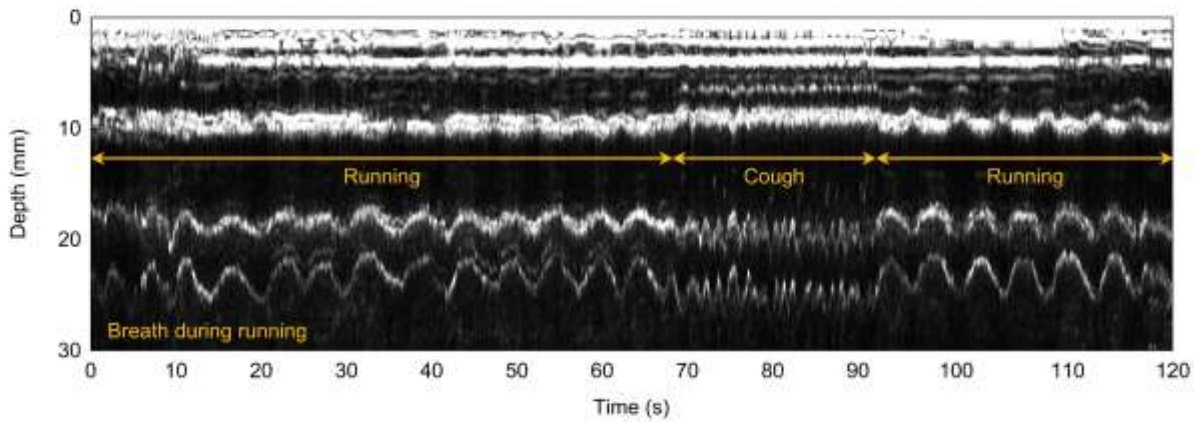

Supplementary Fig. 18 | Testing potential motion artefacts during running on a treadmill. We used the wearable ultrasound system to continuously record the diaphragm signals when a participant ran on a treadmill to test if the exercise could introduce motion artefacts. At the beginning, the participant had stable running and breathing. The ultrasound M-mode image showed that regular running did not cause obvious motion artifacts or affect the monitoring quality of diaphragm. Then the subject consciously coughed to introduce strong diaphragm movements. Although the diaphragm signal showed unstable motions, this was intrinsically because coughing actively caused the relative motions between the ultrasound device and the diaphragm. After coughing, the ultrasound signals became stable again with clearly distinguishable inspiration and expiration patterns. In conclusion, because our wearable ultrasound device could be stably attached to the skin, daily activity and regular excise do not introduce obvious artifacts.

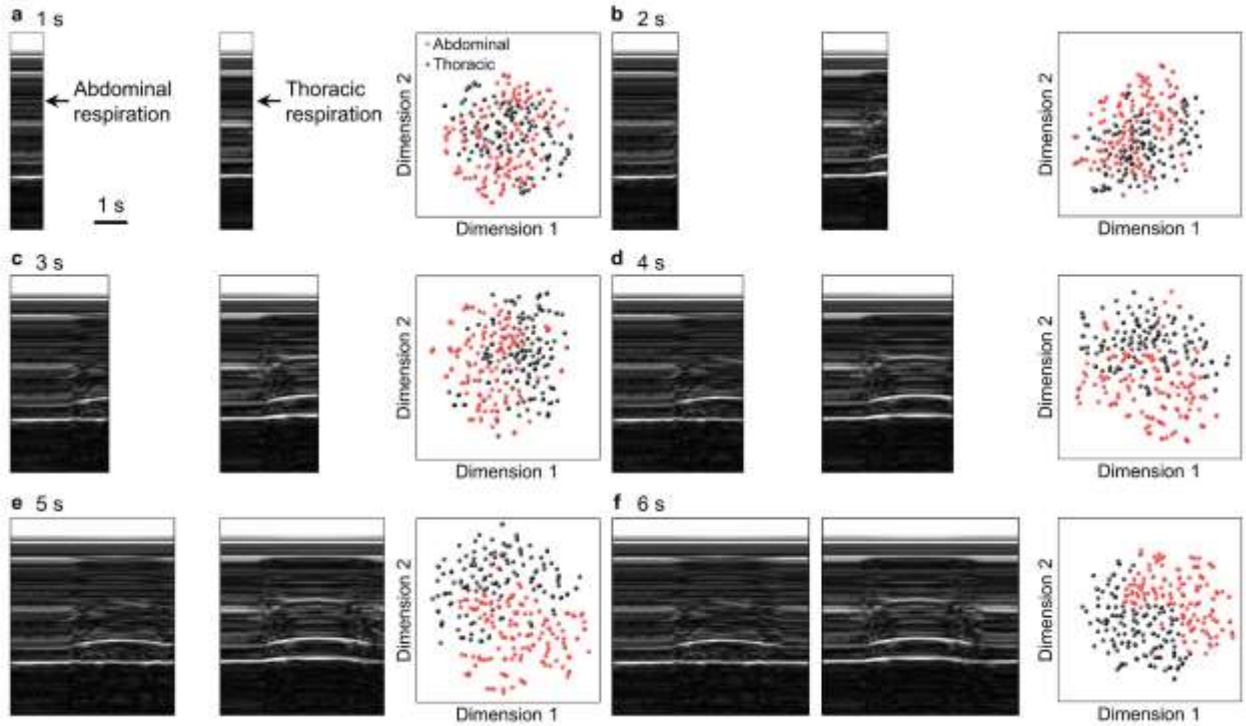

Supplementary Fig. 19 | *t*-SNE plots of M-mode images under different respiration modes. Abdominal respiration contracts the diaphragm and is deep. The belly expands during this type of respiration to make sure diaphragm has the space to contract. Thoracic respiration does not involve the diaphragm and is shallow, during which the intercostal muscles draw a minimal volume of air into the chest. **a-f**, M-mode images corresponding to abdominal respiration and thoracic respiration with different durations. When the duration is short, the two respiration modes may have similar M-mode images. So, they are not clearly separated. As the duration increases, the points corresponding to the two different respiration modes in the *t*-SNE plots are more clearly separated. The larger the separation between these points, the greater the differences in the corresponding data.

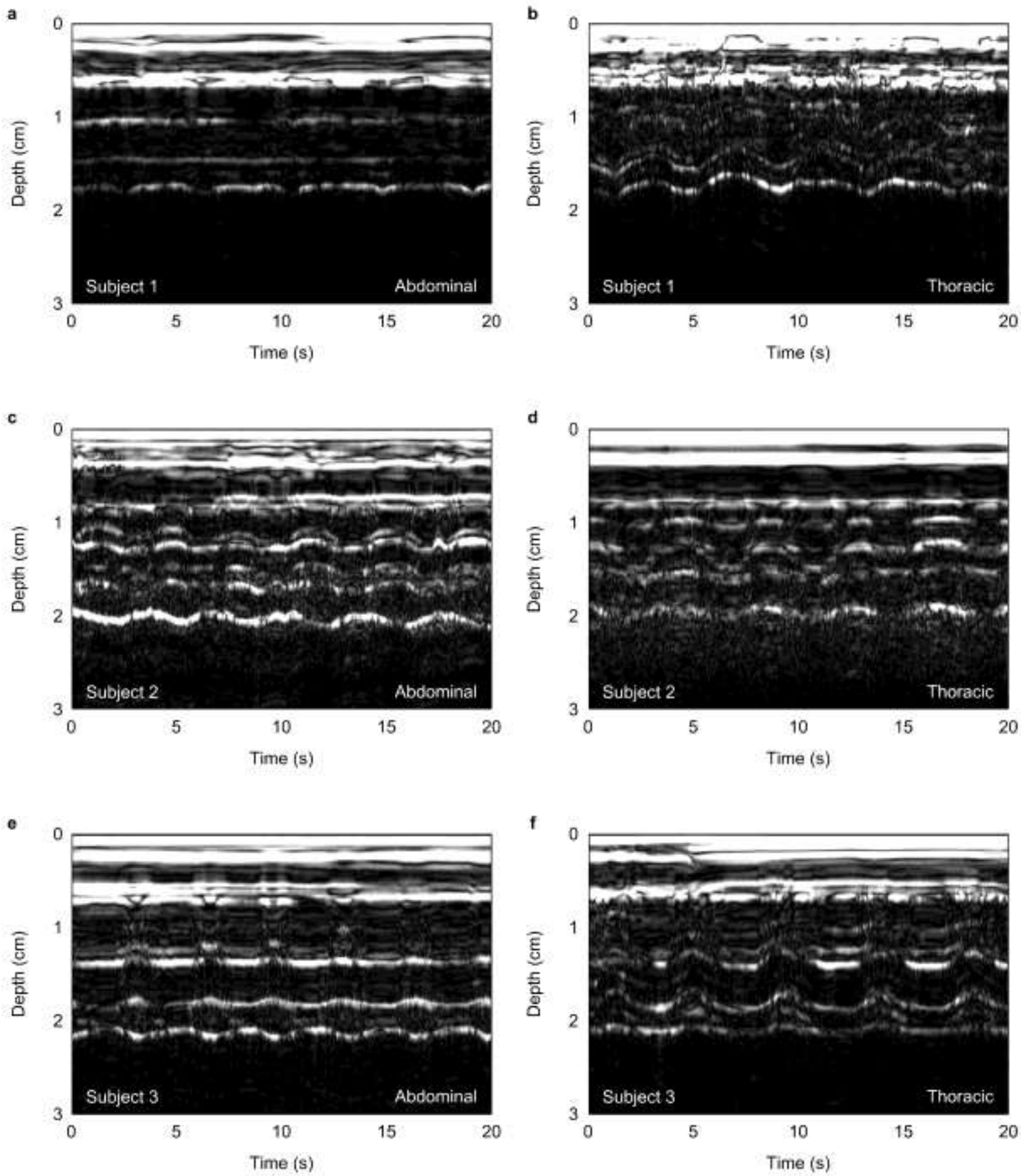

Supplementary Fig. 20 | M-mode images of subjects 1, 2, and 3 during abdominal and thoracic respirations. The diaphragm shows large thickening fractions for all participants in the (**a**), (**c**), and (**e**) abdominal breathing mode, but small thickening degrees in the (**b**), (**d**), and (**f**) thoracic breathing modes.

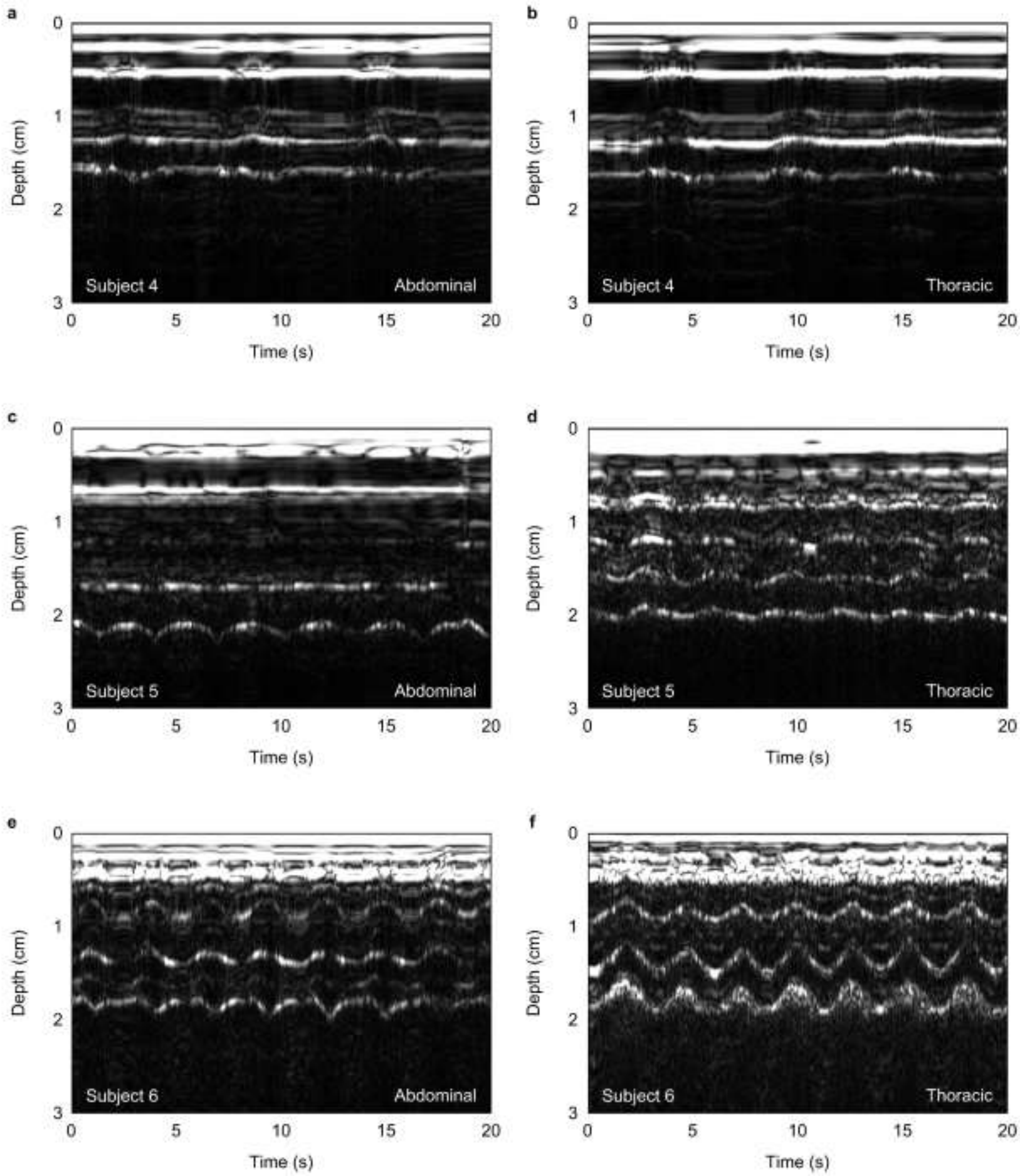

Supplementary Fig. 21 | M-mode images of subjects 4, 5, and 6 during abdominal and thoracic respirations. The diaphragm shows large thickening fractions for all participants in the (**a**), (**c**), and (**e**) abdominal breathing mode, but small thickening degrees in the (**b**), (**d**), and (**f**) thoracic breathing modes.

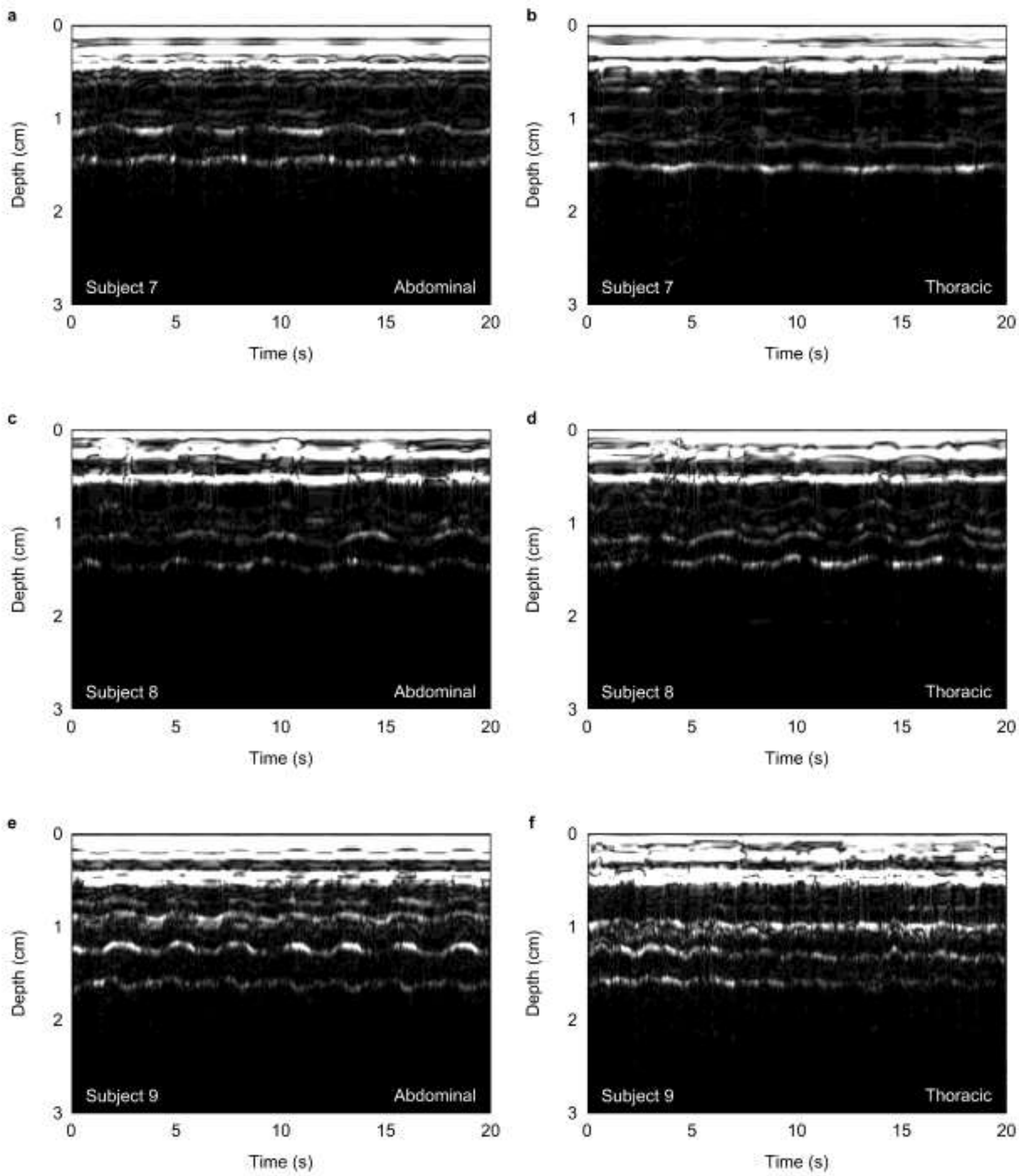

Supplementary Fig. 22 | M-mode images of subjects 7, 8, and 9 during abdominal and thoracic respirations. The diaphragm shows large thickening fractions for all participants in the (**a**), (**c**), and (**e**) abdominal breathing mode, but small thickening degrees in the (**b**), (**d**), and (**f**) thoracic breathing modes.

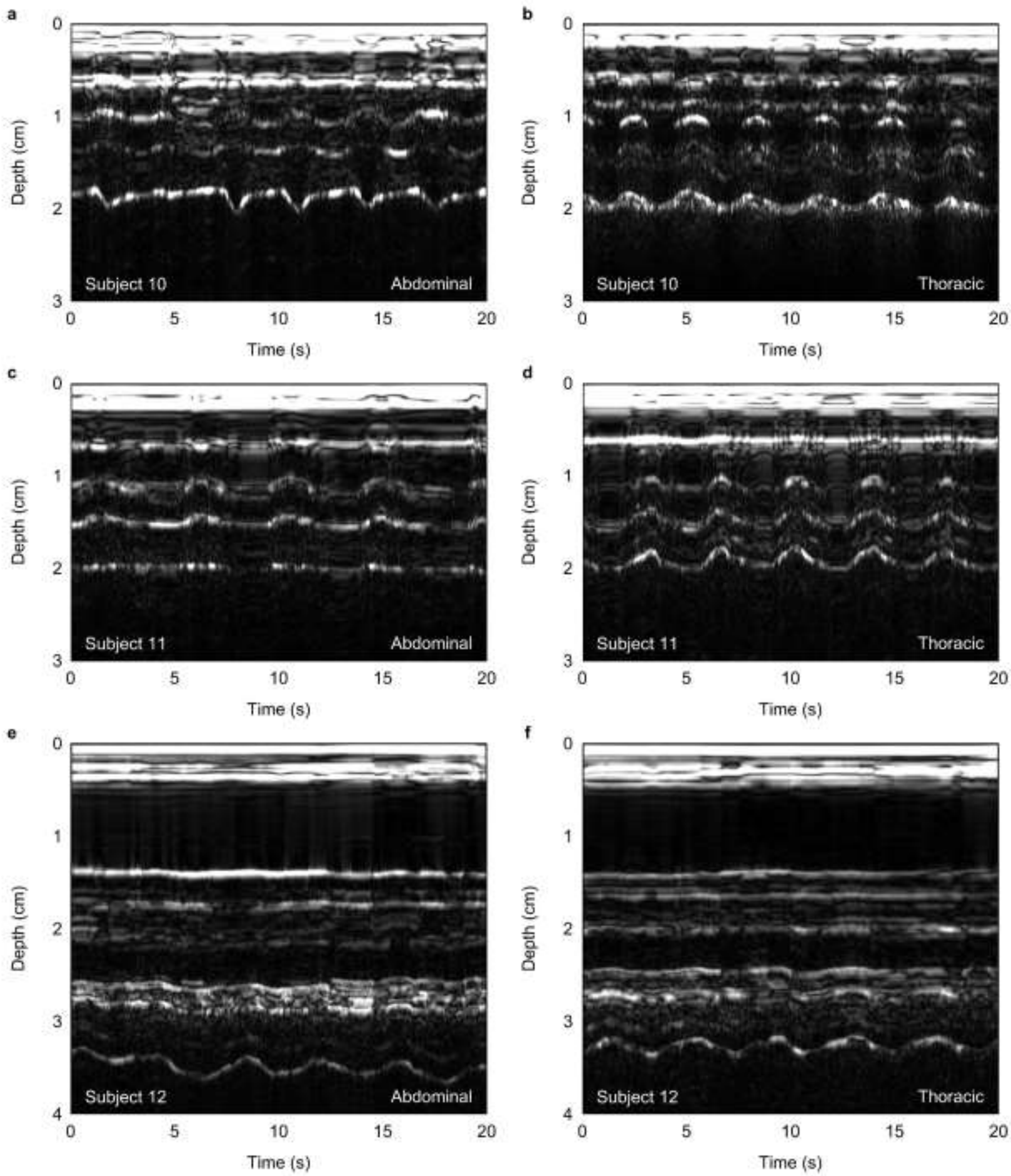

Supplementary Fig. 23 | M-mode images of subjects 10, 11, and 12 during abdominal and thoracic respirations. The diaphragm shows large thickening fractions for all participants in the (**a**), (**c**), and (**e**) abdominal breathing mode, but small thickening degrees in the (**b**), (**d**), and (**f**) thoracic breathing modes.

a

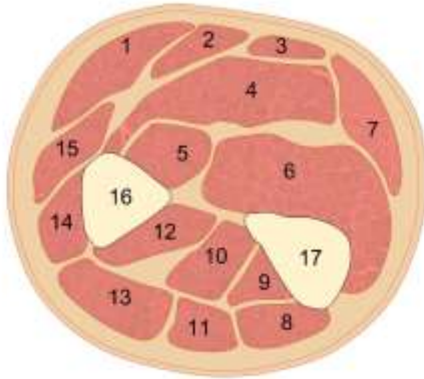

b

Muscle number	Muscle	Related joints
1	Brachioradialis muscle	Elbow
2	Flexor carpi radialis muscle	Wrist
3	Palmaris longus muscle	Wrist
4	Flexor digitorum superficialis muscle	Index, middle, ring, and little fingers
5	Flexor pollicis longus muscle	Thumb
6	Flexor digitorum profundus muscle	Index, middle, ring, and little fingers
7	Flexor carpi ulnaris muscle	Wrist
8	Extensor carpi ulnaris muscle	Wrist
9	Extensor pollicis longus muscle	Thumb
10	Extensor pollicis brevis muscle	Thumb
11	Extensor digiti minimi muscle	Little finger
12	Abductor pollicis longus muscle	Thumb
13	Extensor digitorum muscle	Index, middle, ring and little fingers
14	Extensor carpi radialis brevis muscle	Wrist
15	Extensor carpi radialis longus muscle	Wrist

Supplementary Fig. 24 | Components of the forearm muscles. a, Cross sectional schematics showing the typical spatial distribution of the muscles in the forearm[67]. **b**, Correlations between the muscles and fingers and wrist in typical subjects. 16 and 17 are radius and ulna bones, respectively.

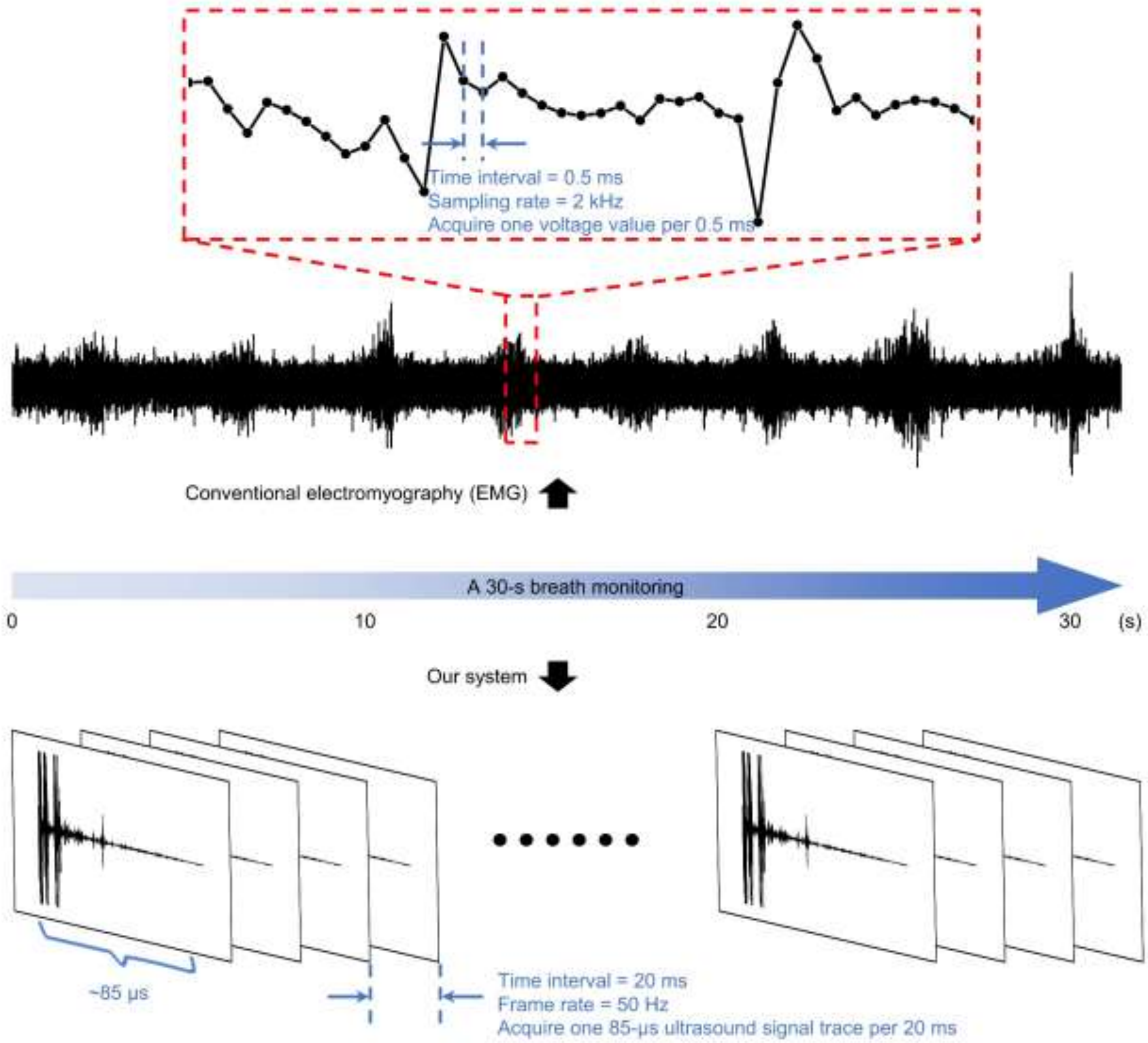

Supplementary Fig. 25 | Comparison of data acquisition and temporal resolution between conventional electromyography and the ultrasound system in this work. We performed 30-s breath monitoring as an example. In conventional electromyography, the surface electrodes measure one voltage value from the skin surface every 0.5 ms. In this case, its temporal resolution is 2 kHz. Our ultrasound system acquires one ultrasound signal trace every 20 ms (corresponding to a temporal resolution of 50 Hz), while each signal trace lasts 85 μs containing 1024 data points. This ultrasound signal trace represents the propagation and reflection of ultrasound waves from the skin to deep tissue (~6.6 cm in depth), which contains the spatial information of deep tissue. To summarize, our ultrasound system has a lower temporal resolution (i.e., 50 Hz) lower than the conventional electromyography (2 kHz), but it contains much more spatial information of muscles for every data acquisition. The applications scenarios of the EMG system and our ultrasound system could be based on their different advantages. The EMG system could be constructed by simple circuits, and capture the mixed signals from a large volume of muscles with several electrodes. Therefore, the EMG system is very suitable for activity or abnormality monitoring of a large area. As a comparison, our ultrasound system can image the detailed movements of deep muscles with a submillimeter resolution, which allows it to accurately monitor detailed muscle motion activities. The temporal resolution limit of our ultrasound system is intrinsically decided by the propagation time of ultrasound waves. Because the transceiving process requires the ultrasound wave to complete the round-trip propagation in the tissue, the minimum time consumption for each frame of data acquisition, which determines the temporal resolution limit of our system, can be calculated as $2D/c$, where D is the detection depth, and c is the speed of sound in tissues. Assuming the sensing depth is about 6.6 cm, as demonstrated in this work, the signal acquisition time will be ~85 μs because the sound speed is ~1540 m/s in muscle. Then, 85 μs will be the temporal resolution limit, which corresponds to the frame rate limit of ~11.7 kHz of our wearable ultrasound system.

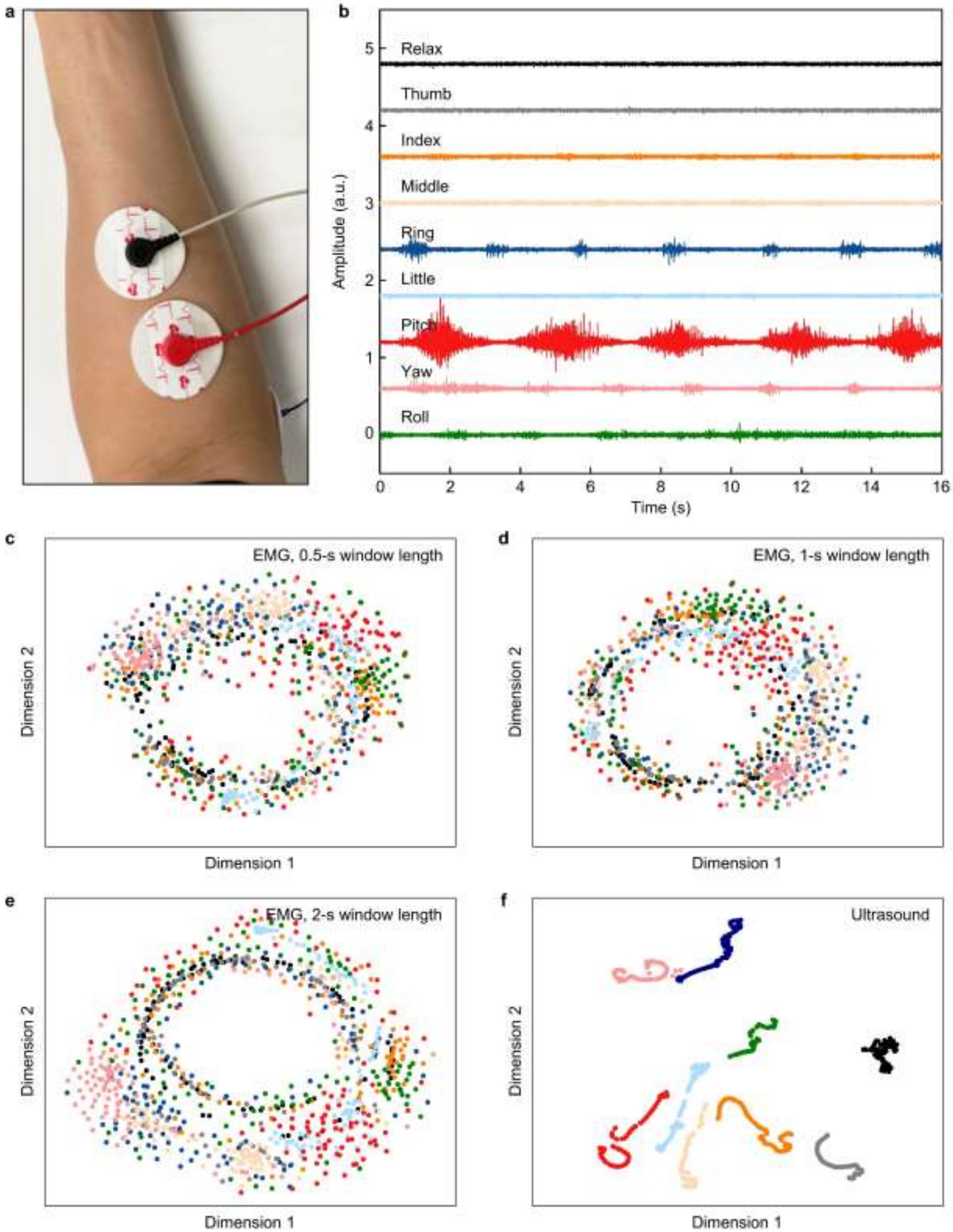

Supplementary Fig. 26 | Surface EMG is insensitive to normal finger and wrist motions. a, Image of electrode placement for surface EMG measurements in this work. **b**, Single-channel surface EMG signals during relaxation, gently bending five fingers, and rotating wrist along pitch, yaw, and roll axes. Raw surface EMG signals were filtered by a 60 Hz notch filter and a 20~500 Hz bandpass filter because surface EMG signals are mainly in this frequency band [66]. The single-channel surface EMG signals during finger bending have low signal to noise ratio and low sensitivity to finger motion. Signals of wrist pitching are relatively strong. But the other two motions of the wrist, yawing and rolling, have low signal amplitudes. **c-e**, *t*-SNE plots of single-channel surface EMG signals corresponding to different segmentation lengths. The scatter points share the same color codes as the signals in **b**. We randomly selected 100 segments from a continuous 1 min surface EMG signal for each kind of motion. The fingers/wrist repeatedly did the bending/rotation every ~2 s within the 1 min measurement. The duration of each segment was set as 0.5 s, 1 s, or 2 s. Such segment window lengths are typical for surface EMG applications[66]. **f**, *t*-SNE plot of EcMG signals corresponding to hand motions like those in Fig. 4B and fig. S23. These *t*-SNE plots show that points of different motions are mixed for surface EMG signals, which means the surface EMG signals of different hand motions have small differences. It is challenging for single-channel surface EMG signals to accurately distinguish different hand gestures. However, the points of different motions are perfectly separated for single-channel EcMG signals, which means ultrasound signals have high differentiation accuracies for different hand gestures. Therefore, EcMG signals are more sensitive to normal muscle contraction than surface EMG signals.

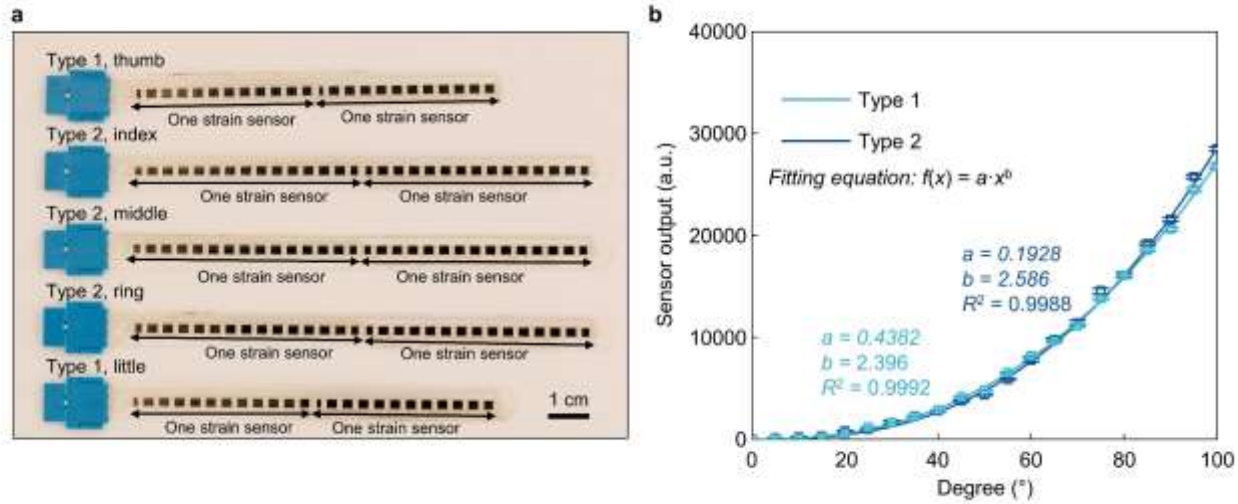

Supplementary Fig. 27 | Calibration of strain sensors. a, Image of the strain sensors used for measuring finger joint angles. Each sensor contains two sub strain sensors for two joints measurement. Two sensors of type 1 are used to measure the two joints of the thumb and the little fingers. Three sensors of type 2 are used to measure two joints of the index, middle, and ring fingers. **b**, Calibration curves of the two types of sensors show the relationships between the bending angle and sensor output. The sub sensors of the same type are exactly the same.

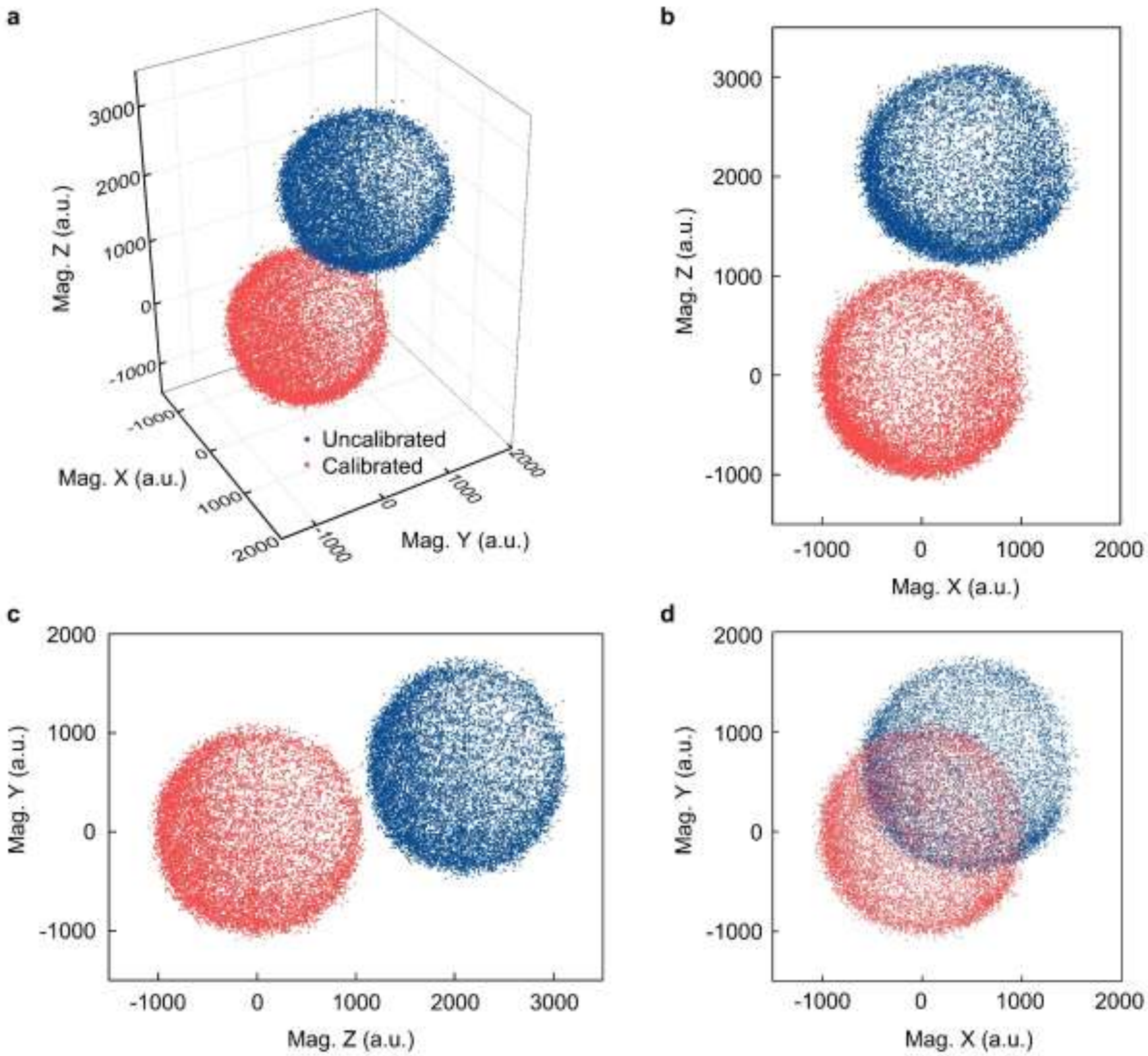

Supplementary Fig. 28 | Calibration of the magnetometer outputs. a, The blue dots are the raw magnetometer output without compensating for environmental distortion. The center of the dot cloud is shifted away from the origin of the coordinate system. The red dots are the calibrated magnetometer data. The center of the red dot cloud is at the origin of the coordinate system. **b-d**, The projection of raw and calibrated data in X-Z, Y-Z, and X-Y planes, respectively.

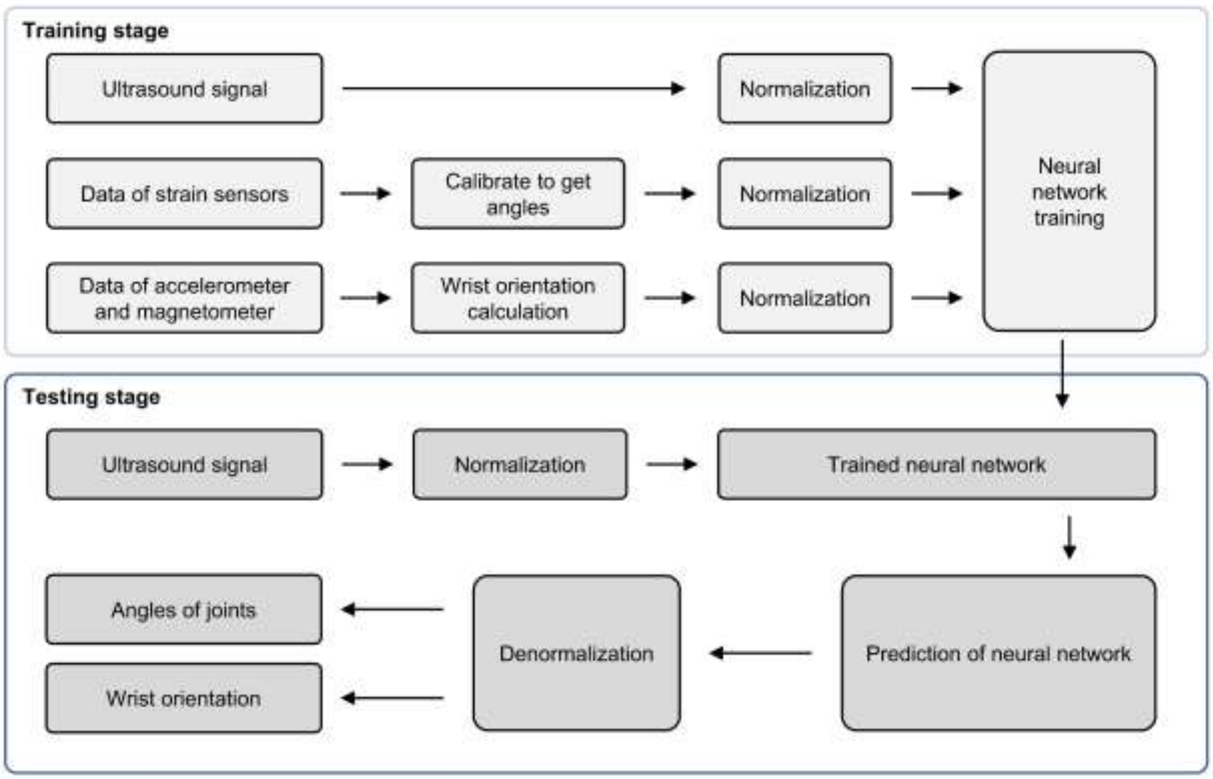

Supplementary Fig. 29 | Flowchart of training and testing of deep learning-based continuous hand gesture tracking. At the training stage, we need to collect the training dataset, which contains paired ultrasound signals and the hand gesture data. The hand gesture data is composed of bending angles of the fingers' joints and rotation angles of the wrist, which are measured by strain sensors and a six-axis IMU sensor (three-axis accelerometer, three-axis magnetometer), respectively. Calibration is required to transform the strain sensor output to bending angle. The ultrasound signals, bending angles of the finger joints, and rotation angles of the wrist are all normalized before being fed into the neural network for training. After the neural network is trained, it can be applied for real-time hand gesture tracking. At the testing stage, the ultrasound signal is also normalized before fed into the trained neural network. The outputs of the neural network are denormalized to acquire the finger joint bending and wrist rotation angles.

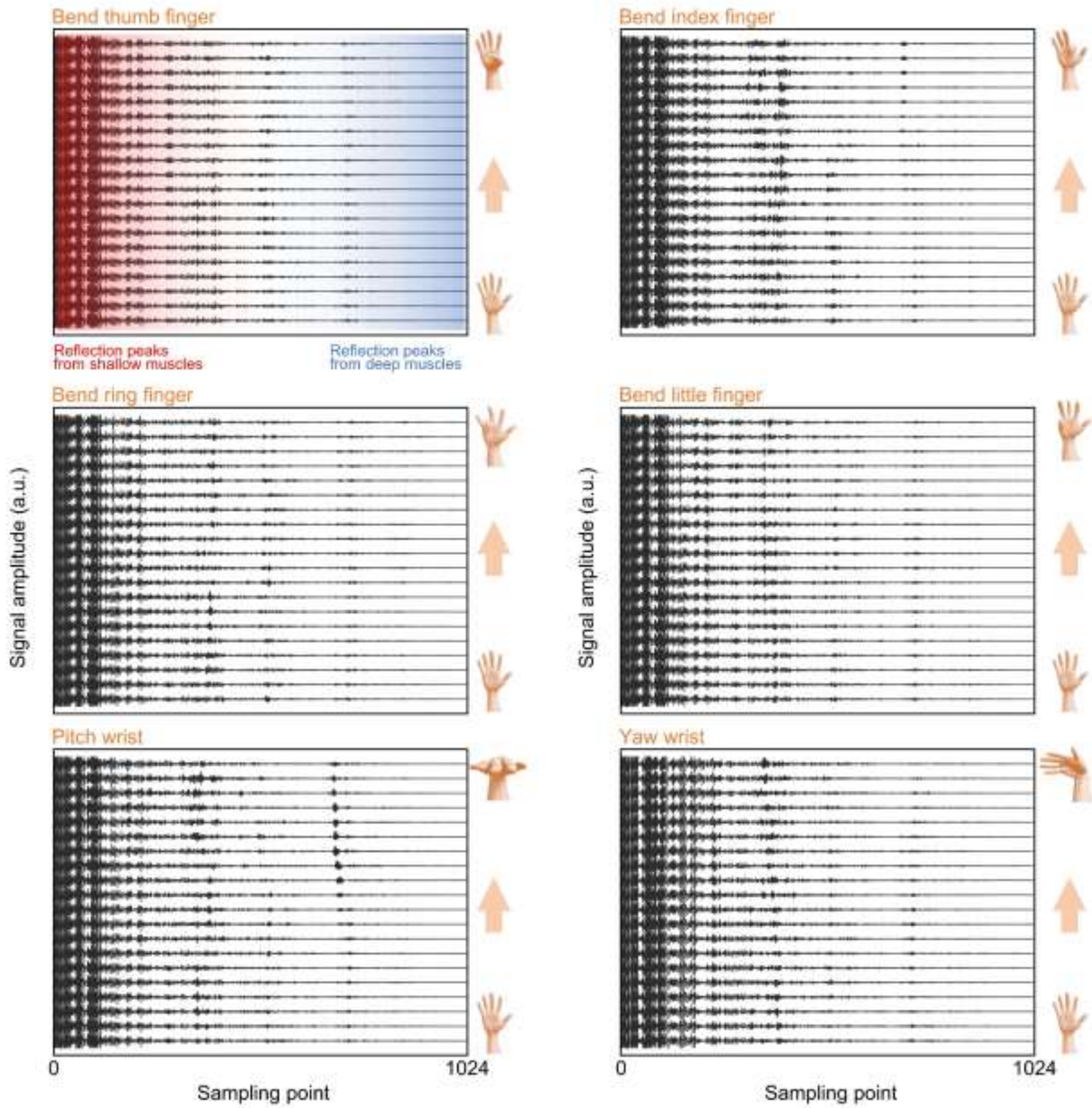

Supplementary Fig. 30 | RF signals as the fingers bend and the wrist rotates. Each panel shows 20 RF signals overlapped to illustrate the evolvement of echo peaks as the fingers and wrist move. The single transducer for hand gesture tracking has a wide beam. One RF data contains signals from all muscles in such a wide beam. Different muscles at the same radial depth appear at the same time in the RF signal. The peak shifts only reflect motion of muscles in the radial direction. Therefore, it is not possible to quantify the absolute motion of a specific muscle just based on the shifted peak.

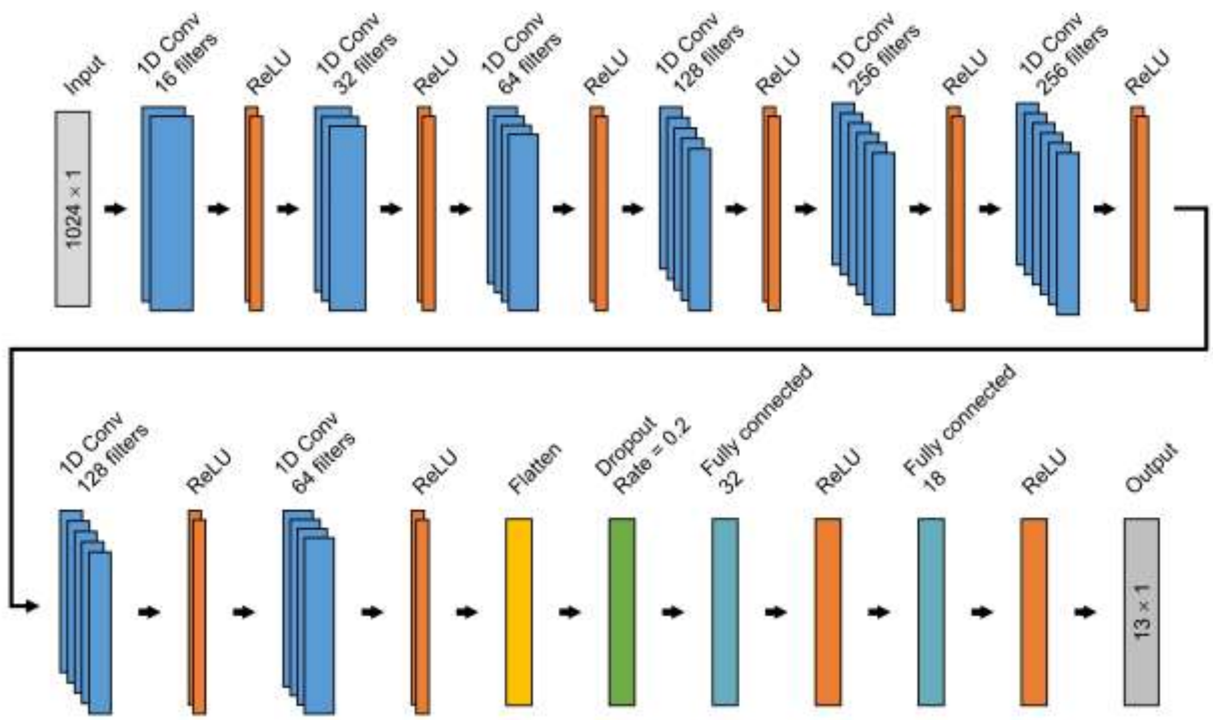

Supplementary Fig. 31 | Framework of the deep neural network for hand gesture tracking. Although the muscle distribution decides the hand gesture and the RF signals, it is almost impossible to establish a mathematical relationship between the RF signals and the hand gesture. Therefore, we developed a deep neural network to infer the hand gesture from the RF signals. The input data are normalized RF signals, while the output layer has 13 numbers corresponding to 13 degrees of freedom of the hand gesture. Convolutional layers are well-suited to detect local patterns and structures in the data. In this work, the RF signal is 1D waveform. We first stack several 1D convolutional layers at the beginning and then adopt fully connected layers at the end of the network, which are typically used as the final layer for classification.

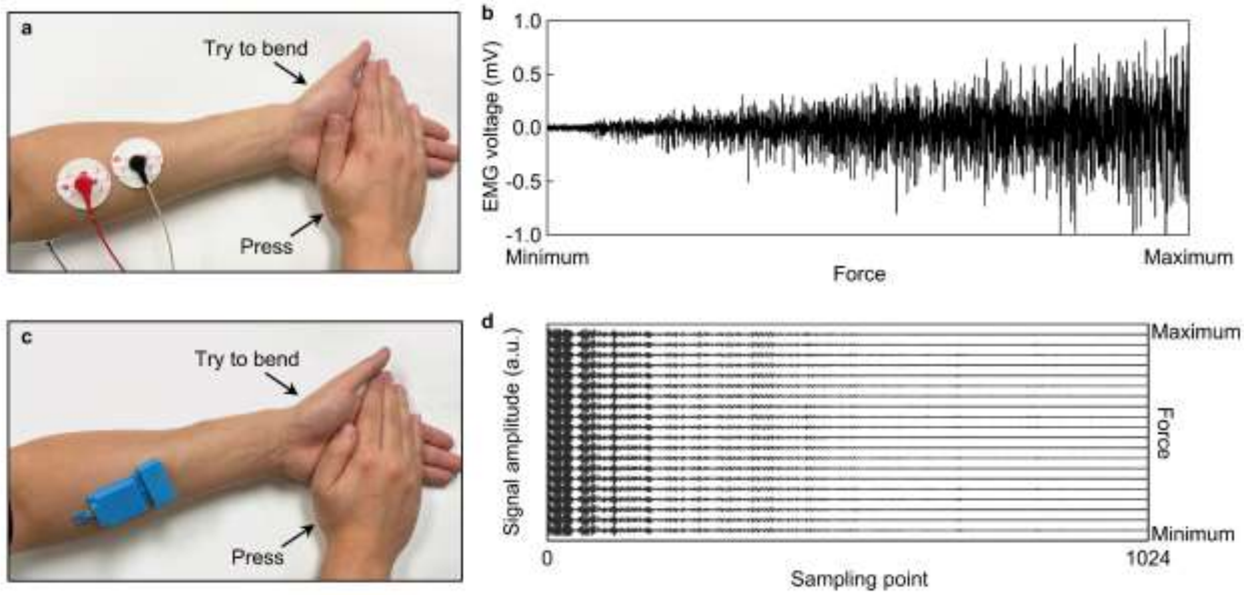

Supplementary Fig. 32 | Comparison between EMG and EcMG when the hand was constrained. a, Image of EMG measurement. **b**, EMG measures the biopotential in the muscle fibers. Therefore, even though the hand cannot move, the muscle fibers are still generating biopotentials, which can be captured by EMG electrodes. **c**, Image of EcMG measurement. **d**, Hand gesture is directly related to the spatial distribution of muscle fibers, which decides the ultrasound RF signals. Therefore, if the hand is constrained without moving, the RF signals show minimal changes even if the muscle force increases. In summary, EcMG directly measures the hand gesture by capturing the spatial distribution of muscle fibers[68], while EMG directly measures the force generated by muscle fibers[69].

Number of piezoelectric elements	Fully integrated wireless	Applications	Deep learning powered	Reference
256	No	Deep tissue elastography	No	[70]
144	No	Deep tissue hemodynamics	No	[31]
88	No	Heart imaging	Yes	[70]
32	Yes	Blood pressure monitoring	Yes	[71]
20	No	Blood pressure monitoring	No	[30]
1	Yes	Diaphragm monitoring and human-machine interface	Yes	**This work**

Supplementary Table 1 | Comparison between the device in this study and our previously reported works. The uniqueness of this device can be summarized in terms of transducer array design, system integration level, applications, and deep learning algorithm.

Component	Manufacture product number	Voltage range (V)	Regulator (if used)
Operational amplifier	ADA4895-1ARJZ-R7	3 ~ 10	N/A
Operational amplifier	ADA4897-1ARJZ-RL	3 ~ 10	N/A
Microcontroller	ATMEGA328P-ANR	2.7 ~ 5.5	MIC5205-3.3YM5-TR
ADC	PIC32MZ1024EFH064-I/MR	2.1 ~ 3.6	MIC5205-3.3YM5-TR
Wi-Fi module	ESP32-S3-WROOM-1	3.0 ~ 3.6	AMS1117

Supplementary Table 2 | Specifics of key components in the PCB. The power consumption of these chips is manageable by a commercial lithium-polymer battery.

Device/skin interface	Sensing area	Detection mode	Health monitoring	Human-machine interface	Deep learning powered	Reference
Rigid	Deep tissue	Continuous doppler	Carotid artery blood flow	No	No	[39]
Rigid	Deep tissue	A-mode	Bladder volume	No	No	[40]
Rigid	Deep tissue	A-mode	Bladder volume	No	No	[41]
Soft	Skin surface	A-mode	Lung volume	No	No	[42]
Soft	Deep tissue	A-mode	Diaphragm movement	Yes	Yes	**This work**

Supplementary Table 3 | Comparison with other fully integrated wearable ultrasound devices. The device in this work has soft interface with the skin, ensuring stable adhesion and acoustic coupling between the single transducer and the skin. Additionally, the device in this work is powered by a deep learning algorithm, which enables continuous tracking of hand gestures for human-machine interface.

Transducer type	Transducer size	Channel number	Sensing mode	Wearable circuit	Use cases	Reference
Rigid linear probe	~38 mm in width	128	B-mode image	No	Classify 15 discrete hand gestures	[72]
Rigid linear probe	~38 mm in width	N/A	B-mode image	No	Classify 6 discrete hand gestures	[73]
Rigid phase array	>19.2 mm in width	1	Radiofrequency signal	No	Classify 9 discrete hand gestures	[74]
Soft single transducers	20 mm × 20 mm × 0.28 mm	3	Radiofrequency signal	No	Classify 5 discrete hand gestures	[75]
Rigid single transducers	Ø 9 mm × 11 mm	8	Radiofrequency signal	No	Classify 8 discrete hand gestures; Track continuous wrist rotation	[76]
Rigid single transducers	16 mm in diameter	8	Radiofrequency signal	No	Classify 11 discrete hand gestures or 9 discrete facial gestures; Track continuous thumb angle or the angle of all other four fingers	[77]
Soft transducer array	15 mm × 15 mm × 3 mm; 100 mm × 100 mm × 3 mm	16	Radiofrequency signal	No	Track continuous arm rotation angle	[78]
Soft single transducer	6 mm × 6 mm × 1.2 mm	1	Radiofrequency signal	Yes	Track 13 continuous angles of the hand joints	**This work**

Supplementary Table 4 | Comparison among different EcMG studies for hand gesture recognition. We developed a fully wearable device, including a soft transducer and a compact controlling circuit, eliminating the tethering wires to bulky equipment. Soft transducers enable reliable contact with the skin, ensuring stable acoustic coupling.

Method	Data	Discrete/ Continuous	Kinds of motions	Accuracy of classification	Number of angles	Error of angles	Citation
EMG	4-ch EMG signal	Discrete	3	95.4%	-	-	[79]
	4-ch EMG signal	Discrete	6	91.1%	-	-	[80]
	5-ch EMG signal	Discrete	10	92.75%	-	-	[81]
	6-ch EMG signal	Discrete	15	98%	-	-	[82]
	8-ch EMG signal	Discrete	6	95.3%	-	-	[83]
	8-ch EMG signal	Discrete	6	90.85%	-	-	[84]
	48-ch EMG signal	Discrete	9	95.8%	-	-	[85]
	57-ch EMG signal	Discrete	7	~98%	-	-	[86]
	192-ch EMG signal	Discrete	11	96.5%	-	-	[87]
	8-ch EMG signal	Discrete/ Continuous	7	95.64%	2	Linear regression $R^2 = 0.843$	[88]
	8-ch EMG signal	Discrete/ Continuous	-	-	21	Median error of 6.4°, 90%-ile error 18.3°	[52]
	96-ch EMG signal	Discrete/ Continuous	-	-	5	>10°	[89]
EcMG	3-ch RF signal	Discrete	5	92.5 ± 7.6%	-	-	[75]
	8-ch RF signal	Discrete/ Continuous	8	96.5 ± 1.7%	1	linear regression $R^2 = 0.954 \pm 0.012$	[76]
	8-ch RF signal	Discrete/ Continuous	11	93.4%	2	1.7° for thumb and 6.5° for other four fingers	[77]
	B-mode image	Discrete	6	94%	-	-	[73]
	B-mode image	Discrete	15	91%	-	-	[72]
	16-ch RF signal	Discrete	1	-	-	-	[78]
	1-ch RF signal	Discrete	9	67.01%	-	-	[74]
	1-ch RF signal	**Continuous**	**-**	**-**	**13**	**7.9°**	**This work**

Supplementary Table 5 | Accuracies of hand gesture recognition based on EMG and EcMG. Previous studies only achieved classifying specific discrete hand gestures, or tracking a few hand joints using multiple-channel signals. In this work, we demonstrated continuous tracking of angles of 13 hand joints using one-channel signal. We used strain and IMU sensors to acquire the finger bending angles and the wrist rotation angles as the ground truth of hand gesture. Then, we developed a deep neural network to relate the RF signals to the angles of the fingers and wrist.

Supplementary Video 1: Simultaneous measurements of EcMG and EMG signals as fingers bend and wrist rotates.

Supplementary Video 2: Real-time virtual bird control by correlating the pitch angle of wrist with the height of the virtual bird.

Supplementary Video 3: Real-time robotic arm control by correlating the pitch angle of wrist and finger joint angle with motions of robotic arm.

References

1 Chung, H. U. *et al.* Skin-interfaced biosensors for advanced wireless physiological monitoring in neonatal and pediatric intensive-care units. *Nature Medicine* **26**, 418-429 (2020).

2 Jeong, H. *et al.* Differential cardiopulmonary monitoring system for artifact-canceled physiological tracking of athletes, workers, and COVID-19 patients. *Science Advances* **7**, eabg3092 (2021).

3 Tan, C. *et al.* A high performance wearable strain sensor with advanced thermal management for motion monitoring. *Nature Communications* **11**, 1-10 (2020).

4 Kwak, J. W. *et al.* Wireless sensors for continuous, multimodal measurements at the skin interface with lower limb prostheses. *Science Translational Medicine* **12**, eabc4327 (2020).

5 Schwartz, G. *et al.* Flexible polymer transistors with high pressure sensitivity for application in electronic skin and health monitoring. *Nature Communications* **4**, 1-8 (2013).

6 Yu, Y. *et al.* Biofuel-powered soft electronic skin with multiplexed and wireless sensing for human-machine interfaces. *Science Robotics* **5**, eaaz7946 (2020).

7 Baker, L. B. *et al.* Skin-interfaced microfluidic system with personalized sweating rate and sweat chloride analytics for sports science applications. *Science Advances* **6**, eabe3929 (2020).

8 Moin, A. *et al.* A wearable biosensing system with in-sensor adaptive machine learning for hand gesture recognition. *Nature Electronics* **4**, 54-63 (2021).

9 Taccola, G. *et al.* Using EMG to deliver lumbar dynamic electrical stimulation to facilitate cortico-spinal excitability. *Brain Stimulation* **13**, 20-34 (2020).

10 Bellani, G. *et al.* Measurement of diaphragmatic electrical activity by surface electromyography in intubated subjects and its relationship with inspiratory effort. *Respiratory care* **63**, 1341-1349 (2018).

11 Kim, M. K. *et al.* Flexible submental sensor patch with remote monitoring controls for management of oropharyngeal swallowing disorders. *Science Advances* **5**, eaay3210 (2019).

12 Kim, T. *et al.* Ultrathin crystalline-silicon-based strain gauges with deep learning algorithms for silent speech interfaces. *Nature Communications* **13**, 5815 (2022).

13 Eskes, M. *et al.* Simulation of facial expressions using person-specific sEMG signals controlling a biomechanical face model. *International Journal of Computer Assisted Radiology and Surgery* **13**, 47-59 (2018).

14 Lee, K. *et al.* Mechano-acoustic sensing of physiological processes and body motions via a soft wireless device placed at the suprasternal notch. *Nature Biomedical Engineering* **4**, 148-158 (2020).

15 Chun, K. S. *et al.* A skin-conformable wireless sensor to objectively quantify symptoms of pruritus. *Science Advances* **7**, eabf9405 (2021).

16 Baek, S. *et al.* Spatiotemporal measurement of arterial pulse waves enabled by wearable active-matrix pressure sensor arrays. *ACS Nano* **16**, 368-377 (2021).

17 Wang, Y. *et al.* A durable nanomesh on-skin strain gauge for natural skin motion monitoring with minimum mechanical constraints. *Science Advances* **6**, eabb7043 (2020).

18 Araromi, O. A. *et al.* Ultra-sensitive and resilient compliant strain gauges for soft machines. *Nature* **587**, 219-224 (2020).

19 Ryu, D. *et al.* Comprehensive pregnancy monitoring with a network of wireless, soft, and flexible sensors in high-and low-resource health settings. *Proceedings of the National Academy of Sciences* **118**, e2100466118 (2021).

20 Rwei, A. Y. *et al.* A wireless, skin-interfaced biosensor for cerebral hemodynamic monitoring in pediatric care. *Proceedings of the National Academy of Sciences* **117**, 31674-31684 (2020).

21 Fortin, J. *et al.* A novel art of continuous noninvasive blood pressure measurement. *Nature Communications* **12**, 1387 (2021).

22 Gao, X. *et al.* A photoacoustic patch for three-dimensional imaging of hemoglobin and core temperature. *Nature Communications* **13**, 7757 (2022).

23 Koh, A. *et al.* A soft, wearable microfluidic device for the capture, storage, and colorimetric sensing of sweat. *Science Translational Medicine* **8**, 366ra165-366ra165 (2016).

24 Thennadil, S. N. *et al.* Comparison of glucose concentration in interstitial fluid, and capillary and venous blood during rapid changes in blood glucose levels. *Diabetes Technology & Therapeutics* **3**, 357-365 (2001).

25 Claver, J. B., Mirón, M. V. & Capitán-Vallvey, L. Disposable electrochemiluminescent biosensor for lactate determination in saliva. *Analyst* **134**, 1423-1432 (2009).

26 Baca, J. T., Finegold, D. N. & Asher, S. A. Tear glucose analysis for the noninvasive detection and monitoring of diabetes mellitus. *The Ocular Surface* **5**, 280-293 (2007).

27 Kim, J., Campbell, A. S., de Ávila, B. E.-F. & Wang, J. Wearable biosensors for healthcare monitoring. *Nature Biotechnology* **37**, 389-406 (2019).

28 Isaacson, D., Mueller, J., Newell, J. & Siltanen, S. Imaging cardiac activity by the D-bar method for electrical impedance tomography. *Physiological Measurement* **27**, S43 (2006).

29 Victorino, J. A. *et al.* Imbalances in regional lung ventilation: a validation study on electrical impedance tomography. *American Journal of Respiratory and Critical Care Medicine* **169**, 791-800 (2004).

30 Wang, C. *et al.* Monitoring of the central blood pressure waveform via a conformal ultrasonic device. *Nature Biomedical Engineering* **2**, 687-695 (2018).

31 Wang, C. *et al.* Continuous monitoring of deep-tissue haemodynamics with stretchable ultrasonic phased arrays. *Nature Biomedical Engineering* **5**, 749-758 (2021).

32 Wang, F. *et al.* Flexible Doppler ultrasound device for the monitoring of blood flow velocity. *Science Advances* **7**, eabi9283 (2021).

33 Hu, H. *et al.* A wearable cardiac ultrasound imager. *Nature* **613**, 667-675 (2023).

34 Hu, H. *et al.* Stretchable ultrasonic arrays for the three-dimensional mapping of the modulus of deep tissue. *Nature Biomedical Engineering* **7**, *1321–1334 (2023).*.

35 Staudenmann, D., Roeleveld, K., Stegeman, D. F. & Van Dieën, J. H. Methodological aspects of SEMG recordings for force estimation–a tutorial and review. *Journal of Electromyography and Kinesiology* **20**, 375-387 (2010).

36 Jamal, M. Z. Signal acquisition using surface EMG and circuit design considerations for robotic prosthesis. *Computational Intelligence in Electromyography Analysis-A Perspective on Current Applications and Future Challenges* **18**, 427-448 (2012).

37 Rampichini, S., Vieira, T. M., Castiglioni, P. & Merati, G. Complexity analysis of surface electromyography for assessing the myoelectric manifestation of muscle fatigue: A review. *Entropy* **22**, 529 (2020).

38 Winder, S. *Analog and digital filter design*. (Elsevier, 2002).

39 Kenny, J.-É. S. Functional hemodynamic monitoring with a wireless ultrasound patch. *Journal of Cardiothoracic and Vascular Anesthesia* **35**, 1509-1515 (2021).

40 Hofstetter, S. *et al.* Dfree ultrasonic sensor in supporting quality of life and patient satisfaction with bladder dysfunction. *International Journal of Urological Nursing*.

41 van Leuteren, P. G., Klijn, A. J., de Jong, T. P. & Dik, P. SENS-U: validation of a wearable ultrasonic bladder monitor in children during urodynamic studies. *Journal of Pediatric Urology* **14**, 569. e561-569. e566 (2018).

42 Chen, A. *et al.* Wireless wearable ultrasound sensor on a paper substrate to characterize respiratory behavior. *ACS Sensors* **4**, 944-952 (2019).

43 Huang, Z. *et al.* Three-dimensional integrated stretchable electronics. *Nature Electronics* **1**, 473-480 (2018).

44 Dewitte, K., Fierens, C., Stockl, D. & Thienpont, L. M. Application of the Bland–Altman plot for interpretation of method-comparison studies: a critical investigation of its practice. *Clinical Chemistry* **48**, 799-801 (2002).

45 Yu, J., Qin, M. & Zhou, S. Dynamic gesture recognition based on 2D convolutional neural network and feature fusion. *Scientific Reports* **12**, 1-15 (2022).

46 Tekin, B., Bogo, F. & Pollefeys, M. in *Proceedings of the IEEE/CVF conference on computer vision and pattern recognition.* 4511-4520.

47 Ge, L. *et al.* in *Proceedings of the IEEE/CVF Conference on Computer Vision and Pattern Recognition.* 10833-10842.

48 Malik, J., Elhayek, A. & Stricker, D. in *International Conference on Virtual Reality and Augmented Reality.* 3-17 (Springer).

49 Glauser, O., Wu, S., Panozzo, D., Hilliges, O. & Sorkine-Hornung, O. Interactive hand pose estimation using a stretch-sensing soft glove. *ACM Transactions on Graphics (ToG)* **38**, 1-15 (2019).

50 Shen, Z. *et al.* A soft stretchable bending sensor and data glove applications. *Robotics and Biomimetics* **3**, 1-8 (2016).

51 Mummadi, C. K. *et al.* in *Informatics.* 28 (MDPI).

52 Liu, Y., Zhang, S. & Gowda, M. in *Proceedings of the Web Conference 2021.* 1471-1482.

53 Hong, Y., Sui, L., Zhang, M. & Shi, G. Theoretical analysis and experimental study of the effect of the neutral plane of a composite piezoelectric cantilever. *Energy conversion and management* **171**, 1020-1029 (2018).

54 McIntosh, J., Marzo, A., Fraser, M. & Phillips, C. in *Proceedings of the 2017 CHI Conference on Human Factors in Computing Systems.* 1923-1934.

55 Xia, W., Zhou, Y., Yang, X., He, K. & Liu, H. Toward portable hybrid surface electromyography/a-mode ultrasound sensing for human–machine interface. *IEEE Sensors Journal* **19**, 5219-5228 (2019).

56 Zhou, Z. *et al.* Sign-to-speech translation using machine-learning-assisted stretchable sensor arrays. *Nature Electronics* **3**, 571-578 (2020).

57 Wang, M. *et al.* Gesture recognition using a bioinspired learning architecture that integrates visual data with somatosensory data from stretchable sensors. *Nature Electronics* **3**, 563-570 (2020).

58 Tang, L., Shang, J. & Jiang, X. Multilayered electronic transfer tattoo that can enable the crease amplification effect. *Science Advances* **7**, eabe3778 (2021).

59 Wu, Y., Zheng, B. & Zhao, Y. in *2018 Chinese Automation Congress (CAC).* 2446-2450 (IEEE).

60 Ozyagcilar, T. Implementing a tilt-compensated eCompass using accelerometer and magnetometer sensors. *Freescale semiconductor, AN* **4248** (2012).

61 David Pirogovsky, A. N., Alec Newport. *Constellation Glasses*, https://people.ece.cornell.edu/land/courses/ece4760/FinalProjects/f2018/dap263_acn55_pdd35/dap263_acn55_pdd35/index.html

62 Gabriel, D. A. Teaching Essential EMG Theory to Kinesiologists and Physical Therapists Using Analogies Visual Descriptions, and Qualitative Analysis of Biophysical Concepts. *Sensors* **22**, 6555 (2022).

63 Konrad, P. The abc of emg. *A practical introduction to kinesiological electromyography* **1**, 30-35 (2005).

64 Cohen, E. *et al.* Excursion-volume relation of the right hemidiaphragm measured by ultrasonography and respiratory airflow measurements. *Thorax* **49**, 885-889 (1994).

65 Guarracino, F. *et al.* Lung, heart, vascular, and diaphragm ultrasound examination of COVID-19 patients: a comprehensive approach. *Journal of Cardiothoracic and Vascular Anesthesia* **35**, 1866-1874 (2021).

66 Nazmi, N. *et al.* Assessment on stationarity of EMG signals with different windows size during isotonic contractions. *Applied Sciences* **7**, 1050 (2017).

67 Pallotti, A., Orengo, G. & Saggio, G. Measurements comparison of finger joint angles in hand postures between an sEMG armband and a sensory glove. *Biocybernetics and Biomedical Engineering* **41**, 605-616 (2021).

68 Ortenzi, V., Tarantino, S., Castellini, C. & Cipriani, C. in *2015 IEEE International Conference on Rehabilitation Robotics (ICORR).* 1-6 (IEEE).

69 Bi, L. & Guan, C. A review on EMG-based motor intention prediction of continuous human upper limb motion for human-robot collaboration. *Biomedical Signal Processing and Control* **51**, 113-127 (2019).

70 Hu, H. *et al.* Stretchable ultrasonic arrays for the three-dimensional mapping of the modulus of deep tissue. *Nature Biomedical Engineering* **7**, 1321-1334 (2023).

71 Lin, M. *et al.* A fully integrated wearable ultrasound system to monitor deep tissues in moving subjects. *Nature Biotechnology* **42**, 448-457 (2024).

72 Akhlaghi, N. *et al.* Real-time classification of hand motions using ultrasound imaging of forearm muscles. *IEEE Transactions on Biomedical Engineering* **63**, 1687-1698 (2015).

73 Yang, X., Zhou, D., Zhou, Y., Huang, Y. & Liu, H. Towards zero re-training for long-term hand gesture recognition via ultrasound sensing. *IEEE Journal of Biomedical and Health Informatics* **23**, 1639-1646 (2018).

74 He, J., Luo, H., Jia, J., Yeow, J. T. & Jiang, N. Wrist and finger gesture recognition with single-element ultrasound signals: A comparison with single-channel surface electromyogram. *IEEE Transactions on Biomedical Engineering* **66**, 1277-1284 (2018).

75 Fernandes, A., Ono, Y. & Ukwatta, E. in *2020 IEEE International Conference on Flexible and Printable Sensors and Systems (FLEPS).* 1-4 (IEEE).

76 Yang, X., Yan, J., Fang, Y., Zhou, D. & Liu, H. Simultaneous prediction of wrist/hand motion via wearable ultrasound sensing. *IEEE Transactions on Neural Systems and Rehabilitation Engineering* **28**, 970-977 (2020).

77 Iravantchi, Y., Zhang, Y., Bernitsas, E., Goel, M. & Harrison, C. in *Proceedings of the 2019 CHI Conference on Human Factors in Computing Systems.* 1-13.

78 Xue, X. *et al.* Development of a wearable ultrasound transducer for sensing muscle activities in assistive robotics applications. *Biosensors* **13**, 134 (2023).

79 Zhang, X., Huang, H. & Yang, Q. in *2013 35th Annual International Conference of the IEEE Engineering in Medicine and Biology Society (EMBC).* 5926-5929 (IEEE).

80 Purushothaman, G. & Ray, K. EMG based man–machine interaction—A pattern recognition research platform. *Robotics and Autonomous Systems* **62**, 864-870 (2014).

81 Ju, Z. & Liu, H. Human hand motion analysis with multisensory information. *IEEE/AsMe Transactions on Mechatronics* **19**, 456-466 (2013).

82 Al-Timemy, A. H., Bugmann, G., Escudero, J. & Outram, N. Classification of finger movements for the dexterous hand prosthesis control with surface electromyography. *IEEE Journal of Biomedical and Health informatics* **17**, 608-618 (2013).

83 Peng, L. *et al.* in *2015 International Conference on Advanced Mechatronic Systems (ICAMechS).* 365-369 (IEEE).

84 Boschmann, A., Platzner, M., Robrecht, M., Hahn, M. & Winkler, M. (Myoelectric Symposium).

85 Stango, A., Negro, F. & Farina, D. Spatial correlation of high density EMG signals provides features robust to electrode number and shift in pattern recognition for myocontrol. *IEEE Transactions on Neural Systems and Rehabilitation Engineering* **23**, 189-198 (2014).

86 Liu, J. & Zhou, P. A novel myoelectric pattern recognition strategy for hand function restoration after incomplete cervical spinal cord injury. *IEEE Transactions on Neural Systems and Rehabilitation Engineering* **21**, 96-103 (2012).

87 Paleari, M., Di Girolamo, M., Celadon, N., Favetto, A. & Ariano, P. in *2015 37th Annual International Conference of the IEEE Engineering in Medicine and Biology Society (EMBC).* 6086-6089 (IEEE).

88 Pan, L., Zhang, D., Liu, J., Sheng, X. & Zhu, X. Continuous estimation of finger joint angles under different static wrist motions from surface EMG signals. *Biomedical Signal Processing and Control* **14**, 265-271 (2014).

89 Stapornchaisit, S., Kim, Y., Takagi, A., Yoshimura, N. & Koike, Y. Finger angle estimation from array EMG system using linear regression model with independent component analysis. *Frontiers in Neurorobotics* **13**, 75 (2019).